# DEVELOPMENT OF POLYMERIC GAS SENSORS

A THESIS SUBMITTED TO
THE GRADUATE SCHOOL OF NATURAL AND APPLIED SCIENCES
OF
MIDDLE EAST TECHNICAL UNIVERSITY

BY

ÖZGE BATIR

IN PARTIAL FULFILLMENT OF THE REQUIREMENTS
FOR
THE DEGREE OF DOCTOR OF PHILOSOPHY
IN
CHEMICAL ENGINEERING

JUNE 2023

Approval of the thesis:

**DEVELOPMENT OF POLYMERIC GAS SENSORS**

submitted by **ÖZGE BATIR** in partial fulfillment of the requirements for the degree of **Doctor of Philosophy** i**n Chemical Engineering, Middle East Technical University** by,

Prof. Dr. Halil Kalıpçılar
Dean, Graduate School of **Natural and Applied Sciences** _____

Prof. Dr. Pınar Çalık
Head of the Department, **Chemical Engineering** _____

Assoc. Prof. Dr. Emre Büküşoğlu
Supervisor, **Chemical Engineering, METU** _____

Assoc. Prof. Dr. Erhan Bat
Co-Supervisor, **Chemical Engineering, METU** _____

**Examining Committee Members:**

Prof. Dr. Ömer Dağ
Chemistry, Bilkent University _____

Assoc. Prof. Dr. Emre Büküşoğlu
Chemical Engineering, METU _____

Prof. Dr. Nihal Aydoğan
Chemical Engineering, Hacettepe University _____

Prof. Dr. Pınar Zeynep Çulfaz Emecen
Chemical Engineering, METU _____

Assoc. Prof. Dr. Emrullah Görkem Günbaş
Chemistry, METU _____

Date: 21.06.2023

**I hereby declare that all information in this document has been obtained and presented in accordance with academic rules and ethical conduct. I also declare that, as required by these rules and conduct, I have fully cited and referenced all material and results that are not original to this work.**

Name Last name : Özge Batır

Signature :

# ABSTRACT

## DEVELOPMENT OF POLYMERIC GAS SENSORS

Batır, Özge
Doctor of Philosophy, Chemical Engineering
Supervisor : Assoc. Prof. Dr. Emre Büküşoğlu
Co-Supervisor: Assoc. Prof. Dr. Erhan Bat

June 2023, 99 pages

Detection of volatile organic compounds (VOCs) is an important issue due to their harmful impact on human health. In the first part of the study, we aimed at enhancing the sensitivity of the anisotropic polymeric films templated from cholesteric liquid crystals (CLCs) in the identification of VOCs at concentration in the order of 100 ppm. To increase sensitivity, we introduced strain to the films in the direction parallel to the helical axis and evaluated its effect on the sensitivity. Specifically, we used LC mixtures of reactive [4-(3-acryloyoxypropyloxy) benzoic acid 2-methyl-1,4-phenylene ester (RM257)], nonreactive E7 mesogen and chiral dopant [4-(1-methylheptyloxycarbonyl)phenyl-4-hexyloxybenzoate)) (S-811)] to synthesize CLC-templated polymeric films with programmed strain profiles using a wedge cell, and measured their response against a range of toluene vapor concentrations. Based on the obtained results, we demonstrated a relationship between the strain in the cholesteric pitch and the sensitivity of the sensor based on spacial responses evaluated from the change in coloring of the film. Our results showed that strain helps to increase the sensitivity of the sensors up to 15 times compared to their unstrained counterparts. Moreover, 90% of the equilibrium response is achieved in less than one minute of exposure which offers rapid diagnosis of VOCs. Our tests

for the reversibility of the sensors showed that the CLC-templated polymeric films can be used multiple times without a significant loss of sensitivity.

In order to increase the specificity and reusability of these structures together with sensitivity to achieve their successful integration into useful applications, in the second part of the study, we developed an interpenetrating polymeric network (IPN) based on poly(RM257) structure of CLC-templated polymeric films and polydimethylsiloxane (PDMS). Contrary to the generic CLC-hosted IPN sensors that use CLC structures to optically report the changes in the polymeric matrix, we employed the collaborative responsiveness of the constituents of the IPN (both CLC-templated and penetrated polymeric structures) to improve the sensor performance. The elastic swelling behavior of PDMS structure increased the durability and reusability of the poly(RM257) polymeric sensor upon exposure to even high VOC vapor concentrations up to their saturation. The sensor tests of both poly(RM257) and IPN films were carried out against four different VOC vapors namely toluene, hexane, acetone, ethanol and also water vapor. The results showed that the synergistic swelling behavior of PDMS and poly(RM257) polymeric structures against vapors directly affected the sensor performance in terms of earned specificity and enhanced sensitivity. Moreover, the real time experiments showed that the measurement accuracy, response, and recovery time of the polymeric sensors were also improved significantly by the development of IPN as compared to their non-IPN counterparts. This study shows a promise towards further engineering of sensors against various applications through detailed design of the constituent polymers against targeted species.

In the last part of the study, we aimed to synthesize and characterize optically active chiral metallomesogens. In the light of the studies presented in literature, a synthesis pathway was developed where the resulting molecule has reactive acrylate end groups, chiral part introduced by aminoalcohols and metal cores namely as either Pd, Cu or Zn. We firstly aimed to study effect of metal core type on chiral behavior of chiral reactive metallomesogens. Therefore, (R)- or (S)-2-amino-1-butanol

aminoalcohols were used to create chiral groups and complexed with three different metal acetates namely; Pd, Cu and Zn acetate. Chiral behavior of Pd and Cu complexes were confirmed by optical characterization and no significant impact of metal core type was observed on helical twisting power (HTP) of the chiral molecule. The complexes of Zn did not possess chiral symmetry due to unstable tetrahedral structure of Zn. We also aimed to examine effect of amino alcohol chiral group on behavior of the chiral reactive metallomesogens. Therefore, we used four more different amino alcohols with varying length of alkyl chains with or without phenyl groups and complexed them with palladium (II) acetate. Optical characterization results revealed that the complexes synthesized from the amino alcohols which has phenyl in their chiral group does not exhibit chiral behavior. When we compared chiral feature of the four different Pd complexes, we observed that increase of the chiral group chain length increases pitch size and decrease of HTP of the chiral reactive metallomesogens. Moreover, chiral reactive metallomesogens were photo-polymerized under UV light which was confirmed by optical characterizations and UV-visible spectrophotometry.

Keywords: Optical Sensor, Cholesteric Liquid Crystal, Interpenetrating Network, Volatile Organic Compound, Metallomesogen

# ÖZ

## POLİMERİK GAZ SENSÖRLERİN GELİŞTİRİLMESİ

Batır, Özge
Doktora, Kimya Mühendisliği
Tez Yöneticisi: Doç. Dr. Emre Büküşoğlu
Ortak Tez Yöneticisi: Doç. Dr. Erhan Bat

Haziran 2023, 99 sayfa

Uçucu organik bileşiklerin (UOB) tespiti, insan sağlığı üzerindeki zararlı etkilerinden dolayı önemli bir konudur. Çalışmanın ilk bölümünde, kolesterik sıvı kristallerden (KSK'ler) şablonlanan anizotropik polimerik filmlerin, 100 ppm mertebesinde konsantrasyonda UOB'lerin tanımlanmasındaki hassasiyetini arttırmayı amaçladık. Duyarlılığı artırmak için filmlere sarmal eksene paralel yönde gerinim uyguladık ve bunun duyarlılık üzerindeki etkisini değerlendirdik. Spesifik olarak, reaktif [4-(3-akriloyoksipropiloksi) benzoik asit 2-metil-1,4-fenilen ester (RM257)], reaktif olmayan E7 mezojen ve kiral katkı maddesi [4-(1-metilheptiloksikarbonil)fenil-4'ün LC karışımlarını kullandık. -heksiloksibenzoat)) (S-811)] bir kama hücresi kullanarak programlanmış gerinim profillerine sahip KSK-şablonlu polimerik filmleri sentezlemek için kullanıldı ve bir dizi toluen buhar konsantrasyonuna karşı tepkilerini ölçüldü. Elde edilen sonuçlara dayanarak, filmin rengindeki değişiklikten değerlendirilen uzamsal tepkilere dayalı olarak, kolesterik perdedeki gerinim ile sensörün hassasiyeti arasında bir ilişki olduğunu gösterdik. Sonuçlarımız, gerinimin, gerilmemiş muadillerine kıyasla sensörlerin hassasiyetini 15 kata kadar artırmaya yardımcı olduğunu gösterdi. Ayrıca, denge yanıtının %90'ına, UOB'lerin hızlı teşhisini sağlayarak bir dakikadan daha kısa sürede

ulaşılmıştır. Sensörlerin tersine çevrilebilirliğine yönelik testlerimiz, KSK-şablonlu polimerik filmlerin, önemli bir hassasiyet kaybı olmadan birden çok kez kullanılabileceğini gösterdi.

Bu yapıların özgüllüğünü ve yeniden kullanılabilirliğini artırmak ve yararlı uygulamalara başarılı bir şekilde entegre olmalarını sağlamak için hassasiyetle birlikte, çalışmanın ikinci bölümünde, poli(RM257) yapısında KSK-şablonlu polimerik filmler ve polidimetilsiloksana (PDMS) dayalı bir iç içe geçen polimerik ağ geliştirdik. Polimerik matristeki değişiklikleri optik olarak raporlamak için KSK yapılarını kullanan jenerik KSK bazlı iç içe geçen polimerik ağ sensörlerinin aksine, sensör performansını iyileştirmek için iç içe geçen polimerik ağ bileşenlerinin (hem KSK şablonlu hem de nüfuz eden polimerik yapılar) işbirlikçi yanıt verebilirliğini kullandık. PDMS yapısının elastik şişme davranışı, doygunluklarına kadar yüksek UOB buhar konsantrasyonlarına bile maruz kaldıktan sonra poli(RM257) polimerik sensörün dayanıklılığını ve yeniden kullanılabilirliğini artırdı. Hem poli(RM257) hem de iç içe geçen polimerik ağ filmlerin sensör testleri, toluen, heksan, aseton, etanol ve ayrıca su buharı olmak üzere dört farklı VOC buharına karşı gerçekleştirilmiştir. Sonuçlar, PDMS ve poli(RM257) polimerik yapıların buharlara karşı sinerjik şişme davranışının, kazanılan özgüllük ve gelişmiş hassasiyet açısından sensör performansını doğrudan etkilediğini gösterdi. Ayrıca gerçek zamanlı deneyler, polimerik sensörlerin ölçüm doğruluğunun, tepkisinin ve toparlanma süresinin de iç içe geçen polimerik ağ 'nin geliştirilmesiyle iç içe geçen polimerik ağ olmayan muadillerine kıyasla önemli ölçüde iyileştiğini gösterdi. Bu çalışma, bileşen polimerlerin hedeflenen türlere karşı ayrıntılı tasarımı yoluyla çeşitli uygulamalara karşı sensörlerin daha fazla mühendisliğine yönelik bir vaat göstermektedir.

Çalışmanın son bölümünde ise optik olarak aktif kiral metallomezojenlerin sentezlenmesi ve karakterize edilmesi amaçlandı. Literatürde sunulan çalışmalar ışığında, ortaya çıkan molekülün reaktif akrilat uç gruplarına, aminoalkollerin getirdiği kiral kısma ve Pd), Cu veya Zn olmak üzere üç farklı metal çekirdeğe sahip

olduğu bir sentez yolu geliştirilmiştir. İlk olarak, kiral reaktif metallomezojenlerin kiral davranışları üzerinde metal çekirdek tipinin etkisini incelemeyi amaçladık. Bu nedenle kiral gruplar oluşturmak için (R)- ve (S)-2-amino-1-butanol aminoalkoller kullanıldı ve üç farklı metal asetat ile kompleksleştirildi; Pd, Cu ve Zn asetat. Pd ve Cu komplekslerinin kiral davranışı, optik karakterizasyon ile doğrulandı ve kiral molekülün sarmal burulma gücü (HTP) üzerinde metal çekirdek tipinin önemli bir etkisi gözlenmedi. Zn kompleksleri, Zn'nin kararsız tetrahedral yapısından dolayı kiral katkı maddesi gibi davranmadı. Ayrıca amino alkol kiral grubunun kiral reaktif metallomezojenlerin davranışı üzerindeki etkisini incelemeyi amaçladık. Fenil içeren veya içermeyen farklı alkil zincir uzunluklarına sahip dört farklı amino alkol daha kullandık ve bunları paladyum (II) asetat ile kompleks haline getirdik. Optik karakterizasyon sonuçları kiral grubunda fenil bulunan amino alkollerden sentezlenen komplekslerin kiral davranış sergilemediğini ortaya koymuştur. Dört farklı Pd kompleksinin kiral özelliklerini karşılaştırdığımızda, kiral grup zincir uzunluğundaki artışın zift boyutunu artırdığını ve kiral reaktif metallomezojenlerin HTP'sini azalttığını gözlemledik. Ayrıca kiral reaktif metalomesojenler, UV ışığı altında polimerize edildi ve optik karakterizasyon ve UV-görünür spektrofotometri ile doğrulandı.

Anahtar Kelimeler: Optik Sensör, Kolesterik Sıvı Kristal, İç İçe Geçen Polimerik Ağ, Uçucu Organik Bileşik, Metallomezojen.

To my precious family

## ACKNOWLEDGMENTS

I would wish to express my deepest gratitude to my supervisor Assoc. Prof. Dr. Emre Bükuşoğlu, for his guidance, time, leadership, criticism, encouragement, insight and passion throughout our research. It was an honor for me to work with him as his first PhD student and I feel very lucky to have the opportunity to work with him. I would also like to show my gratitude to my co-supervisor Assoc. Prof. Dr. Erhan Bat for his helpful suggestions and different point of view which guided me throughout this research study. I also want to thank Prof. Dr. Ömer Dağ and Prof. Dr. Zeynep Çulfaz-Emecen for their valuable comments and discussions during my thesis monitoring committees; and Assoc. Prof. Dr. Görkem Günbaş for his support during my synthesis studies.

I would also like to say a special thank you to all the members and alumni of Soft and Functional Materials Laboratory Group; Aslı Karausta, Burak Akdeniz, Deniz Avşar, Ceren Kocaman, Selin Şengül, R. Umut Dinç, Elif Erçelik, Ali Akman, A. Nurcan Özşahin, Gülce İlhan, Dr. Pınar Beyazkılıç Ayas, Dr. Selda Sezer for their endless support, and friendship, and peaceful working environment. I also want to thank Zeynep Karabağ and Dr. Aliekber Karabağ for their help during my synthesis study. Many thanks to my dearest friends Ceren Karataş-Batan, Özge Meriç Demir and Aybüke Karakaş for their friendship and support ever since our high school days. I also want to Dr. Berrak Erkmen and Özge Şen for their endless support and all the good memories; without their support, it would be much harder for me to complete this study. I also want to thank my co-workers Ezgi Altıntaş, Neslin Doğan, Mehmet Soner Yaşar, Berkan Atman for their supports and hopeful point of view in all situations.

Last but not least, I want to express my deepest pleasure to my mother Leyla Batır, father Lütfü Batır and my little sister Neris Batır for their unconditional love, sacrifices, unshakable faith in me, and endless support over my whole life. They are

my luck; my success wouldn’t have been possible without their encouragement and love.

This work was supported by the Scientific Research Projects Coordination of the Middle East Technical University under the grant number TEZ-D-304-2020-10175 and Scientific and Technological Research Council of Turkey under grant number TUBİTAK 120Z987.

## TABLE OF CONTENTS

## LIST OF TABLES

TABLES

## LIST OF FIGURES

FIGURES

# CHAPTER 1

## INTRODUCTION

Nature has been an expert in the development of nanostructures resulting in structural coloring.[1] For example, the eye catching color with high reflectivity of Morpho butterfly, peacocks, jeweled beetles is a result of coherent scattering from the nanostructures with periodicities of ~100 nm.[2–4] Nature not only employs structural coloring in static states but also takes advantage of the change in color in a dynamic color in response to external stimuli such as the color change of chameleons during social interactions, which is an outcome of the presence of dynamic micro-nano periodic structures that reflect visible light.[5,6] According to Bragg's Law, diffraction maxima are observed in the direction in which the waves scattering from consecutive repeating planes with a distance of **d** are in the same phase.[7] Therefore, the distance between periodic micro-nano structures determines the wavelength of reflected light, and hence the apparent color.[8] Inspired from nature, we are motivated to develop passive optical sensors without external energy requirements by mimicking the visible light reflective properties of periodic structures in nature. These sensors could be used in a range of areas including industry, transportation vehicles, households where concentration of VOCs should be continuously recorded and reported for the occupational safety and health and in medical applications.

Volatile organic compounds are widely used in paint, adhesive, correction fluid, printing, and leather tanning processes in industry; and also in household cleaners in daily life.[9] However, due to their harmful effect to health, their exposure limits are usually specified and must be continuously monitored and controlled. Moreover, despite their harmful impacts, VOCs can also be used in biomedical applications. In this study, we chose toluene, acetone, ethyl alcohol, n-hexane and water vapor as our

model molecules. Although toluene, acetone, ethyl alcohol and n-hexane are used in many areas of industry and daily life, exposure to these VOCs must be kept under control because of their serious adverse effects on human's brain system, respiratory system, reproductive system and circulatory system.[10] The permitted exposure limit values for these VOCs determined by Occupational Safety and Health Administration (OSHA) are shown in Table 1.[10] As summarized, the limit of the concentration of toluene in the medium is 200 ppm for time weighted average (TWA) (with 300 ppm maximum) on long-term exposure and 500 ppm maximum on short-term exposure (10 minutes). For acetone, in the medium is 500 ppm for time weighted average (TWA) (with 750 ppm maximum) on long-term exposure and 3000 ppm maximum on short-term exposure (10 minutes). For ethanol, in the medium is 1000 ppm for time weighted average (TWA) on long-term exposure. For hexane, in the medium is 50 ppm for time weighted average (TWA) on long-term exposure and 500 ppm maximum on short-term exposure (10 minutes). Therefore, it is very important to develop sensitive, reversible, and durable sensors with high response speed that allows instantaneous and continuous diagnosis. However, the continuous diagnosis of VOCs is challenging since the exposure limit values are in the order of 100 ppm.

Table 1.1 OSHA permissible exposure limits and health effects of toluene, acetone, ethyl alcohol and n-hexane[10]

| Chemical | Limits | Health Factors and Target Organs |
|---|---|---|
| **Toluene** | **Long term exposure**<br>200 ppm TWA<br>300 ppm Ceiling<br>**Short term exposure**<br>500 ppm Peak<br>(10 minutes) | • Central nervous system depression, causing fatigue, headache, confusion, paresthesia, dizziness, and muscular incoordination<br>• Irritation of the eyes, mucous membranes, and upper respiratory tract |
| **Acetone** | **Long term exposure**<br>500 ppm TWA<br>750 ppm Ceiling<br>**Short term exposure**<br>3000 ppm Peak<br>(10 minutes) | • Kidney, liver, and nerve damage<br>• Increased birth defects<br>• Lowered ability to reproduce (males only) |
| **Ethyl alcohol** | 1000 ppm TWA | • Irritation of the eyes<br>• Irritaton of the upper respiratory tract mucous membranes |
| **n-hexane** | **Long term exposure**<br>50 ppm TWA<br>**Short term exposure**<br>500 ppm Peak<br>(10 minutes) | • Irritation and burning of the skin and eyes.<br>• Irritation of the nose, throat and lungs causing coughing, weezing and/or shortness of breath.<br>• Headache, nausea, vomitting, and passing out.<br>• Coma and death with high levels of exposure |

Liquid crystals (LCs) are widely used for detection and measuring of VOC concentration as they offer high sensitivity by the contribution of their elastic properties.[11,12] LCs are condensed fluid phases that are thermodynamically stable at temperatures intermediate between those that give rise to crystalline solids and isotropic liquids.[13] LCs exhibit unique optical properties due to long range ordering of their constituent molecules.[13] Nematics are one of the simplest LCs which are rod-like molecules with unidirectional order (Figure 1.1.a).[13,14] Adding chiral dopant to a nematic LC results in helical twisting of the molecules perpendicular to nematic order leading to a CLC phase which exhibit a wavelength and polarization selective

reflection (Figure 1.1.b).[15,16] If the pitch size, length of helical axis over 360˚ rotation of the rod-like molecules, is of the same order of magnitude as the wavelength of visible light, the cholesteric phase allows Bragg reflections in visible wavelengths (Figure 1.1.c).[14,17] In the limit of low concentrations, pitch size of cholesteric structure is inversely proportional with the concentration (c) and the helical twisting power (HTP) which is defined as the ability to form helical twisting of nematic LCs.

$$p = \frac{1}{H.T.P \times c} \qquad \text{Equation 1}$$

Pitch size can be influenced by various external stimuli (temperature, pH, chemical vapor, etc.), causing a change in the selective reflection wavelength and thus the reflected color (Figure 1.1.d).[14,18] Optical gas sensors have been produced by using this feature of CLCs. Recently, CLC films are attractive class of materials as they offer battery free operation and direct visualization[19] and have great potential to be used as gas or environmental sensors.[20–26] However, due to their fluidic properties, they have limited potential to be used in practical applications. Recent studies show that the configuration of the LCs are preserved via polymerization.[22,25,27] Several past studies have investigated the response of CLCs upon exposure to VOCs.[20–26,28,29] However, these efforts have not considered the low exposure limits of VOCs that is crucial for sensing and monitoring purposes (they have reported results at concentrations close to their saturation at ambient temperatures).

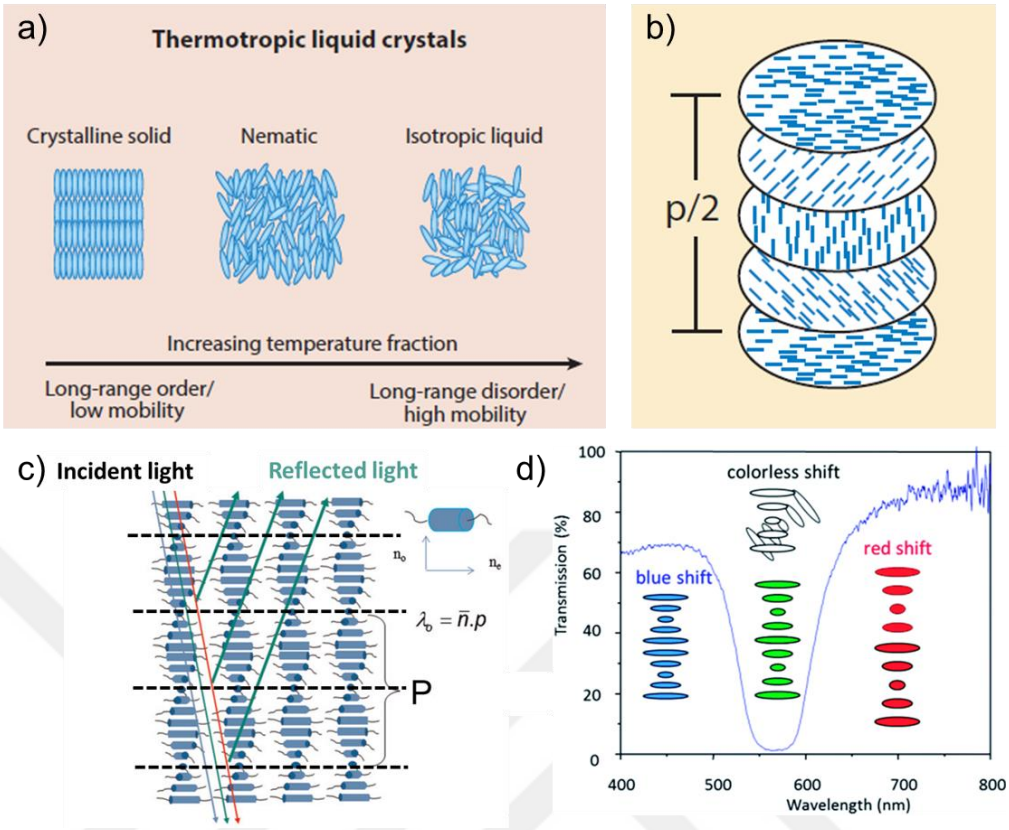


Figure 1.1 (a) Schematic of the phase behavior of thermotropic LCs.[30] (b) Schematic representation of the CLC structure.[30] (c) Light reflection behavior of CLC. (d) Pitch size and corresponding wavelength change of CLCs in visible ligth region upon exteral stimuli.[31]

Herein, in the first part of this study, we designed and characterized polymeric sensors synthesized from CLC templates aiming for use in practical applications. We anticipated the durability of the LC-based sensors to be enhanced using polymerization and will also be suitable for integration into wearable technologies. We chose toluene as the analyte due to its wide applications and accessible concentration exposure limits. We aimed to go beyond the past studies by increasing the sensitivity of the sensor to be used especially in a concentration range of 0-1000 ppm considering the exposure limits indicated in Table 1. In the second part of the study, we aimed to develop an IPN where the synergetic responsiveness of host matrix (CLC-templated structure) and penetrating polymer (PDMS) was used to gain specificity together with enhanced durability and reusability of sensors. We seek to

go beyond these past studies with the use of the IPNs formed by two constituents that exhibit response against exposure to different VOCs; which was not reported in literature, i.e. we also employed the responsive properties of CLC-templated structure in our design rather than using them only as optical reporters. In the last part of our research, we aim at the synthesis and characterization of reactive metallomesogenic molecules with chiral symmetries in order to address different application areas. The main reason for the selection of metallomesogenic reactive molecules is the chemical selectivity to be provided for diagnosis and the additional advantages of the possible secondary effects that may occur as a result of the interactions of the metal atom in the chiral center.[32,33] Therefore, it can be predicted that the reactive metallomesogens in chiral structure planned to be synthesized will enable many applications in the near future.

# CHAPTER 2

# LITERATURE REVIEW

Different approaches for the design of sensors have been developed for detection and measuring of VOC concentration based on the change in electrical properties[34–37], physical properties[38] and optical properties[28,39,40] upon exposure. Recently, optical sensors have been an attractive class of sensors due to their high sensitivity, easy fabrication, low power consumption, compactness, electromagnetic interference immunity properties, and more importantly due to their ease in quantification.[41] Optical sensors for detection of VOCs have been developed based on different materials such as co-polymers (Figure 2.1.a)[31,42–45], optical fibers (Figure 2.1.b)[39,46,47] and composite materials (Figure 2.1.c)[42,48]. The sensing mechanism of these sensors is based on the change in the fluorescence[43] or Bragg reflection[31,39,44,46,48] intensity and the reflected wavelength of the sensing material by the change in polymeric layer thickness, intermolecular or interparticle distances resulting from the interaction of the target substance and the sensing material.

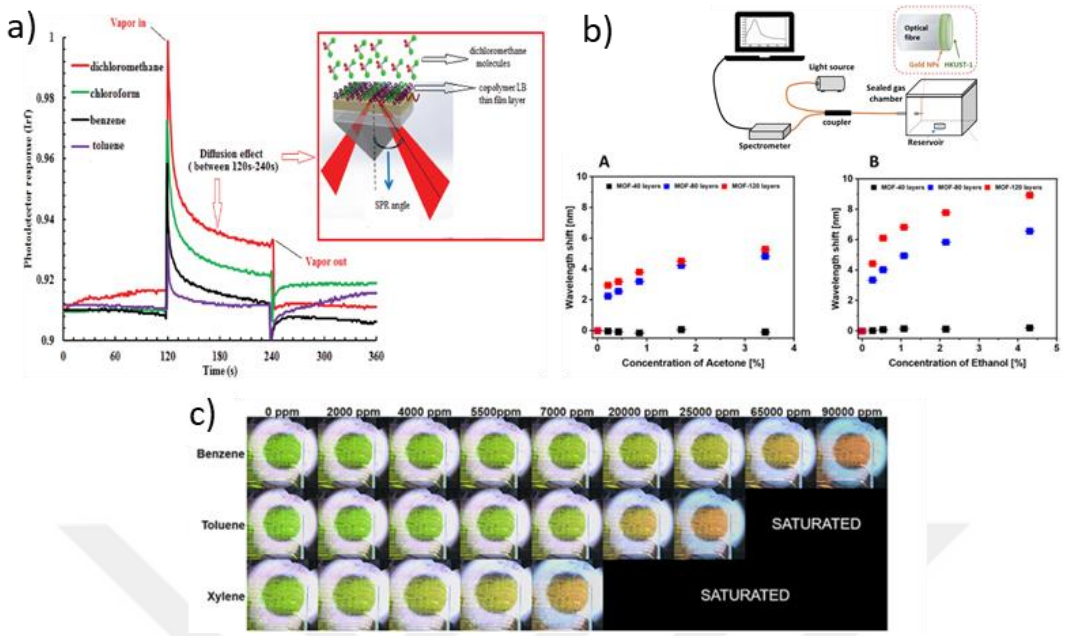


Figure 2.1 (a) Response of amphiphilic PDMA block copolymer film upon VOC exposure.[45] (b) Experimental set-up and dynamic response of optical fibre VOC sensor.[47] (c) Color change of colloidal crystal - PDMS composite upon different concentrations of VOCs.[42]

Besides these materials, liquid crystals (LCs) are also widely used as optical sensing elements for detection of VOCs by either change in molecular orientation or phase transition also with the contribution of their elastic properties.[11,12] Nayani et al.[11] worked on the orientational response of 5CB nematic LC decorated on metal surface upon exposure to dimethyl methylphosphonate (DMMP). They created strained state caused by homeotropic anchoring of nematic LC on the $La^{3+}$ perchlorate functionalized surface, planar anchoring on the air interface (Figure 2.2.b) and strain free state by ensuring homeotropic anchoring on both surfaces (Figure 2.2.a). These systems were exposed to DMMP analyte and the molecular reorientation was measured by change of the intensity of the transmitted light. The results showed that the release of initially stored elastic energy within the sensing unit resulted in faster initial responses, faster rates of responses and higher sensitivity as illustrated in Figure 2.2.c.

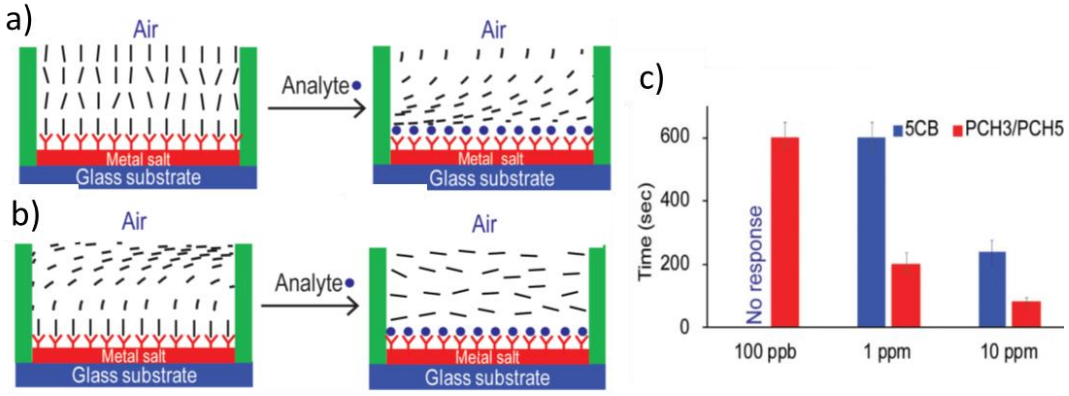


Figure 2.2 Schematic illustration of the director profile of (a) strain-free and (b) strained state before and after DMMP exposure. (c) Response time of strain-free and strained states to reach 80% of the equilibrium as a function of DMMP concentration.[11]

Cholesteric liquid crystals (CLCs), which are the phases formed by adding a chiral dopant to a nematic LC to induce helical twisting of molecular order, are promising candidates to be used as optical sensors which are widely reported in literature [20,22,29,49–51] Kek and co-workers[28] investigated the effect of chemical structure of CLCs on the response in terms of maximum wavelength shift upon exposure to toluene, cyclohexane, methyl ethyl ketone (MEK), n-hexane, acetone, ethanol and tert-butyl alcohol. To illustrate effect of contents of nematic LC and chiral dopant on response of CLC layer, CLC-2, containing tolan derivative and CLC-4 were prepared and spin-coated on glass substrate which was placed in a vessel and the VOCs were introduced to a vessel by a micropipette. With the interaction between CLCs and VOCs, reflected color of the CLC layers, were changed either as red shift (Figure 2.3.a) or blue shift (Figure 2.3.b) depending on the structure of CLC resulting change of $\lambda_{max}$ of the reflected light (Figure 2.3.c). This study is very important in terms of research on the response of CLC-based optical sensors upon different VOCs together with deeply investigation of the response in molecular interaction level; however, there are also some bottlenecks. Firstly, the proposed sensing system contains liquid state CLC layer deposited on the glass substrate and the response was measured by spectrophotometer which makes this system impractical for integration into wearable technologies. Secondly, sensor sensitivity was not considered as the response upon

saturation concentration of the VOC was reported which is way higher than the hundreds of ppm level exposure limits.

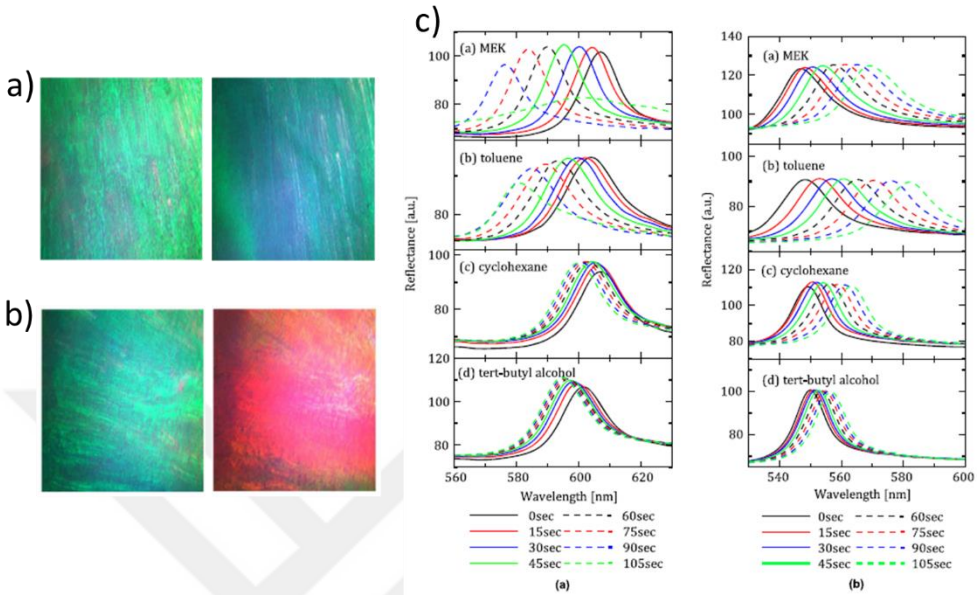


Figure 2.3 Optical microscopy images of (a) CLC-2 and (b) CLC-4 upon exposure to toluene. (c) Reflection spectra of CLCs exposed to MEK, toluene, cyclohexane and tert-butyl alcohol with repect to time.

Due to their fluidic nature, integration of CLC-based optical responsive materials into wearable technologies poses a problem. To overcome this problem, in the reported studies, polymerization is mostly preferred to maintain the initial configuration and optical properties of CLC structure.[22,23,27] In order to synthesize liquid crystalline polymeric materials, reactive mesogens containing rigid mesogenic core and reactive groups can be polymerized by free radical polymerization. The reactive groups can be at the end (end-on, Figure 2.4.a and one-end (Figure 2.4.b)) or at the side (side-on, Figure 2.4.c,d) of rigid mesogenic units.[52,53] The reactive groups of the mesogens can be polymerized by free-radical polymerization and can crosslink to each other and form main chain polymers (Figure 2.4.a,b) or laterally attached to a backbone (Figure 2.4.d) or a monomer unit (Figure 2.4.c) and form side chain polymer.

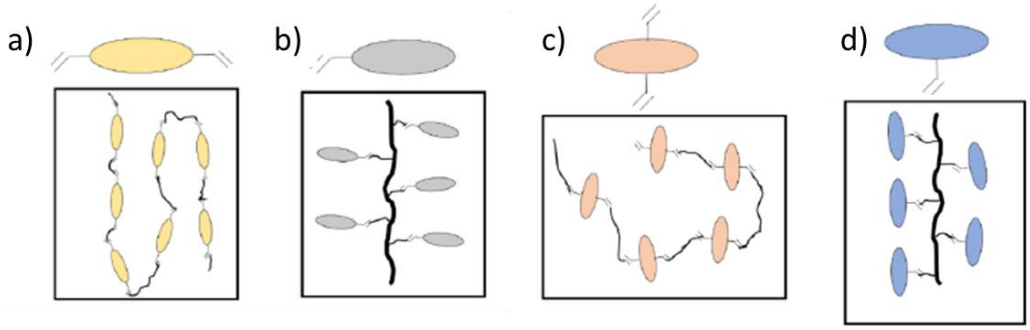


Figure 2.4 Different types of LC monomers with the reactive groups at the end; (a) end-on, (b) one-end, or (c,d) at the side (side-on) of rigid mesogenic units.[52]

In the study of Avsar and Bukusoglu[54], they synthesized CLC-templated polymeric particles by mask lithography and soft-lithography and used these particles for the detection of toluene vapor. Their results showed that CLC-templated particles exhibited red shift upon toluene exposure with the sorption of the molecules and swelling of the polymeric structure (Figure 2.5.a). Moreover, sensitivity results revealed that elastic energy stored due to extraction of nonreactive mesogens resulted in higher sensitivities (Figure 2.5.b). Furthermore, these polymeric particles were shown to be used several times without loss of sensitivity together with accurate measurement. Overall, in this study, with the help of polymerization, a durable sensor was developed with high sensitivity and reusability.

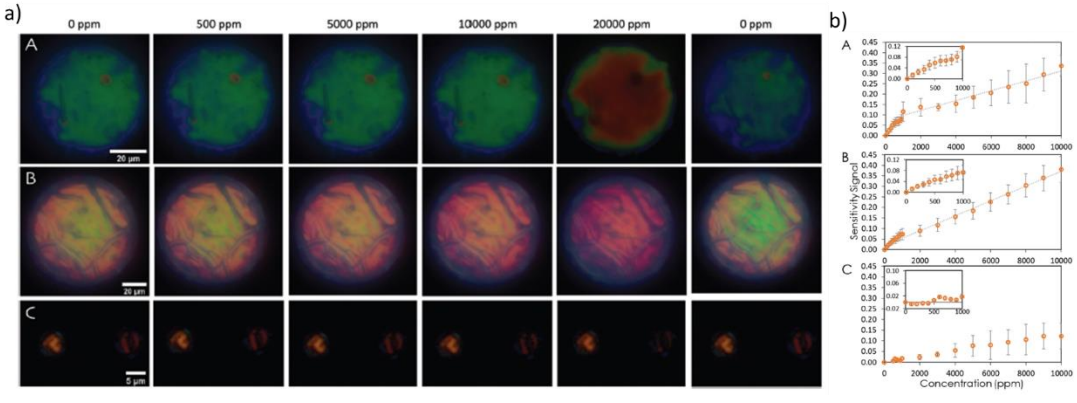


Figure 2.5 (a) Reflection mode optical micrographs and (b) response curves of CLC templated polymeric particles synthesized with (A) mask lithography, and soft lithography with size of (B)100 µm and (C) 7 µm.

In another study, Yeh et al.[55] used reactive LC mesogens to develop responsive hydrogen-bonded CLC-templated polymeric films for discrimination of methanol and ethanol in alcohol solutions. In order to get fast response and increase sensitivity of the sensor, 5CB, nematic LC - nonreactive mesogens, was extracted after polymerization and porous structure was developed (Figure 2.6.a) which increases the analyte-sensor interaction area. To study sensitivity and discrimination performance of the proposed sensors, solutions with varied methanol to ethanol ratio were prepared and change of central wavelength of the polymer was recorded (Figure 2.6.b). The results showed that as the molecular affinity of ethanol with hydrogen-bonded polymeric network is higher, ethanol rich alcohol solutions resulted in higher swelling of the polymeric structure and greater shift of central reflection wavelength. Furthermore, least square method revealed linear relationship between methanol-ethanol concentration and the wavelength shift (Figure 2.6.c).

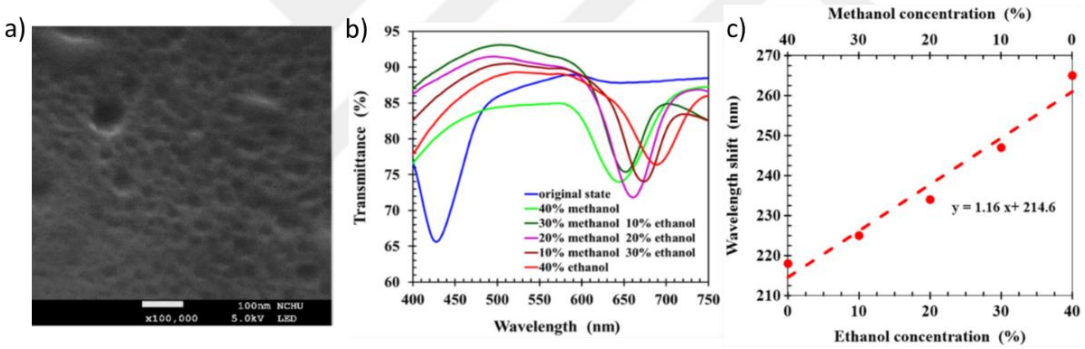


Figure 2.6 (a) SEM image of CLCP film after extraction of nonreactive 5CB nematic LC. (b) The transmission spectra of CLC films, (b) wavelength shift of CLCs upon alcohol solutions (40%) with different ethanol–methanol ratios.

Considering the studies reported in literature, in the first part of our study, we anticipated the durability of the LC-based sensors to be enhanced using polymerization which will also be suitable for integration into wearable technologies. We chose toluene as the analyte due to its wide applications and accessible concentration exposure limits. Although past studies have investigated the response of CLCs upon exposure to VOCs[20–26,28,29], these efforts have not considered the low exposure limits of VOCs that is crucial for sensing and monitoring purposes

(they have reported results at concentrations close to their saturation at ambient temperatures). Therefore, we firstly aimed to go beyond these past studies by increasing the sensitivity of the sensor to be used especially in a concentration range of 0-1000 ppm considering the exposure limits indicated in Table 1.

We sought to take the advantage of strain on enhancing the sensitivity of the polymeric sensors. Our approach to incorporate strain to the polymeric films involved two steps. First, we used mixtures of reactive and non-reactive mesogens to template the configuration and the cholesteric symmetry of the reactive mesogens and then extracted the unreacted part that incorporated strain via shrinkage preferentially along the helical axis. Second, we designed polymeric films with pre-programmed strain profiles that provide precise information of the local strain, which could be related to the sensitivity. With the advantage of this approach, we hypothesized that the diagnostic concentration range of the polymeric sensors may be expanded and lowered with the help of the elastic properties of the anisotropic polymers. In addition to this, we have foreseen that fast and continuous measurement can be obtained with the rapid response of the robust polymeric materials and the chemically inert nature of the system to be designed.

Interpenetrating polymeric networks (IPNs) comprise two or more networks which are at least partially interlaced on a molecular scale but not covalently bonded to each other.[56] IPN structures are widely used to combine the desired properties of the constituent polymers in the structure and increase functionality. IPNs can be prepared by two main methods, namely in-situ and sequential synthesis.[57] In the in-situ synthesis, all the reactants are mixed before the initiation of any polymerization or cross-linking reaction. In the sequential synthesis, the first polymer is synthesized and subsequently swollen which is needed for the formation of the second network within the first polymeric network.[57] IPNs can be used in wide range of applications such as biotechnology[58,59], energy storage[60,61], membrane[62–64], electrochemical devices[65], coatings[66] and sensors (bio-[67–69], pH[70–72], temperature[73,74], electrical energy[68], humidity[75,76] etc.). In recent years, CLC-based IPNs have also been used in optical sensing applications for detection of strain[77], humidity[77,78], temperature[79],

and pH[80,81] to optically report the changes in the geometry of the optically inactive polymeric networks. Hussain and Park[67] developed an optical glucose sensor by developing IPN between a photonic network and smart responsive hydrogel. The photonic network was prepared by polymerization of CLC-reactive mesogen (RMM) mixture which is responsible for the visible light reflection. After extraction of nonreactive chiral dopant, the pores were filled with a smart-polymer network which swells against external stimuli. The IPN array films were firstly exposed to different pH stimuli and corresponding color appearance was observed in the smart phone camera images (Figure 2.7.a). At low pH values, due to protonation of the PDMAEMA, the responsive hydrogel swells resulting increase of CLC pitch size and red-shift of the reflected color of CLC structure. In the second part, IPN arrays were exposed to glucose oxidase ($GO_x$) where 9 mM and higher concentration of $GO_x$ should be considered for diabetes patience. Immersion of 12 mM of $GO_x$ was determined as the optimum concentration considering reflected color and central wavelength of the reflected light illustrated in Figure 2.7.b.

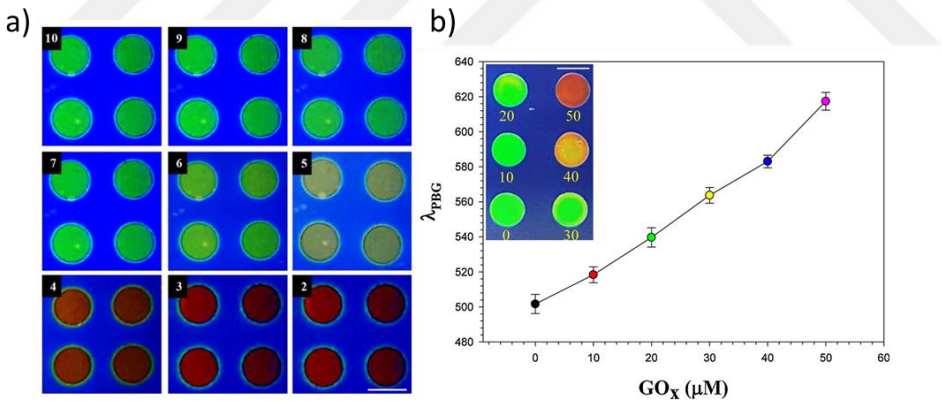


Figure 2.7 (a) Photographs of IPN arrays exposed to different pH stimuli for 40 minutes. (b) Optical micrograph and central wavelength of the reflected light from the IPN arrays immersed different concentrations of $GO_x$.

In the previous studies on CLC-based IPN sensors, specifically, the selective reflection properties of CLCs are cooperated with the swelling of hydrogels upon external stimuli that the volume change of hydrogel is optically reported through the color change of the CLC-templated structure. Furthermore, durability, reusability,

and specificity of both CLC-based and IPN sensors reported in the literature have not been investigated, that is still an issue that needs to be resolved.

In the second task of this work, we aimed to develop an IPN where the synergetic responsiveness of host matrix (CLC-templated structure) and penetrating polymer (PDMS) will be used to gain specificity together with enhanced durability and reusability of sensors. For this purpose, we used two generic polymer networks to highlight the generality of our approach. These two networks are chemically and optically distinct such that the PDMS network is optically transparent, whereas the poly(RM257) network possesses periodicity and an associated structural coloring due to Bragg reflections. First, we use 4-(3-acryloyoxy-propyloxy)benzoic acid 2-methyl-1,4-phenylene ester (RM257), a mesogenic reactive monomer, in mixtures of nematic host and a chiral dopant to form the cholesteric structure through templated polymerization methods.[82] The second polymer should have different response characteristics than the CLC-templated polymeric structure, and be transparent, easily accessible and processable. Therefore, we decided to use PDMS as an isotropic polymer that satisfies these and shows well-characterized, high swelling upon exposure to relatively low polarity solvents (e.g., toluene, hexane, and hydrocarbons).[83,84] We prepared IPN using sequential impregnation synthesis pathway by filling the pores of CLC-templated polymeric films with PDMS and called as IPN structure. To be used in our sensor tests, we chose five model molecules (both polar and non-polar) to investigate the distinct swelling tendency of both CLC-templated and PDMS polymeric structures and its effects on the response characteristic of the IPN in terms of specificity and sensitivity. Moreover, we anticipated that the elastic swelling of PDMS would increase durability and reusability of CLC-templated polymeric sensors upon high concentrations of VOC exposures. In the light of the results obtained in this study, complex mixtures can be specified via online and fully quantified IPN-based sensors whose constituents can be modified depending on the selective responsiveness.

It is very important to develop promising LC materials with wide application areas. Metallomesogens, which are LCs containing metal centers, also attract great

attention due to their optical, electrical, magnetic and electro-optical properties thanks to the metals in their structures. [85,86] Metallomesogenic structures shows high thermal and mechanical stability, different functionality of the active sites, efficient dichroic ratio and high emission efficiency which makes them to be used for wide range of applications such as the energy [87] (Figure 2.8.a), analytical instruments[88–90] (Figure 2.8.b), material[85,91,92] (Figure 2.8.c)/biomaterial[93] development, catalyst production[94,95] and electro-luminescence devices[96–98] (Figure 2.8.d).

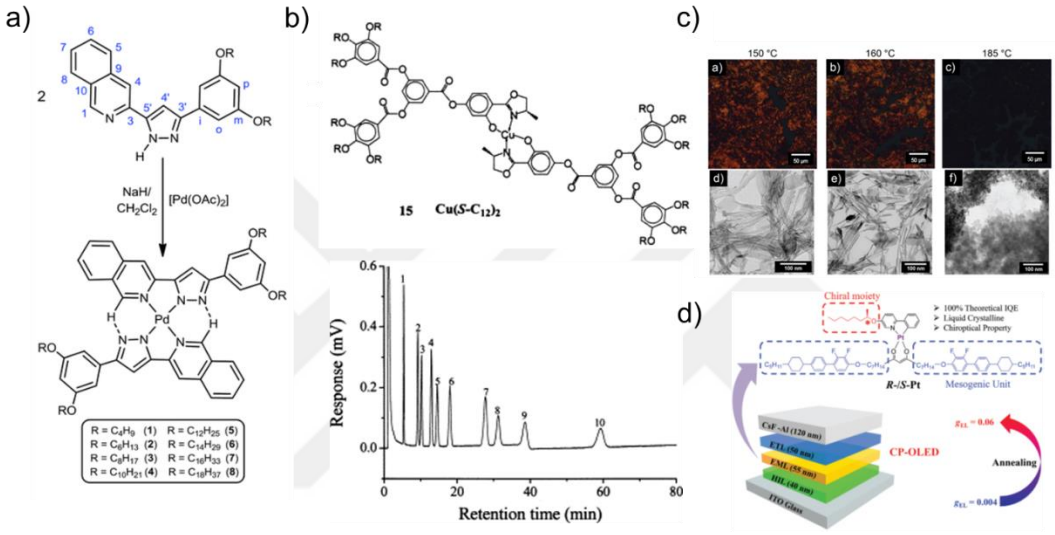


Figure 2.8 Sythesis of Pd(II) complex as one-dimensional proton conductors.[87] (b) Molecular structure of oxazoline Cu(II) complex and PAH separation gas chromatogram.[90] (c) Thermolysis of $CuSeC_{12}H_{25}$ templated by metallomesogens.[91] (d) Molecular structure of R/S-Pt ( including LC and chiral moetry) and fabrication of circularly polarized OLED diodes.[96]

Although metallomesogens show advanced properties derived from the existence of anisotropic phase metals, the stability and processability of these compounds are not as good as the other similar organic molecules.[99] In order to overcome this problem, synthesis of reactive metallomesogens containing acrylate[100] or 1,3-dienoxy tails[101] were reported in literature which can be polymerized by cross-linking of the reactive groups and durable polymeric structures can be developed. Cano and co-workers[100] synthesized mesomorphic salicylaldimines complexed with acrylate group modified Pd(II), Zn(II), VO(IV), and Cu(II). Liquid crystalline behavior of the reactive

metallomesogens were investigated and except Zn(II) complex, all the molecules exhibited mesogenic behavior. Moreover, the synthesized molecules are reactive, and can undergo bulk thermal or photo-initiated free-radical polymerization (except Cu(II) complex) by UV-visible spectrophotometer.

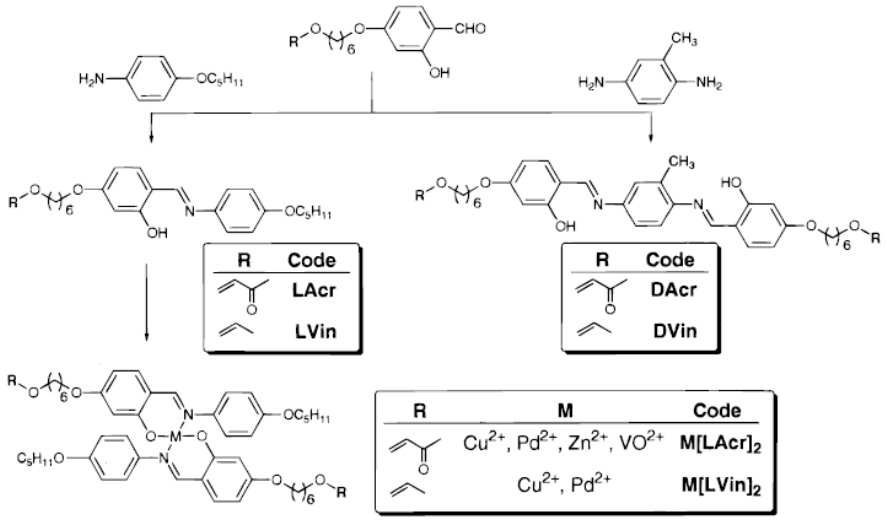


Figure 2.9 Synthesis of reactive Schiff bases and metal complexes.

Besides reactivity, metallomesogens can be also synthesized with the chiral symmetry[102] to use the excellent properties of chiral molecules such as unique physicochemical features, including circular dichroism, circularly polarized photoluminescence, optical properties, thermal conductance, chemical reactivity; ability to mimic complex biological processes and their potential applications in enantioselective events such as asymmetric catalysis and chiral sensing. [96–98] Lehmann et al.[102] synthesized chiral metallomesogens with different metal centers depending on the type of metal acetate as a result of the reaction of the chiral oxazoline ligands and metal acetate compounds they synthesized (Figure 2.10). NMR spectroscopy results showed that the synthesized compounds had two-fold symmetry confirming their chiral structure. The synthesized molecules were thermally characterized by DSC analysis confirming mesogenic behavior. The helical twisting power of the mixtures of chiral molecules with nematic LCs were measured by the Cano method and it was observed that when chiral molecule is

soluble in nematic LC, which is effected by the number of carbon atoms in the molecule, cholesteric phase was formed.

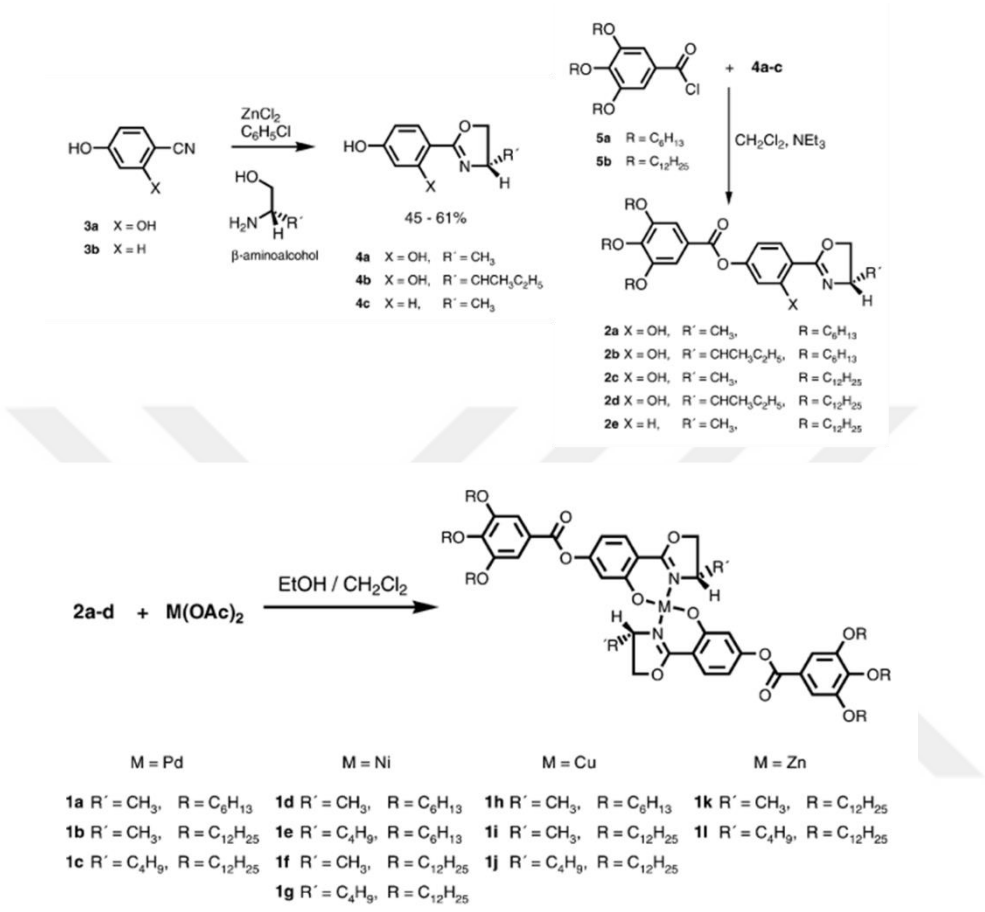


Figure 2.10 Synthesis of chiral metallomesogenic complexes.

When we consider studies on synthesis of metallomesogens, there is no molecule containing metal-centered chiral core and reactive end groups reported in literature. Therefore, we aimed to synthesize and characterize such molecule for the possible applications. Considering the studies in literature, firstly, we aimed to synthesize a molecule which has a nucleus with a chiral symmetry containing a metal atom. The main motivation of this aim is to provide a specific interaction in possible metal core-target molecule interactions; this interaction can result in change of helical twisting power of chiral molecule, thus resulting in an improved, noticeable change in optical appearance. As a result, studies to be carried out in the next stages may enable the

diagnosis of optical appearance changes and specific molecular interactions, and a useful material for sensor and diagnostic applications will be obtained. Second, the ends of the molecule were functionalized with acrylate groups to subject the sensing material to free radical photopolymerization to increase durability of structure. Thus, integration problems that may occur due to liquid behavior can be prevented without losing the molecular order in liquid structures and chiral symmetry can be addressed within the molecule to use their advantages in the possible applications. Considering the metallomesogen applications; chiral structured photo-active metallomesogens with *Palladium*, which has a high proton carrying capacity in a wide temperature range due to its high thermal stability and can be used in PEM fuel cells[87] and can add bioactive properties by changing the molecular organization of the ligand[92], metal center; *Copper*; which can be used as a template in the synthesis of nanocrystal structures[91], can be used as a stationary phase in separation processes[88], and can be used in gas sensor applications due to its high electron affinity[98] was synthesized and characterized.

# CHAPTER 3

# MATERIALS AND METHODS

## 3.1 Materials

Reactive mesogen 4-(3-acryloyoxy-propyloxy)benzoic acid 2-methyl-1,4-phenylene ester (RM257) and E7, nematic LC blend, (mixture of 51% of 4-cyano-4'-pentylbiphenyl (5CB), 25% of 4′-heptyl-4-biphenylcarbonitrile (7CB), 16% of 4′-n-octyloxy-4-cyanobiphenyl (8OCB) and 8% of 4-cyano-4"-n-pentyl-terphenyl (5CT)) were obtained from HCCH Jiangsu Hecheng Chemical Materials Co., Ltd. (Nanjing, China). Chiral dopant 4-(1-methylheptyloxycarbonyl)phenyl-4-hexyloxybenzoate)) (S-811) was purchased from Merck. 6-Chloro-1-hexanol, butyl vinyl ether, potassium carbonate, sodium iodide, 2-butanone, zinc chloride, chlorobenzene, dichloromethane, ethanol, palladium(II)acetate, copper(II)acetate, zinc(II)acetate, (R)-2-amino-1-butanol, (S)-2-amino-1-butanol, (S)-(+)-2-phenylglycinol, (R)-(+)-2-phenylglycinol, (S)-(-)-2-amino-3-phenyl-1-propanol and (S)-(+)-2-amino-3-methyl-1-butanol), dimethyloctadecyl[3-(trimethoxysilyl)-propyl]ammoniume chloride (DMOAP), polyvinyl alcohol (PVA), 3-(trichlorosilyl)propylmethacrylate (TCSPM), the photoinitiator 2,2 dimethoxy-2-phenylacetophenone, hexane, toluene and anhydrous acetone were purchased from Sigma- Aldrich (St. Louis, USA). Anhydrous ethanol was obtained from J.T. Baker (Phillipsburg, USA). SYLGARD™ 184 Polydimethylsiloxane (PDMS) Silicone Elastomer Kit was purchased from Dow Chemicals (Midland, Michigan, USA). Glass slides and cover glasses were obtained from Marienfeld GmbH (Lauda-Königshofen, Germany). were purchased from Sigma-Aldrich (St. Louis, USA). 2,4-dihydroxybenzonitrile was obtained from Apollo Scientific (Cheshire, UK). Prior to use, 6-chlorohexanol mixed with dichloromethane was neutralized by washing with 10% $NaHCO_3$.

## 3.2 Preparation of CLC – monomer mixtures

20 wt % reactive mesogen RM257 and chiral dopant at a percentage that depended on the desired reflected color of the polymeric film; were added to the non-reactive mesogen mixture E7. The photoinitiator was then added at 1 wt % based on the mass of RM257 to the mixture. Toluene, the co-solvent, was added to the LC mixture at about half of the weight of the E7 to dissolve and enable well mixing. The mixture was then mixed vigorously using a vortex mixer until a clear solution was obtained. Finally, toluene was evaporated from the solution under vacuum before use.

## 3.3 Preparation of glass substrates

To achieve planar anchoring of LCs, glass slides and PCX lens were coated with PVA. 5 wt % aqueous PVA solutions were prepared in deionized water. Glass surfaces were spin-coated at 5000 rpm for 2 minutes. The PVA surfaces were then rubbed with a fabric to maintain uniform planar anchoring of LCs. To prepare acrylate functionalized glass substrates, $O_2$ plasma was applied to the glass slides (using a Diener Electronics, Zepto Plasma Unit) before functionalization of the glass surfaces by TCSPM. O2 was fed to the system with a flow rate of 100 cm3/min for 15 min for the plasma cleaning and activation. Then, TCSPM was deposited on the surface with overnight incubation in a vacuum chamber.

## 3.4 Preparation of polymeric films

Flat films were synthesized in sandwich cells which were prepared with two pieces of PVA coated glass slides. The spacing was set using a polyethylene film as a spacer. The prepared glass slides were filled with the LC monomer-chiral dopant mixture with the help of capillary action. For strained films, optical cells were prepared by sandwiching the chiral mixture between a plano-convex (PCX) lens and

a flat glass slide. LC monomer-chiral dopant mixture was dropped on the convex side of PCX lens and sandwiched with the glass slide.

The photo-polymerization of the films was done by using a Spectroline ENF-280C/FE UV lamp (365 nm; Westbury, NY) that delivered 2.5 $mW.cm^{-2}$ at a distance of 5 cm from the light source. Sandwich cells were exposed to UV light for 30 min (Figure 3.1). After polymerization, sandwich cells were placed into Petri dishes which were filled with distilled water and incubated overnight to dissolve PVA. When PVA that coated the surface of the glass slides was dissolved, the polymer films were spontaneously detached from the surfaces. For the complete dissolution of PVA, the film was incubated in UP water for additional 2 hours after detachment. Then, free-standing polymeric films were placed in excess amount of pure ethanol to extract unreacted mesogens (Figure 3.1). Lastly, CLC-templated polymeric films were placed on glass slides to be used in toluene tests. The detailed characterization of the LC-templated RM257 polymeric films can also be found elsewhere.[103]

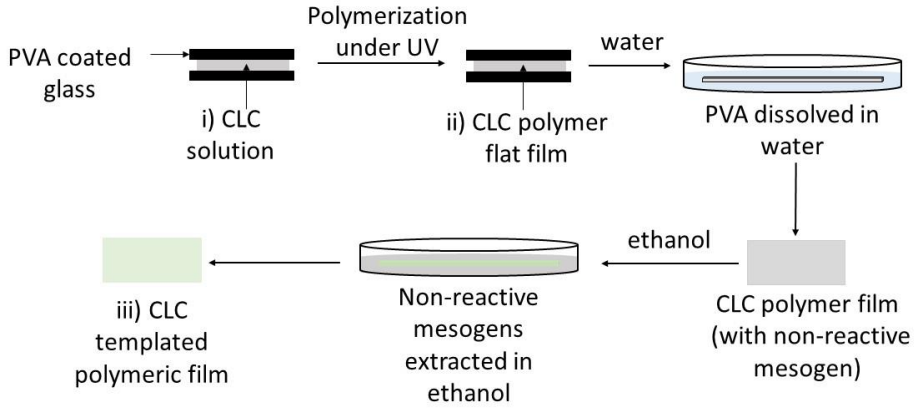


Figure 3.1 Schematic illustration of the preparation of CLC-templated polymeric films.

In order to synthesize IPN films, PDMS precursor and curing agent were mixed in 10/1 by weight ratio and dropped on the CLC-templated polymeric film before the pores are closed with evaporation of ethanol. During this filling process, a part of PDMS would be cured. To ensure complete curing of PDMS precursor, the

polymeric film was left in furnace overnight at 50°C. Then, the excess PDMS present on the surface of the polymeric film was removed using a tweezer to overcome mass transfer limitations during sensor tests (photographs of preparation of IPN are illustrated in Figure 3.1). Lastly, IPN films on acrylate coated glass slides were used in sensor tests.

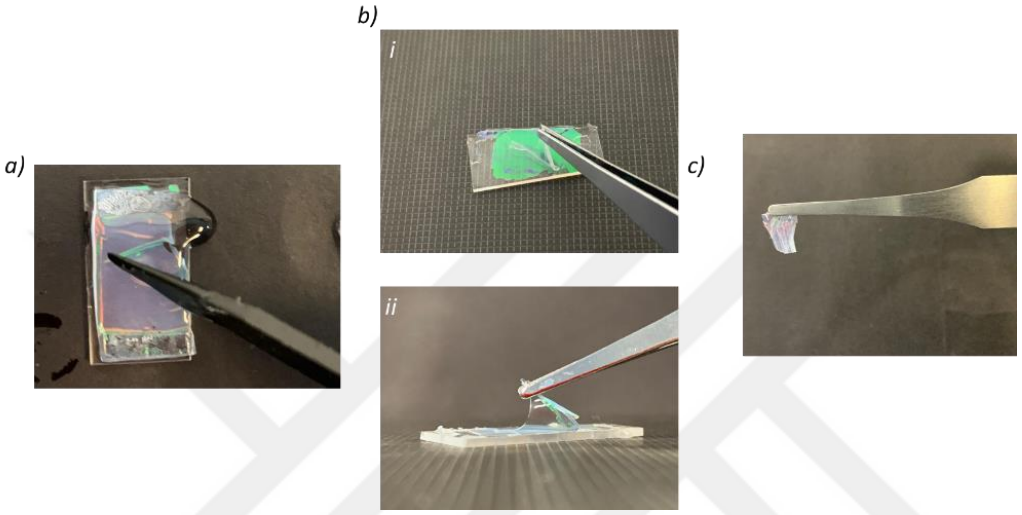


Figure 3.2 Preparation of IPN. (a) Dropping of PDMS precursor-curing agent mixture on CLC-templated polymeric film, (b) removing of excess PDMS after curing PDMS precursor, (c) after detachment from the acrylate coated glass slide.

## 3.5 Characterization of polymeric films

CLC mixtures were prepared with different chiral dopant ratio and UV-visible spectra of CLC films were recorded before - after polymerization and after extraction non-reactive mesogens using SHIMADZU UV-2550 spectrophotometer. An empty sandwich cell was used as reference in the measurements. In order to clarify the effect of interpenetration of PDMS on the structure of CLC-templated polymeric film, we collected UV-visible spectra of the polymeric films by THORLABS CCS100/M Compact Spectrophotometer which is integrated into the optical microscope. To investigate the effect of PDMS filling on the thermal behavior of CLC-templated polymeric films, Differential Scanning Calorimetry (DSC) (Shimadzu DSC-60) was used; heating and cooling were applied to the polymer two

times between 25 and 150 °C at a rate 10 °C/min and the second heating curves were illustrated. To investigate the chemical structure of PDMS, poly(RM257) and IPN films, FTIR analyses were carried by Perkin Elmer Spectrum Two FTIR Spectrophotometer. The surface morphology of the polymeric films was characterized by using a Quanta 400F Field Emission series scanning electron microscope and $N_2$ adsorption-desorption isotherms obtained by using Micromeritics TriStar II instruments at 77 K. The samples were degassed under vacuum at 333 K overnight. A Barrett−Joyner−Halenda (BJH) model was used to estimate the pore size distribution of polymeric films from the desorption isotherms.

### 3.6 Response tests

A schematic illustration of the experimental set-up is shown in Figure 3.3. A vacuum system was built for the introduction of precise concentrations of toluene vapor while imaging the CLC-templated polymeric films. The system consists of a toluene reservoir, valves for the toluene input from the reservoir and concentration tuning, and a vacuum pump. The exposure chamber was put on the optical microscope stage. Before starting the sensor tests, toluene reservoir was placed in liquid nitrogen and degassed. Next, the film was placed in a sample cell, and then system was evacuated for 15 minutes. The test was carried between 0 ppm to vapor pressure of toluene at room temperature when necessary. Concentration of toluene delivered to the system was controlled by monitoring the pressure using a Baratron® capacitance manometer (MKS Instruments). After delivery of toluene vapor to the desired pressure, the system was allowed to equilibrate for 2 minutes and reflection mode polarized optical micrographs of the films were taken at equilibrium for determination of the response curves (We verified that 2 minutes duration was enough to reach steady state conditions.). Then, we analyzed the selected areas and determined the change in average red-green-blue (RGB) values with increasing toluene concentration or with respect to time. To obtain the response curve, we calculated sensitivity signal as;

$$\text{sensitivity signal} = \left(\frac{R-R_0}{R_0} - \left(\frac{G-G_0}{G_0} + \frac{B-B_0}{B_0}\right)\right) \qquad \text{Equation 2}$$

where R, G, and B letters stand for the average red, green, blue signal intensities measured from the micrographs and the subscript zero indicates its value at 0 ppm of toluene. Then, the response curve was obtained by plotting the signal with respect to the toluene concentration obtained from three independent measurements.

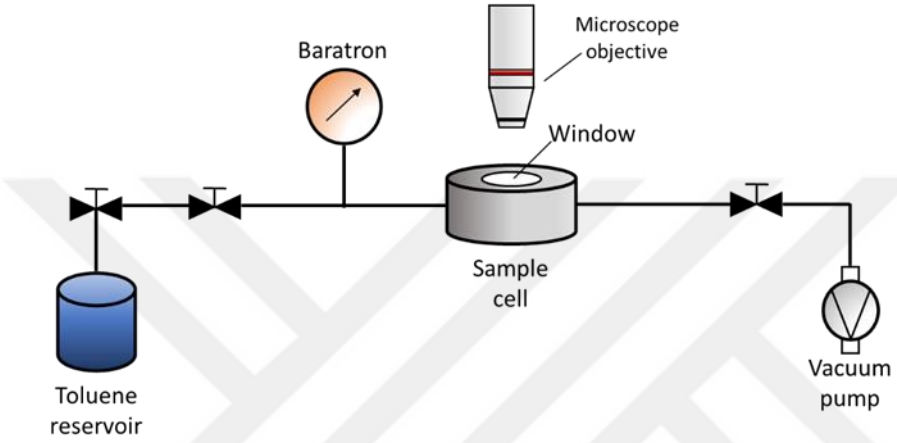


Figure 3.3 Schematic representation of the experimental setup.

## 3.7 Synthesis of chiral reactive metallomesogens

In the light of the studies reported in literature, the synthesis procedure shown in Figure 3.4 was determined. The synthesis procedure began with commercially available nitrile 1. According to the literature, the hydroxy group in the para position to the nitrile can be selectively alkylated. [102] Alkylation was carried out with vinyl ether, which is commercial but can also be easily synthesized using the corresponding alcohol and n-butyl vinyl ether. [104] The resulting alkyl benzo nitrile (2) was reacted with optically active amino alcohols (the chemical structure of amino alcohols are available in Appendix C. 1) in the presence of $ZnCl_2$ to produce compound 3. Finally, two moles of compound 3 was complexed with one mole of

metal acetate (copper, palladium and zinc) to obtain optically active polymerizable units and mentioned in the manuscript as the **M**- X complex (e.g. Pd-3a).

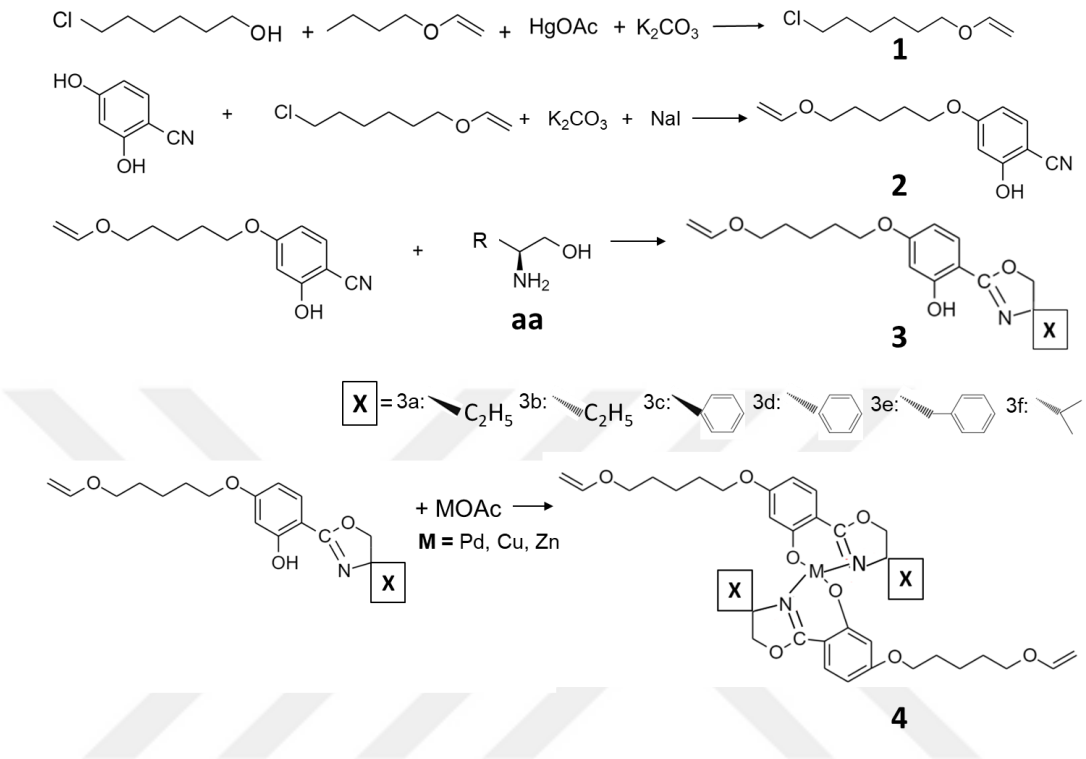


Figure 3.4 Synthesis of chiral reactive metallomesogens.

### 3.7.1 Synthesis of compound 1

To synthesize (6-chlorohexyloxy)ethane[104] (Figure 3.5) ethyl vinyl ether (249.24 g, 3.45 mol) was reacted with neutralized 6-chorohexanol (79.43 g, 0.58 mol) and mercury acetate (3.46 g, 0.01 mol). The reaction was performed at reflux for 3 h at 110°C. Then 10 g (0.07 mol) of anhydrous potassium carbonate was added to the solution.

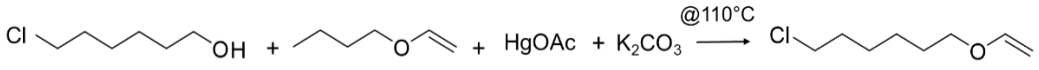


Figure 3.5 (a) Synthesis of (6-Chlorohexyloxy)ethane.

In thin layer chromatography (TLC), 3 spots were observed on the TLC plate. The product was then purified by silica gel column chromatography using hexane/EtOAc (first started with pure hexane, then continued with 15:1) as eluent. The NMR analysis of 3 different materials obtained from silica column were conducted and the top spot was determined as our material. After purification, yellow oily liquid was obtained with yield of 54.7%. The $^{1}$H NMR spectra was illustrated in

Appendix D.1. $^{1}$H NMR (δ, $CDCl_3$): 1.47-1.56 (4H, m, Cl-$CH_2$-$CH_2$-$CH_2$-$CH_2$), 1.69-1.74 (2H, m, O-$CH_2$-$CH_2$), 1.80-1.86 (2H, m, Cl-$CH_2$-$CH_2$), 3.62-3.66 (2H, m, Cl-$CH_2$), 3.71-3.74 (2H, m, O-$CH_2$), 3.96-4.21 (2H, m, O-CH=$CH_2$), 6.50-6.55 (1H, m, O-CH).

### 3.7.2 Synthesis of compound 2

To synthesize 4-(6-hydroxyhexyloxy)-2-hydroxybenzonitrile[100] (Figure 3.6), a mixture of 2,4-dihydroxybenzonitrile, 6-chlorohexanol, $NaHCO_3$ and NaI in butanone was maintained at reflux temperature for 36 h. The reaction mixture was filtered, evaporated to dryness and the crude product was purified by silica column chromatography using hexane/EtOAc (first started with pure hexane, then continued with 15:1, 10:1 and 5:1). The NMR analysis of 3 different materials obtained from silica column were conducted. The top spot was determined as the starting material, (6-chlorohexyloxy)ethane, the second spot was the side product in which hydroxy groups in the both para and ortho position to the nitrile was alkylated. The spot at the bottom was determined as our product which was confirmed by H-NMR analysis with yield of 46.4%. The $^{1}$H NMR spectra was illustrated in Appendix D.2. $^{1}$H NMR (δ, $CDCl_3$): 1.47-2.02 (4H, m, $CH_2$-$CH_2$-$CH_2$-$CH_2$), 3.66-3.74 (2H, m, O-$CH_2$), 4.18-4.21 (2H, m, CH=$CH_2$), 4.26-4.32 (2H, m, $CH_2$-O), 6.50-6.55 (2H, m, O-CH), 7.17 (1H, s, C=CH), 7.42 (1H, s, CH=C).

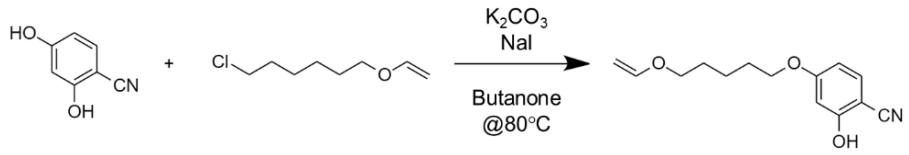


Figure 3.6 Synthesis of 4-(6-hydroxyhexyloxy)-2-hydroxybenzonitrile.

### 3.7.3 Synthesis of compound 3

To synthesize compound 3[102,105], in a 100-ml two-necked flask, 68 mg of $ZnCl_2$ (0.50 mmol) was melted under high vacuum and cooled under argon. After cooling to room temp., 30 ml of chlorobenzene was added followed by 10 mmol of the 4-(6-hydroxyhexyloxy)-2-hydroxybenzonitrile and 30 mmol of the amino alcohol (R-2-amino-1-butanol, S-2-amino-1-butanol, (S)-(+)-2-phenylglycinol, (R)-(+)-2-phenylglycinol, (S)-(-)-2-amino-3-phenyl-1-propanol and (S)-(+)-2-amino-3-methyl-1-butanol) as shown in Figure 3.7, Figure 3.8, Figure 3.9 and Figure 3.10 . The mixture was heated under reflux for 36 h. The solvent was removed under reduced pressure to give an oily residue, which was dissolved in 30 ml of dichloromethane. The solution was extracted three times with 20 ml of water and the aqueous phase with 30 ml of dichloromethane. The combined organic phases were dried with sodium sulfate, and the solvent was removed in vacuo. In literature, it was reported that the resulting oil was purified by silica column chromatography using pentane/EtOAc (4:1). However, when we used the reported system, we could not collect pure product. Therefore, we started with pure hexane and gradually increased polarity to hexane:EtOAc (1:2). The spot at the bottom was determined to be our product which was confirmed by H-NMR analysis illustrated in Appendix D.3, Appendix D. 8, Appendix D. 9, Appendix D. 10. $^1$H NMR (δ, $CDCl_3$): 1.47-2.02 (4H, m, $CH_2$-$CH_2$-$CH_2$-$CH_2$), 3.66-3.74 (2H, m, O-$CH_2$), 4.18-4.21 (2H, m, CH=$CH_2$), 4.26-4.32 (2H, m, $CH_2$-O), 6.50-6.55 (2H, m, O-CH), 7.17 (1H, s, C=CH), 7.42 (1H, s, CH=C), 7.68 (2H, s, CH=C).

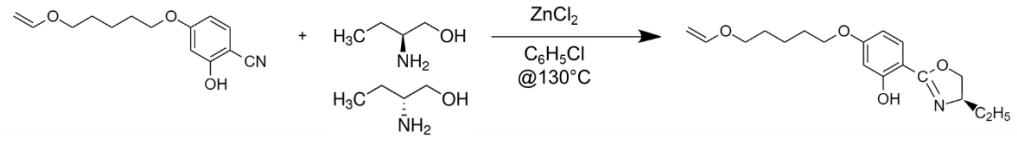


Figure 3.7 Synthesis of compound 4 by (R)- and (S)- 2-amino-1-butanol.

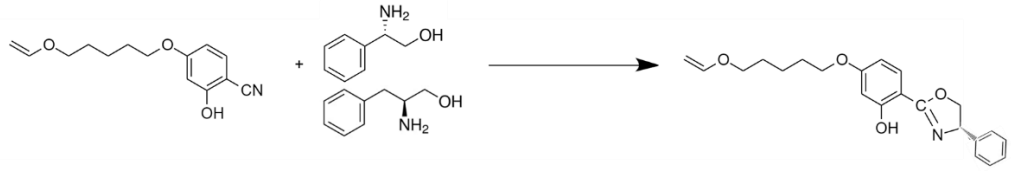

Figure 3.8 Synthesis of compound 4 by (R)- and (S)-(+)-2-phenylglycinol.

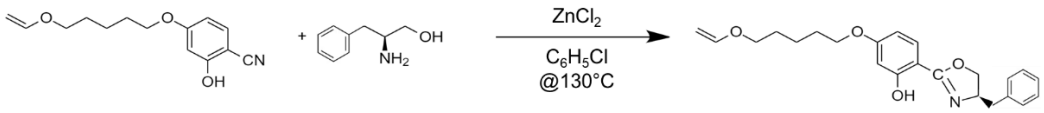


Figure 3.9 Synthesis of compound 4 by (R)-(-)-2-Amino-3-phenyl-1-propanol.

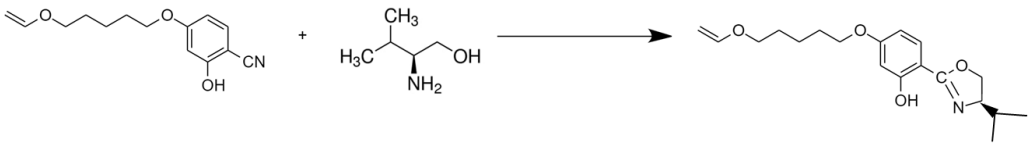

Figure 3.10 Synthesis of compound 4 by (S)-(+)-2-amino-3-methyl-1-butanol.

### 3.7.4 Synthesis of compound 4

To synthesize compound 4[100,102], the appropriate metal salt (palladium (II) acetate, copper (II) acetate and zinc acetate) in 96% ethanol was added to a solution of the compound 4 synthesized by (R)- and (S)-2-amino-1-butanol and palladium (II) acetate was added to solution of compound 4 synthesized by (S)-(+)-2-phenylglycinol, (R)-(+)-2-phenylglycinol, (S)-(-)-2-amino-3-phenyl-1-propanol and (S)-(+)-2-amino-3-methyl-1-butanol in 96% ethanol at reflux temperature (Figure

3.11, Figure 3.12, Figure 3.13 and Figure 3.14. After stirring 5 h, the precipitate was filtered and washed with 96% ethanol, dissolved in chloroform, and filtered through Celite®. In thin layer chromatography (TLC), 2 spots were observed on the TLC plate. After separation of two products, the product at the bottom was confirmed to be our main product by 1H-NMR analysis, illustrated in Appendix D.4, Appendix D. 5, Appendix D. 6, Appendix D. 7, Appendix D. 11, Appendix D. 12. 1.47-2.02 (4H, m, $CH_2$-$CH_2$-$CH_2$-$CH_2$), 3.66-3.74 (2H, m, O-$CH_2$), 4.18-4.21 (2H, m, CH=$CH_2$), 4.26-4.32 (2H, m, $CH_2$-O), 6.50-6.54 (2H, m, O-CH), 7.18 (1H, s, C=CH), 7.40 (1H, s, CH=C), 7.67 (2H, s, CH=C).

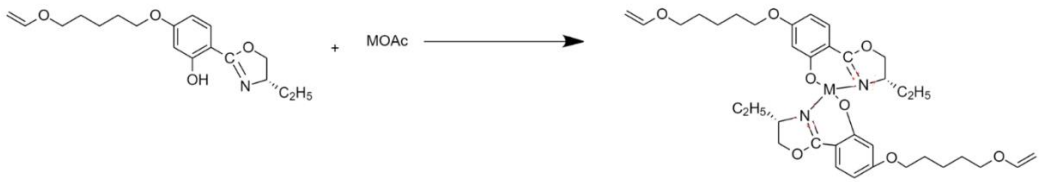


Figure 3.11 Synthesis of Pd complex of compound 4 synthesized from (R)- and (S)- 2-amino-1-butanol.

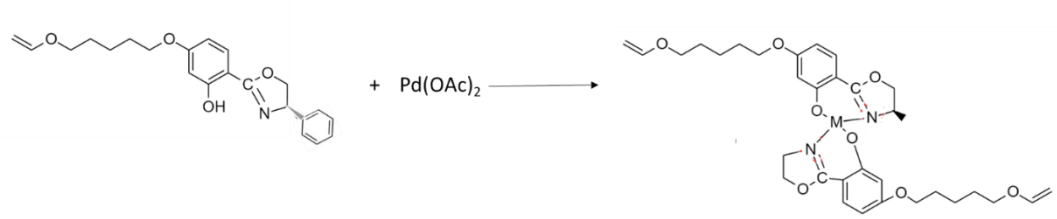


Figure 3.12 Pd complex of compound 4 synthesized from (R)- and (S)-(+)-2-phenylglycinol.

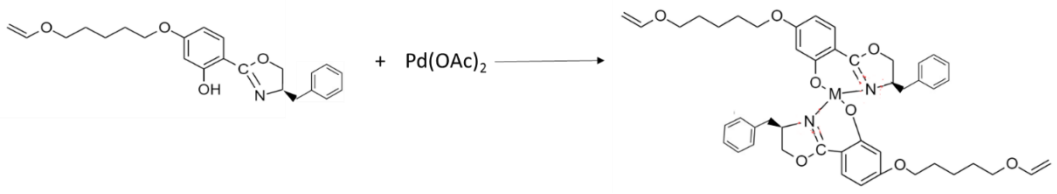


Figure 3.13 Pd complex of compound 4 synthesized from (R)-(-)-2-Amino-3-phenyl-1-propanol.

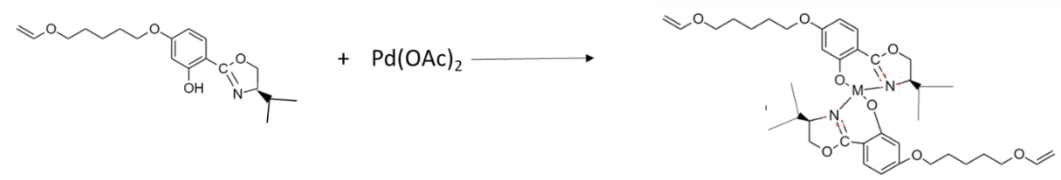


Figure 3.14 Pd complex of compound 4 synthesized from (S)-(+)-2-amino-3-methyl-1-butanol.

### 3.7.5 Characterization of chiral reactive metallomesogens

Optical characterizations were performed using an Olympus BX50 microscope (Olympus Inc., Japan) equipped with a polarizer and analyzer filters. Thermal behavior of the metallomesogens were characterized by Perkin Elmer Diamond Differential Scanning Calorimetry (DSC); two heating and cooling cycles was applied between -90 and 150°C at a rate 10 °C /min under nitrogen. Thermal gravimetric analysis (TGA) (Shimadzu DTG-60H) was applied by heating the sample from room temperature to 900°C with a heating rate of 10 °C /min under nitrogen atmosphere. The circular dichroism spectrum was scanned with the Jasco J 815 spectrophotometer from 300 to 700 nm.

# CHAPTER 4

# RESULTS AND DISCUSSIONS

The study described in this thesis was divided into two main parts. In the first part of the thesis study, we designed, synthesized, and characterized the response characteristics of polymeric sensors synthesized from CLC templates for the determination of volatile organic compound (VOC) vapor with enhanced performance in terms of sensitivity, specificity and reusability. In the second part of the thesis study, we aimed to synthesize and characterize chiral reactive metallomesogens and use a bottom up approach to develop chiral polymeric structures.

## 4.1 Development of Polymeric Sensors Templated from Cholesteric Liquid Crystals with Enhanced Performance

Within the first part of this section, we aimed to enhance the sensitivity of CLC templated polymeric sensors by using the strain resulted from the extraction of non-reactive mesogen and the geometry of the film. In the second part, we further enhanced performance of the CLC templated polymeric sensors by developing interpenetrating polymeric network (IPN) where the synergetic responsiveness of host matrix (CLC-templated structure) and penetrating polymer (PDMS) was used to gain specificity together with enhanced durability and reusability of sensors.

### 4.1.1 Strain-enhanced Sensitivity of Polymeric Sensors Templated from Cholesteric Liquid Crystals

#### 4.1.1.1 Synthesis and characterization of the cholesteric liquid crystal templated polymeric films

We first aimed at synthesizing a strained film confined in a wedge cell formed by a plano-convex (PCX) lens and a flat glass slide (Figure 4.1.a,b). When CLC mixture of 20% RM257, 7.5% chiral dopant and balance E7 was confined to this geometry, disclination lines appeared in strained film as shown in Figure 4.1.c,d between each periodic color patterns. We explained the origin of the disclination lines in Fig. 1c along with the observations in literature.[106–108] In brief, the cholesteric helices are unstrained only when the distance between two surfaces (PCX lens and glass slide surfaces) are commensurate with the number of a half pitch. On either side of the unstrained regions, the cholesteric helix is strained (either compressed or stretched). At a thickness, energetic cost of accommodating one more half pitch becomes favorable, this causes the formation of a defect which is visible as a sharp line under the microscope (Figure 4.1.d, indicated by arrows). Within each period, a color change from shorter to longer wavelength in the direction of increasing film thickness was observed (left to right), as shown in Figure 4.1.d and sketched in Figure 4.1.c. This is an indicative of a gradual change from compressed to stretched helical pitch between each consecutive disclination line as the thickness is increased.[106,107]

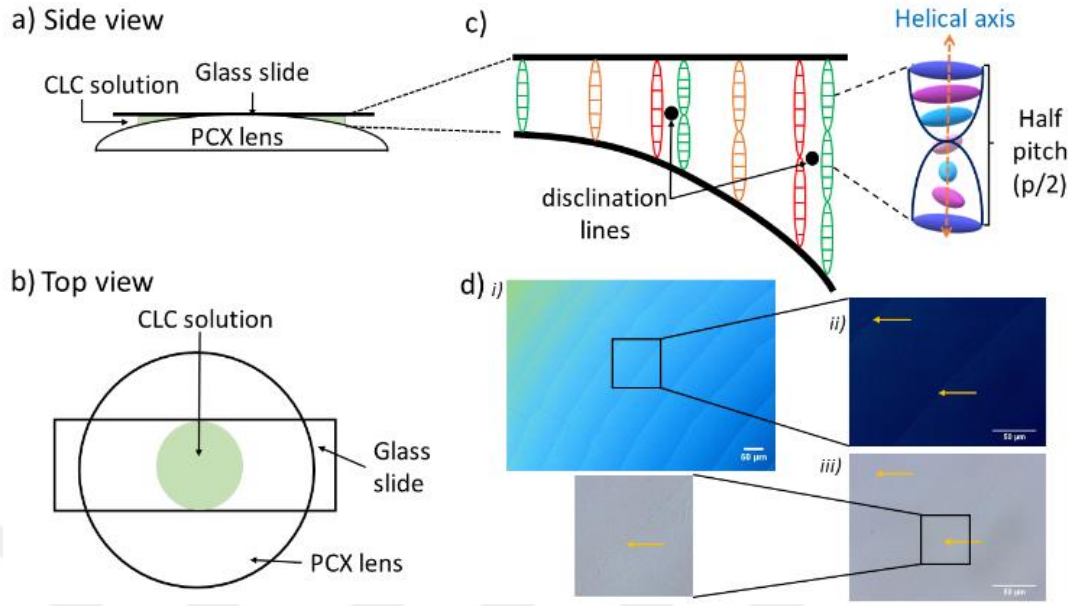


Figure 4.1 (a) Side view and (b) top view of cholesteric liquid crystal between a PCX lens and glass slide. (c) Schematic representation of origin of disclination lines which appears when CLC is inserted between PCX lens and glass slide. (d) i) Reflection-mode polarized light, ii) transmission mode polarized light and iii) transmission mode brightfield micrographs of a strained CLC film synthesized from 20% RM257, 7.5% chiral dopant and balance E7 before polymerization. (Yellow arrows indicate the locations of the disclination lines.)

The CLC-templated films to be used as sensors were treated with ethanol to extract the unreacted monomers and non-reactive mesogens. Before testing the films upon toluene exposure, we characterized their color using a UV-visible spectrophotometer. We recorded visible light transmission spectra of the flat films with various chiral dopant concentrations before and after polymerization, and after extraction, where examples for 20% chiral dopant are shown in Figure 4.2.b. Then, we plotted the transmission minima as a function of the chiral dopant concentration as shown in Figure 4.2.a. At high chiral dopant concentrations (15-25%), the reflected wavelength of light measured from the films before and after polymerization was in the visible region. With extraction, pitch size decreased with shrinkage which resulted in the shift of reflected wavelength of light to the invisible region (ultraviolet). At lower chiral dopant concentrations (5-10%), the reflected wavelength of light from the film was in infrared region before and after

polymerization. With the extraction of unreacted mesogens, shrinkage resulted in the shift of reflected wavelength to the visible region. Therefore, we can conclude that all regions of the flat and strained films became compressed upon extraction of unreacted mesogens as compared to the initial natural pitch size. Moreover, according to the wavelength shift observed in Figure 4.2.a, we estimated a shrinkage of 45% which can be considered as strain in the compression direction induced by extraction in addition to the strain introduced on the cholesteric helix via wedge cell (see Appendix A for more detail). Furthermore, according to the measurements we performed before polymerization and after extraction of strained film, radius of disclination lines decreased by 2.8 ± 1.3% with extraction. These shrinkage amounts are important in the calculations of the elastic energies that we explained below. We also note that the CLC-templated polymeric films exhibited mesoporous structure, with a mean pore diameter of 74.5 ± 30.1 nm, resulting from the extraction of the unreacted mesogens (Figure 4.2.d). This morphology contributed to a fast response due to higher surface area for the diffusion of organic compound.[24,103]

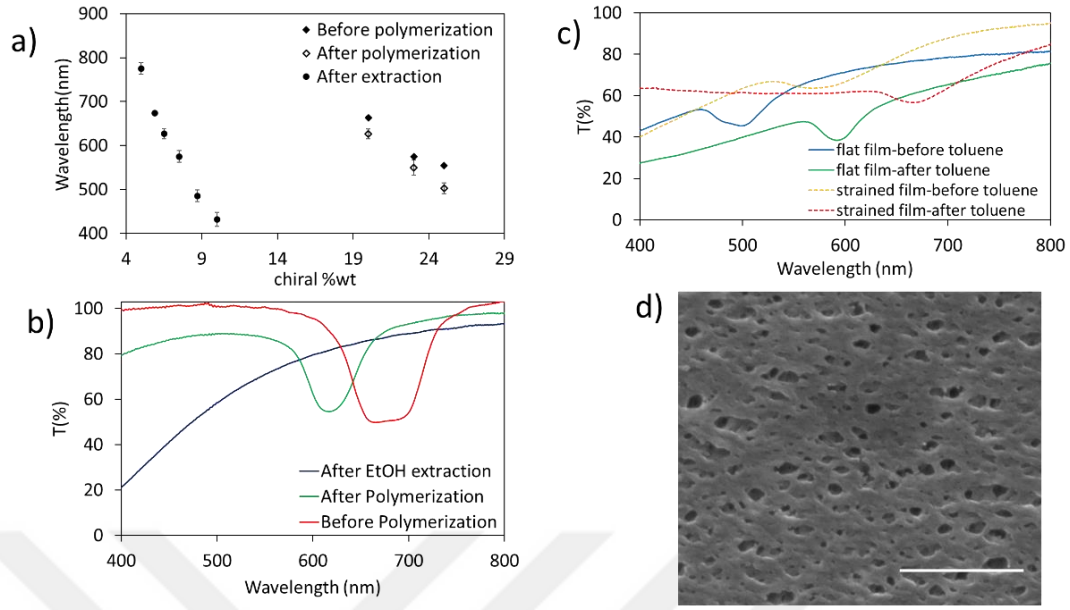


Figure 4.2 (a) The plot of the peak wavelengths of the films synthesized from 20% RM257, chiral dopant and balance E7 before polymerization, after polymerization and after extraction as a function of the concentration of chiral dopant, (b) UV-visible spectrum of a CLC film synthesized from 20% RM257, 20% chiral dopant and balance E7 before polymerization, after polymerization and after extraction , (c) UV visible spectrum of CLC-templated, extracted polymeric films synthesized from 20% RM257, 7.5% chiral dopant and balance E7 before and upon toluene exposure, (d) SEM image of CLC-templated polymeric film synthesized from 20% RM257, 7.5% chiral dopant and balance E7 after extraction of unreacted mesogens, scale bar: 1 μm.

#### 4.1.1.2 Response of polymeric films to toluene vapor

For toluene sensor tests, first, polymeric flat films synthesized from 20% RM257, 7.5% chiral dopant and balance E7 were placed in the exposure chamber and toluene vapor was introduced at known concentrations. Then, reflection mode polarized micrographs were collected at steady state, which took less than two minutes to reach. We observed a red shift of reflected color from flat films as shown in Figure 4.3.a,b. With this observation, we evidenced the CLC-templated polymeric flat film to be responsive against toluene vapor; however, to be able to serve at low exposure limitation of toluene as determined by OSHA, sensitivity of the sensor should be improved. To achieve desired sensitivity, we prepared strained films which we

hypothesize to enhance response with the contribution of stored elastic energy as compared to flat film.

In strained films, we identified three different regions which reflected different colors depending on the amount of strain on the cholesteric axis as described above. Although all these three regions are compressed due to the shrinkage as described above; total magnitude of compression on the regions changes depending on the amount of additional strain introduced by the wedge cell. Therefore, we identified these regions as high-, medium- and low-compressed regions. In the films synthesized from mixtures of 20% RM257, 7.5% chiral dopant and balance E7, medium-compressed regions appeared yellow-green (color of the flat film) while high-compressed regions appeared blue-green and low-compressed regions appeared red (Figure 4.3.c). In all these three regions, we observed a red shift of reflected color upon toluene exposure as shown in Figure 4.3.d (Appendix B. 1). Consistent with the range of reflection colors, we observed wider peaks in UV-visible light transmission spectra of the films before and upon toluene exposure (in the red and yellow dash lines as compared to green and blue lines in Figure 4.2.c). It is worth noting that the color change was only in a direction from shorter to longer wavelengths due to the increase of the pitch size with the sorption of toluene. Since the strain was in compression mode in all three regions of the film, sorption of toluene led to the release of strain and contributed to the increase of the pitch size. We reasoned that the extend of this red shift could be dependent on the magnitude of strain. A detailed analysis of that dependency required the spatial analysis of the coloring and strain. However, such information would not be available from visible light spectrophotometry measurements. Thus, below we continue with the response analysis from the optical micrographs.

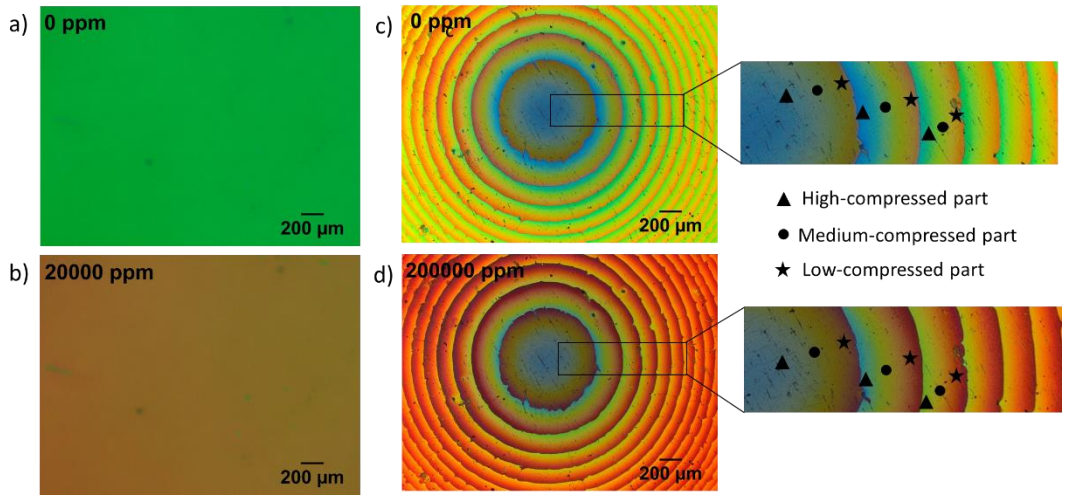


Figure 4.3 Reflection mode polarized optical micrographs of CLC-templated polymeric films synthesized from 20% RM257, 7.5% chiral dopant and balance E7. Flat film before (a) and upon (b) toluene exposure. Strained film before (c) and upon (d) toluene exposure.

In order to develop strain-response profiles during sensor tests, we first set out to establish a relationship between the coloring and strain (or pitch size) of the cholesteric pitch of the polymer synthesized from CLCs. Thus, we developed an understanding of the strain profile of the polymeric films and related to coloring. Firstly, strain map of CLC film in wedge cell (.a) was developed using a model based on the twist part of the elastic energy (details can be found in Appendix.A).[106] We have described above that 45% shrinkage in helical axis and 2.8 ± 1.3% decrease in the radius of the disclination lines were observed after the extraction of the unreacted mesogens. By combining this information with the strain map of CLC film before extraction calculated by elastic energy model (Figure 4.4.a), we developed the strain map of the strained polymeric films after extraction (dashed lines in Figure 4.4.a) where we identified the high-, medium- and low-compressed regions between two consecutive disclination lines. As shown, the maximum strain in compression mode (-63%) was observed in the high-compressed region of the first period, the magnitude of which decreases as the distance from center increases. Based on the calculated periodicity, we also developed a color map of the strained film by describing the colors corresponding to minimum and maximum strain between

disclination lines as illustrated in Figure 4.4.b which was consistent with the experimental micrograph shown in Figure 4.3.c. In order to obtain the relationship between strain and the sensitivity of the sensor, we initially analysed the selected areas from each of the three regions and determined the sensitivity signal using Eqn. 1 as a function of the toluene concentration and plotted the response curves.

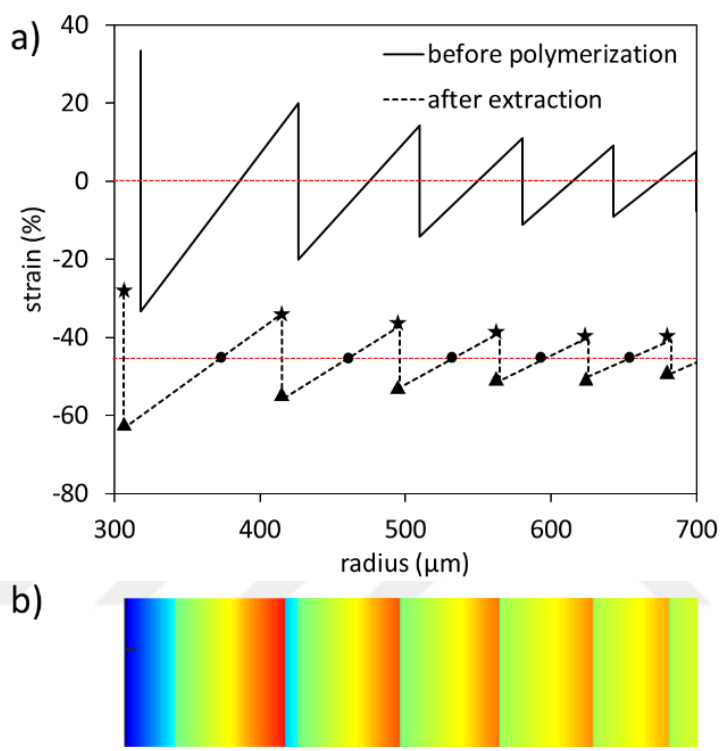


Figure 4.4 (a) Strain map of CLC in wedge cell (a) before polymerization and after extraction of unreacted mesogens (Star, circle and triangle symbols corresponds to low-, medium- and high-compressed regions shown in Figure 4.3.c, respectively). (b) Color map of CLC-templated polymeric film calculated from the elastic energy model.

We calculated the averages of sensitivity signals obtained from high-, medium- and low-compressed parts between first four disclination lines, and plotted in Figure 4.5. Inspection of Figure 4.5 led us to make three main initial observations. First, we observed monotonous increase in the signal for flat film and all the regions of the film synthesized in wedge cell consistent with the red shift upon toluene exposure. Second, the slope of the signal curves was affected from the region (thus the strain) where the measurements were taken, and high-compressed regions exhibited a

significantly higher response. Third, the relatively large error bars were observed in the sensitivity signals of high-compressed parts between first four disclination lines, which we hypothesized to be due to the significant variation in the magnitude of strain with the distance from the center as illustrated in Figure 4.4.a. Overall, according to the response measurements, increased sensitivity of the sensor by the introduction of strain to the polymeric film was apparent, and there is a significance evidence on the role of the magnitude of strain on the sensitivity of the film. Based on these critical observations, below we further investigate the dependence of the response on the magnitude of strain in more detail.

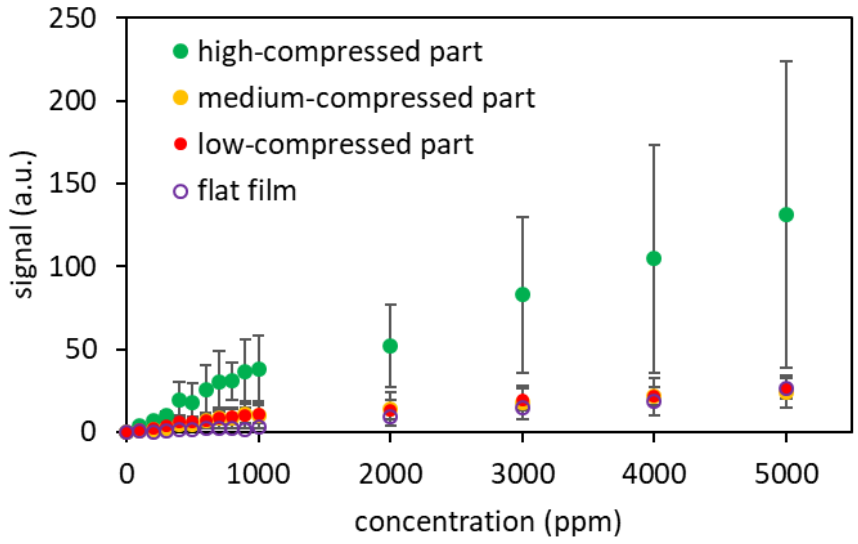


Figure 4.5 Response curves of flat film and strained film upon toluene exposure. The films were synthesized from 20% RM257, 7.5% chiral dopant and balance E7.

We conducted the following experiments in order to understand the relationship between strain and response. We synthesized films from mixtures of 20% RM257, 13% chiral dopant and balance E7 in a wedge cell so that high and low-compressed parts reflect dark blue (near ultraviolet) and blue color, respectively. In this way, we obtained only increase of the blue signal of the reflected color upon toluene exposure making the comparison more reliable using single color channel. Then, we have measured the response of an extracted flat film and obtained the reference signal without the influence of the additional strain (Figure 4.6.a,b). Finally, we measured

the response of the strained film (Figure 4.6.c,d) and analysed the sensitivity of high and low-compressed parts.

To illustrate the effect of the magnitude of strain on sensitivity of the films, we plotted the average slope of sensitivity curves of the flat film and the high- and low-compressed parts of the strained film (Fig. 6e) as a function of the strain calculated above (shown in Figure 4.4.a). We observed that sensitivity of the sensor is directly proportional to the amount of strain on the corresponding region of the film. Moreover, more pronounced response was observed in high-compressed regions while lowest response was observed in low-compressed regions at the vicinity of the first disclination line, which is consistent with the strain map of the film illustrated in Figure 4.4.a. Specifically, by varying the compressive strain from 28% to 63%, the amount of stored elastic energy within our polymeric film was increased which enabled us to improve the sensitivity by ~15×. This variation in the sensitivity with strain also explains the large deviations we observed in the averaged signals that were highlighted in Figure 4.5.

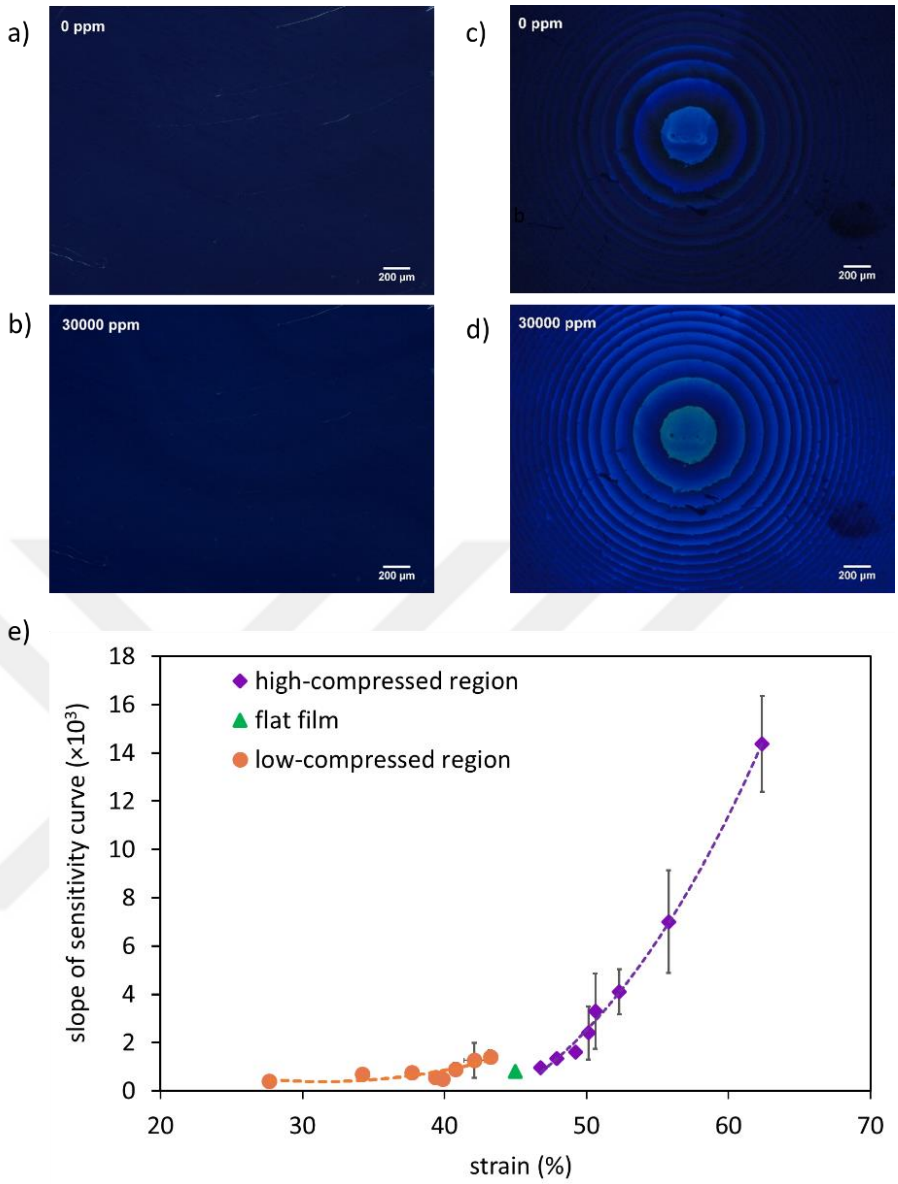


Figure 4.6 Reflection mode polarized optical micrographs of flat film synthesized from 20% RM257, 13% chiral dopant and balance E7 (a) before and (b) upon toluene exposure. Reflection mode polarized optical micrographs of strained film (c) before and (d) upon toluene exposure. (e) Slope of response curve with respect to strain.

With the experiments we conducted, we demonstrated the enhancement of sensitivity of sensor by the introduction of strain. Lastly, we conducted sensor tests which may simulate the real time use of our sensor. In these experiments, we introduced toluene to the system as step inputs of 500 ppm with the profile shown with the straight lines in Figure 4.7, to observe the response time and reusability of the sensor. Specifically,

we first collected reflection mode polarized light micrographs for 5 minutes under vacuum. Then, we introduced 500 ppm of toluene to the system and collected micrographs for 10 minutes. Finally, we applied vacuum and took micrographs for 5 more minutes. This procedure was repeated 3 cycles for 3 independent samples and the averages were plotted for high-compressed parts with the standard deviations in Figure 4.7. According to step response results, for high-, medium- and low-compressed parts, 90% of the maximum response was observed at 47.3 ± 16.2, 70±30.1 and 82±77.7 s, respectively. Therefore, we can conclude that, equilibrium was achieved approximately within the first minute of exposure for hig-compressed parts. Moreover, we proved the reusability of our sensor as we did not observe a significant decrease of the sensitivity during cyclic experiments. Furthermore, we exposed our sensors to 500 ppm toluene for 10 minutes (total exposure: 300000 ppm.s) and we observed 100.8 ± 22.1%, 95.9±8.2% and 100.2±15.4% of the theoretical response for high-, medium- and low-compressed parts of our sensor which proves the accurate cumulative exposure measurements.

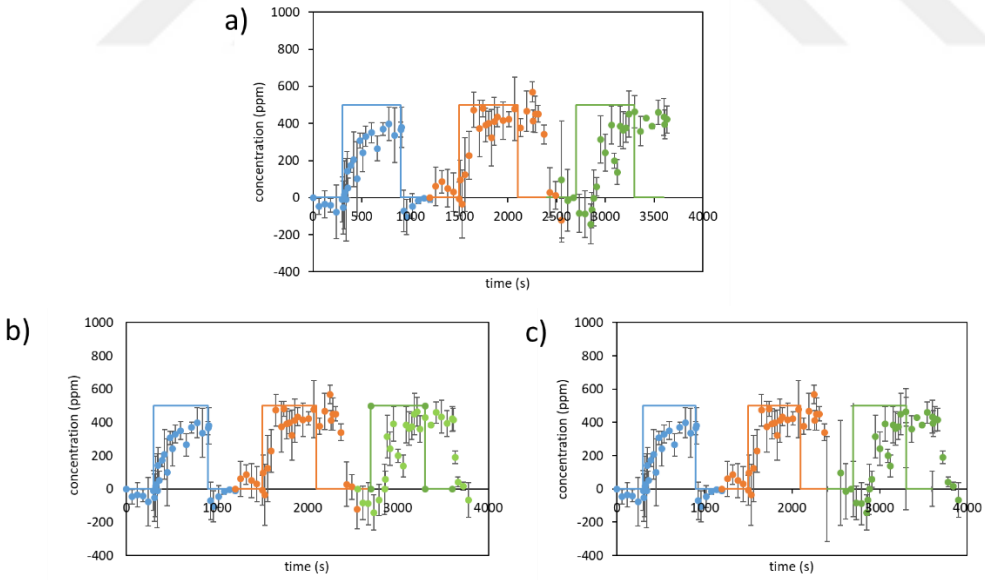


Figure 4.7 The response measurements of the (a) high-, (b) medium- and (c) low-strained regions of the films synthesized from 20% RM257, 7.5% chiral dopant and balance E7 that are exposed to cyclic concentration profiles of toluene. Straight lines indicate the exposed concentration profile of the toluene. Error bars indicate the standard deviation of the three independent measurements.

All the data we showed up to this point was obtained by image processing which we explained in detail in the experimental section. However, change in the wavelength of the reflected light upon toluene exposure can also be measured by using UV spectrophotometer as given in the literature[22,24,25,28,29]. Therefore, we also used UV spectrophotometer integrated to optical microscope for collecting sensor signals in terms of wavelength shift. We firstly took micrographs (Figure 4.8) with 100x magnification and collected the UV-visible spectra of high-, medium-, and low-compressed parts of the region 1 (between 1st and 2nd disclination line) and the 5 regions between 2nd to 6th disclination lines (Figure 4.9) before and upon 500, 1000, 5000 ppm toluene exposure. UV-spectra results showed that no significant wavelength shift was observed until 5000 ppm (~5%) toluene exposure which is too high as compared to our target concentration range (0-500 ppm).

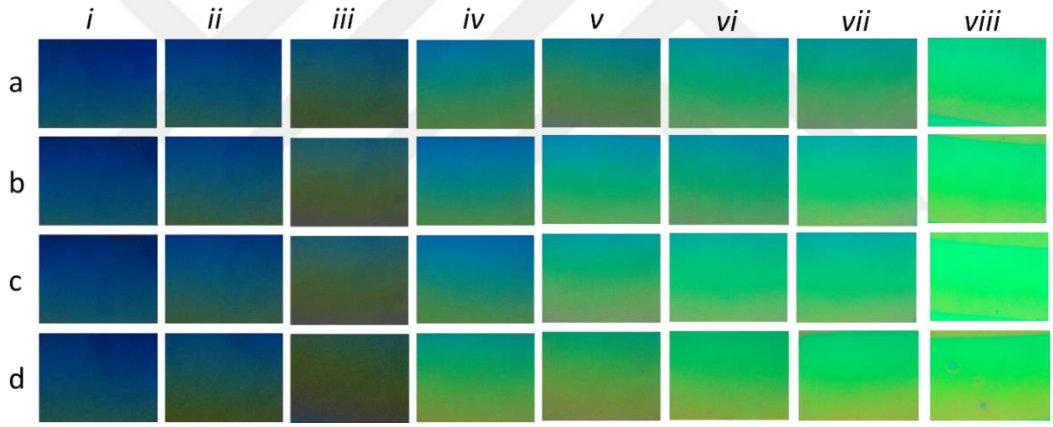


Figure 4.8 Reflection mode polarized optical micrographs of high- (i), medium- (ii) and low-compressed (iii) parts of region 1 and the regions between 2nd to 7th disclination lines (iv-viii) upon 0 ppm (a), 500 ppm (b), 1000 ppm (c) and 5000 ppm (d) toluene exposure.

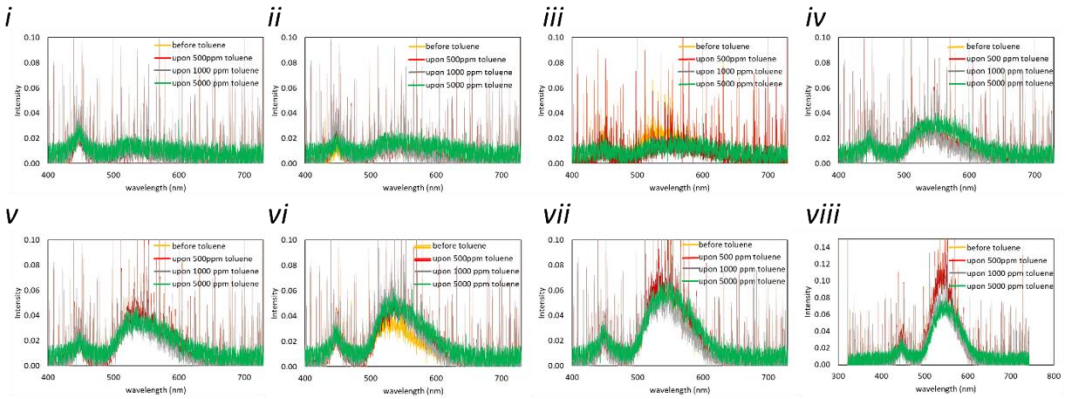


Figure 4.9 UV-visible spectra of high- (i), medium- (ii) and low-compressed (iii) parts of region 1 and the regions between 2nd to 7th disclination lines (iv-viii) upon 0 ppm, 500 ppm, 1000 ppm and 5000 ppm toluene exposure.

We also conducted 0 ppm to 500 to 0 ppm, 0 ppm to 1000 ppm to 0 ppm and 0 ppm to 5000 ppm to 0 ppm cycles and collected UV-visible spectra. We observed that with the removal of up to 5000 ppm toluene from the system, the reflected color (Figure 4.10) and wavelength (Figure 4.11) of the film turned back to its initial state; therefore, the proposed sensor can be used several times for <5000 ppm exposure ranges.

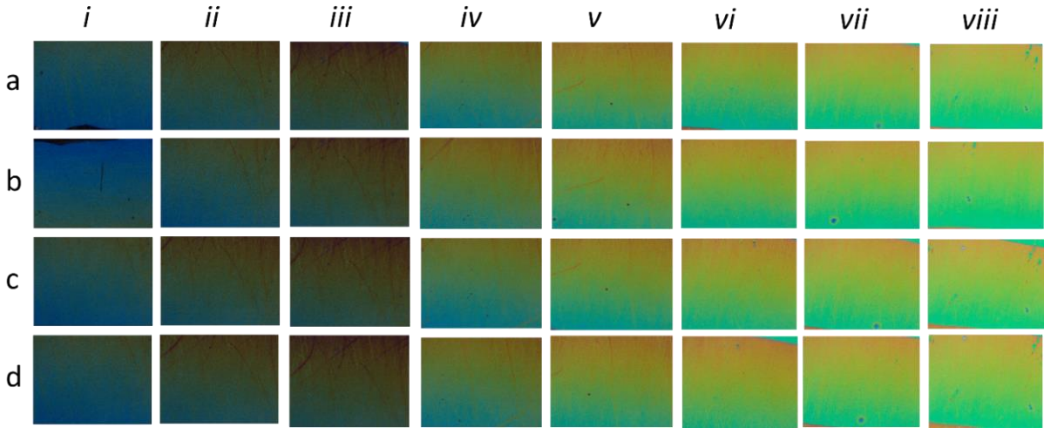


Figure 4.10 Reflection mode polarized optical micrographs of high- (i), medium- (ii) and low-compressed (iii) parts of region 1 and the regions between 2$^{nd}$ to 7$^{th}$ disclination lines (iv-viii) at 0 ppm (a) and after removal of 500 ppm (b), 1000 ppm (c) and 5000 ppm (d) toluene.

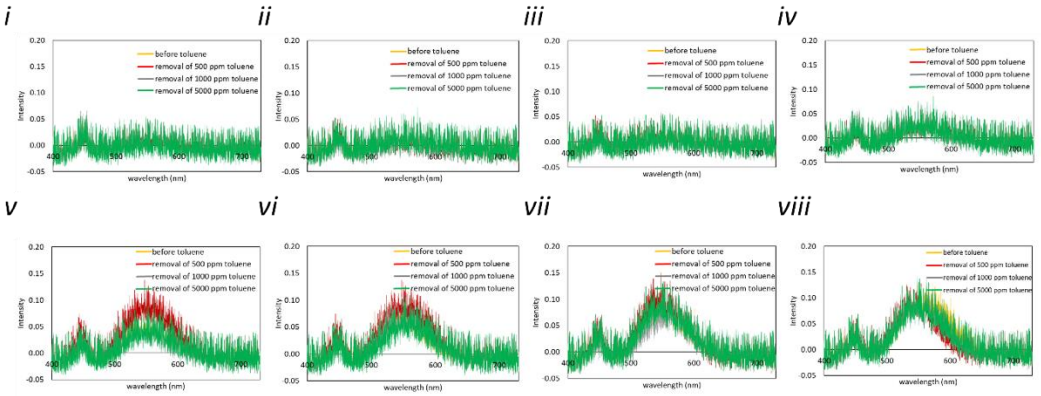


Figure 4.11 UV-visible spectra of high- (i), medium- (ii) and low-compressed (iii) parts of region 1 and the regions between 2$^{nd}$ to 7$^{th}$ disclination lines (iv-viii) at 0 ppm (a) and after removal of 500 ppm, 1000 ppm and 5000 ppm toluene.

As we examine the usage of UV-visible spectrophotometer in terms of practicality and the data quality, we obtained the following results. Firstly, in this method, data processing took more time as compared to image processing. Secondly and more importantly, as we had to use high magnifications (100x) to investigate small areas of the film (high-, medium, and low-compressed regions), resolution and optical problems evolved with the microscope which prevents the collection of highly sensitive sensor signals. Therefore, we concluded that image processing will be more suitable for the data processing step of the sensor tests.

#### 4.1.1.3 Response of CLC-templated polymeric films to acetone vapor

As a second model molecule, we chose acetone which has potential usage in biomedical applications. For the purpose of comparing acetone and toluene sensitivities, synthesized polymeric strain films were divided into two equal parts and each part was exposed to acetone and toluene vapor at saturation pressure at room temperature and UV-visible spectrums were collected. When the spectrum shown in Figure 4.12 is examined, it was observed that the wavelength of the films exposed to toluene (23% wavelength shift) increased more than those exposed to acetone (9% wavelength shift).

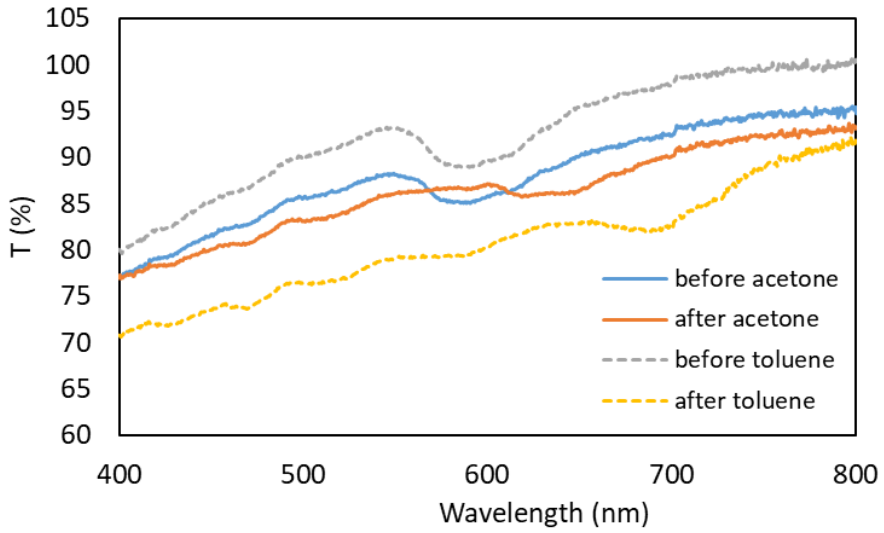


Figure 4.12 UV-visible spectrum of CLC-templated polymeric films synthesized from 20% RM257, 7.5% chiral and equilibrium E7 before and after exposure to toluene and acetone.

Sensor tests were carried out to examine the sensitivity of polymeric strained films against acetone and toluene vapor in more detail. Polymeric strained films were divided into two equal parts, placed in the exposure chamber at room temperature and exposed to known concentrations of acetone (Figure 4.13.a,b) and toluene (Figure 4.13.c,d). Then, reflection mode polarized micrographs were collected at steady state, which took less than two minutes to reach. With the processing of only high-strain regions of the images obtained as a result of 3 sets of sensor tests, the change in sensitivity signal depending on toluene and acetone concentration was obtained (Figure 4.13.e). When the sensitivity curves are examined, we observed that the sensor shows higher sensitivity to toluene vapor.

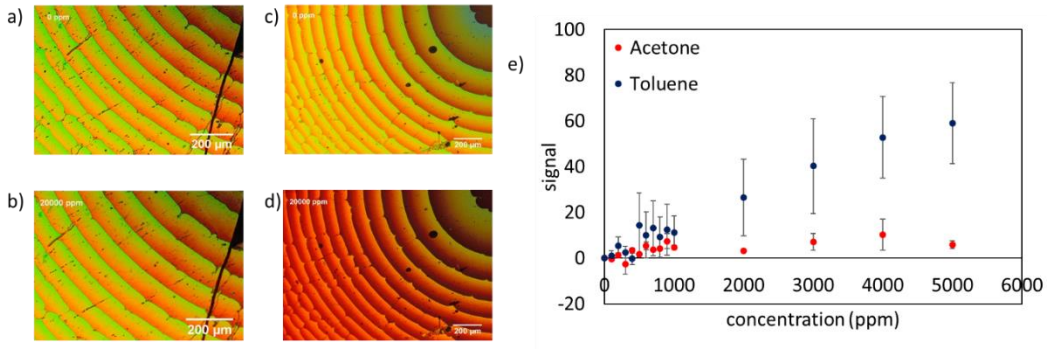


Figure 4.13 Reflection mode polarized optical micrographs of CLC-templated polymeric films synthesized from 20% RM257, 7.5% chiral dopant and equilibrium E7. Strained film (a) before and (b) after acetone exposure. Strained film before (c) and (d) after toluene exposure. (e) Response curves of high-compressed regions of strained films exposed to toluene and acetone.

We have also conducted sensor tests for both acetone and toluene which may simulate the real time use of our sensor. In these experiments, we introduced toluene to the system as step inputs of 2000 ppm with the profile shown with the straight lines in Figure 4.14, to observe the response time and reusability of the sensor. Specifically, we first collected reflection mode polarized light micrographs for 5 minutes under vacuum. Then, we introduced 200 ppm of toluene to the system and collected micrographs for 10 minutes. Finally, we applied vacuum and took micrographs for 5 more minutes. This procedure was repeated 3 cycles for 3 independent samples and the averages were plotted for high-compressed parts with the standard deviations in Figure 4.14. 90% of the maximum response was observed against toluene at 33.3 ± 5.8 seconds and against acetone at 203.3 ± 58.2 seconds. Therefore, we can conclude that, equilibrium was achieved approximately in the first minute of exposure to toluene and in the fourth minute upon acetone exposure. Moreover, we proved the reusability of our sensor as we did not observe a significant decrease of the sensitivity during cyclic experiments. Furthermore, we exposed our sensors to 2000 ppm toluene for 10 minutes (total exposure: 1200000 ppm.s) and we observed 113.4% and 83.6% of the theoretical response for high-compressed parts of our sensor upon toluene and acetone exposure, respectively, which proves the accurate cumulative exposure measurements.

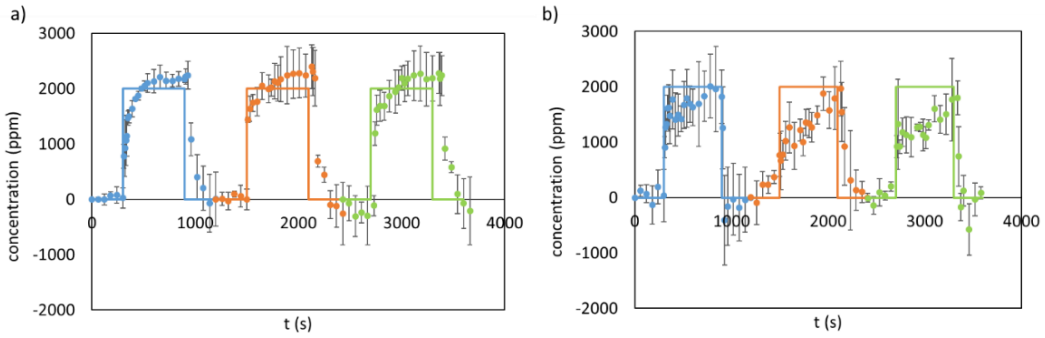


Figure 4.14 The response measurements of the high-strained regions of the films synthesized from 20% RM257, 7.5% chiral dopant and balance E7 that are exposed to cyclic concentration profiles of (a) toluene and (b) acetone. Straight lines indicate the exposed concentration profile of the vapor. Error bars indicate the standard deviation of the three independent measurements.

### 4.1.2 Interpenetrating Network Based Polymeric Sensors with Enhanced Specificity, Sensitivity, and Reusability

#### 4.1.2.1 Synthesis and characterization of IPN films

We first aimed to synthesize IPN films. After polymerization of CLC mixtures, unreactive mesogens were extracted with ethanol which results in a porous structure.[51] We note here that our past studies showed a substantial shrinkage to occur, as an outcome of the closure of the pores, if the ethanol was evaporated from the films after extraction.[51] Thus, to develop an IPN of PDMS and poly(RM257) polymeric films, we modified the previous method such that PDMS precursor-curing agent mixture was dropped without pressing on the CLC-templated poly(RM257) polymeric film immediately after the extraction of unreactive mesogens to fill the pores before evaporation of ethanol and to prevent shrinkage of the polymeric film as illustrated in Figure 4.15. Detailed synthesis procedure was illustrated in Figure 3.2.

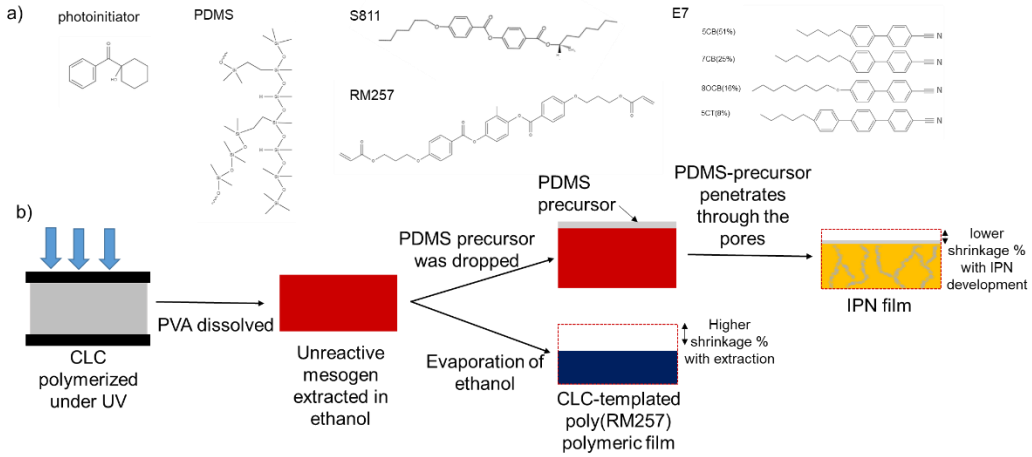


Figure 4.15 (a) Chemical structures of the molecules used in preparation of IPN film. (b) Schematic illustration of the preparation of IPN films. Sketches represent the side view of the film and colors represent the reflection colors of the films.

The possible paths of PDMS after being dropped on CLC-templated poly(RM257) film are given in Figure 4.16. PDMS precursor can follow three different paths after being dropped; PDMS precursor may not penetrate through the pores (Figure 4.16.i), PDMS may partially fill the pores (Figure 4.16.ii) or PDMS precursor completely fill the pores (Figure 4.16.iii). This step is important to achieve complete filling of the pores within the depth of the films under investigation, thus, we have provided enough time at this step for filling, then polymerized to maintain the final structure of the IPNs. Further characterization details to support these follows below.

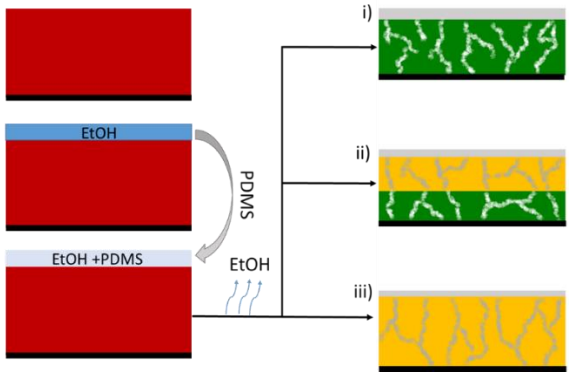


Figure 4.16 Schematic illustration of the possible paths of PDMS after being dropped on CLC-templated poly(RM257) film; (i) when PDMS does not penetrates into the pores, (ii) when PDMS partially penetrates into the pores, (iii) when PDMS fully penetrates into the pores (side view).

In order to prepare IPN films, we first proposed 3 different methods; by casting and curing PDMS precursor-curing agent on polymeric film for 2 days at room temperature and pressure (method 1), spin-coating and curing PDMS precursor-curing agent on polymeric film for 2 days at room temperature and under vacuum (method 2), and embedding polymeric film in PDMS precursor-curing agent and curing for 2 days at room temperature and under vacuum (method 3) and compared their effectiveness. Top and bottom surfaces' reflection mode polarized micrographs and UV-visible spectra of cured samples were collected and illustrated in Figure 4.17.a,b,c. For all the methods, same color signal was obtained from top and bottom surfaces which proves homogenous shrinkage, thus color distribution throughout the thickness of the film and successful penetration of PDMS into the pores. Moreover, no significant difference between penetration efficiency of these three methods was observed as the reflected wavelength of the cured samples are very similar (Figure 4.17.d) where multiple peaks resulted from non-homogenous blue-green color appearance of the film were observed in UV-visible spectra. As a result, we showed that the scenario illustrated in Figure 4.16occurs as PDMS completely fills the pores and we decided to prepare IPN films by the easier 1$^{st}$ method. To further verify the successful preparation of IPN films, we carried out characterizations using FTIR, DSC, UV-visible spectrophotometry, SEM imaging and nitrogen adsorption porosimetry. First, we synthesized polymeric films from CLC mixture of 20% RM257, 20% chiral dopant and balance E7 which reflected red color with 625 nm peak wavelength (star in Figure 4.17.e). When the unraeacted mesogens were extracted, pitch size of CLC structure reduced which resulted in a ~25% decrease of the peak wavelength to 475 nm and blue color appearance as shown in UV-visible spectra (circle in Figure 4.17.e). After filling the pores of CLC-templated poly(RM257) polymeric films with PDMS precursor-curing agent mixture and following the slow curing process, 584 (triangle in Figure 4.17.e) and 565 nm (diamond in Figure 4.17.e) peak wavelength and orange and yellow appearance was observed, respectively. Therefore, amount of shrinkage was reduced to ~13% with filling the pores with PDMS which is consistent with the development of IPN

network. Here, we want to note that the percent shrinkage of PDMS upon curing at room temperature was reported as -0.13 ± 0.05%[109]; therefore, curing of PDMS does not have a significant effect on the wavelength shift observed in UV-visible spectra. DSC thermogram of the same film is shown in Figure 4.17.f. Consistent with the literature, poly(RM257) films exhibited glass transition ($T_g$) at around 112.3°C[49] which did not significantly change ($\Delta T_g$ <1°C) with development of IPN. This result showed that structure of poly(RM257) was conserved and constituents of IPN did not dissolve in each other. Lastly, we investigated the chemical structure of the cured PDMS, poly(RM257) and IPN films by FTIR analysis as shown in Figure 4.17.g. Cured PDMS samples showed peaks around 789–796 $cm^{-1}$ (−$CH_3$ rocking and Si-C stretching in Si-$CH_3$), 1020–1074 $cm^{-1}$ (Si-O-Si stretching), 1259–1260 $cm^{-1}$ ($CH_3$ deformation in Si-$CH_3$), and 2950–2960 $cm^{-1}$ (asymmetric $CH_3$ stretching in Si-$CH_3$).[110] For the poly(RM257) polymeric films, the peak around 1700 $cm^{-1}$ originates from the stretching of C=O bond present in RM257. Besides, the multiple peaks between 1000-1300 $cm^{-1}$ originate from stretching of C-O present in the ester groups of RM257.[103] When the IPN was developed between PDMS and poly(RM257) films, in addition to the multiple peaks between 1000-1300 $cm^{-1}$ due to poly(RM257) in the structure, we also observed multiple peaks between 500-1300 $cm^{-1}$ originated from PDMS. Therefore, the existence of PDMS after removing excess PDMS layer from the top of the film was confirmed by the signatures of FTIR.

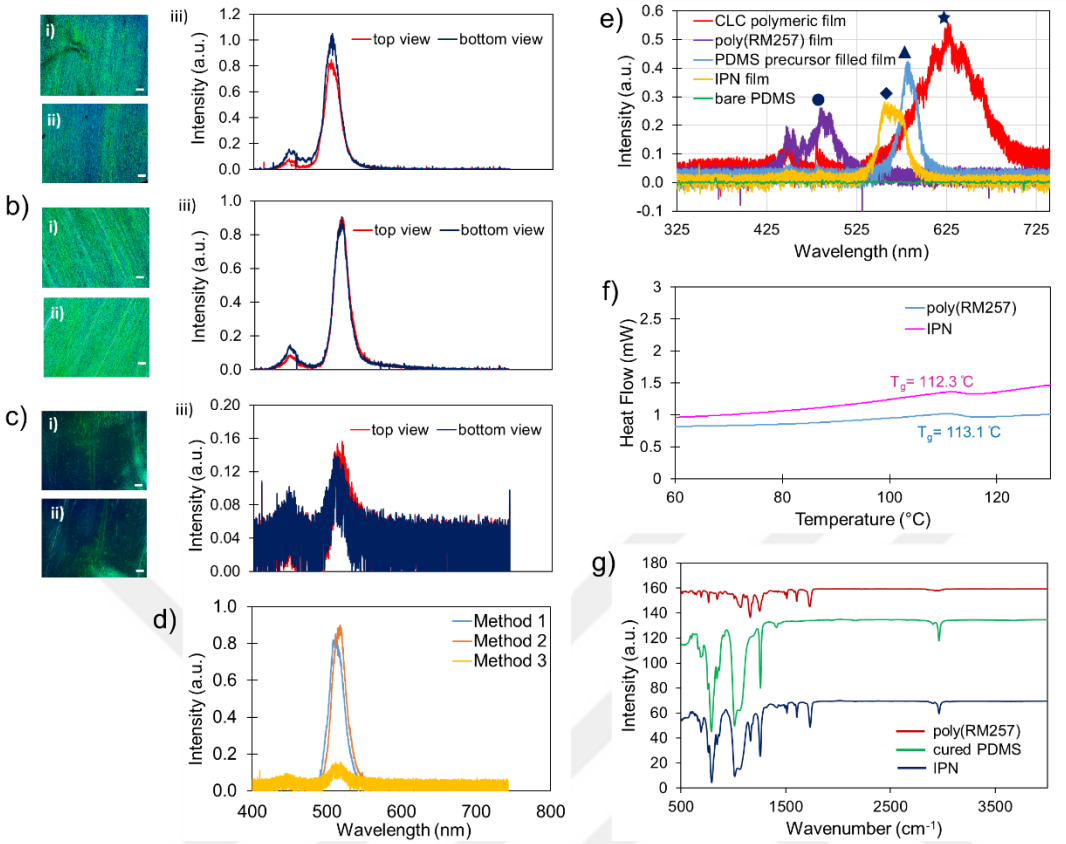


Figure 4.17 Reflection mode polarized micrographs of IPN film synthesized from 18.5% chiral, 20% RM257 and balanced E7 collected from (i) top surface, (ii) bottom surface and (iii) UV-visible spectra after; (a) casting and curing PDMS precursor – curing agent on polymeric film for 2 days at room temperature and pressure (method 1), (b) spin-coating and curing PDMS precursor-curing agent on polymeric film for 2 days at room temperature and under vacuum (method 2), (c) embedding polymeric film in PDMS precursor-curing agent and curing for 2 days at room temperature and under vacuum (method 3). (d) UV visible spectra of IPN films prepared by the methods in (a), (b) and (c). (e) UV-visible spectra of colors reflected from polymeric films. (f) DSC thermograms of poly(RM257) and IPN films. (g) FTIR spectra of the cured PDMS, poly(RM257) and IPN films. The polymeric films were synthesized from 20% RM257, 20% chiral dopant and balance E7. (scale bar: 200µm)

SEM images of surface of poly(RM257) film (Figure 4.18) revealed that extraction of unreactive mesogens to result in porous structure with average pore diameter of 74.5 ± 30.1 nm measured from the SEM images. With the filling of the pores with PDMS, we did not observe a porous structure on the surface in SEM images of IPN films (Figure 4.18.b). Moreover, cross-sectional SEM image of IPN films (Figure 4.18.c,d) showed homogenous appearance. Furthermore, the pore size range

measured from $N_2$ adsorption isotherms also confirmed the morphology observed in SEM of poly(RM257) with a pore size distribution between 20 to 120 nm (Figure 4.18.d), while such distribution was absent in IPN film (Figure 4.18.d inset). Overall, the FTIR analysis, SEM and BET results confirmed the development of IPN between PDMS and poly(RM257) polymeric structures, which we proceed with the response measurements below.

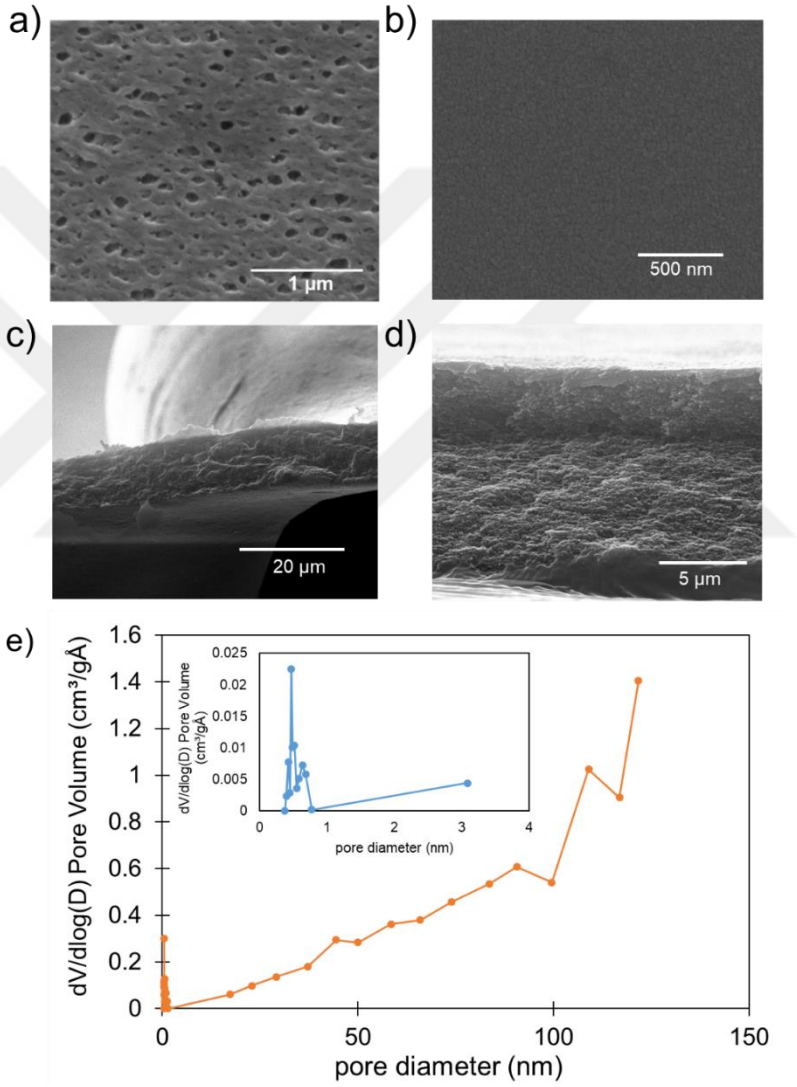


Figure 4.18 SEM images of (a) top view of CLC-templated polymeric film, (b) top view, (c,d) sectional view of IPN film after removing excess PDMS layer. (e) Pore size distribution of CLC-templated polymeric film calculated using BJH theory. Inset shows pore size distribution of IPN film. The polymeric films were synthesized from 20% RM257, 20% chiral dopant and balance E7.

#### 4.1.2.2 Sensor performance of IPN films

After characterization of IPN films, we first synthesized polymeric films from 20% RM257, 17% chiral dopant and balance E7 and the excess PDMS layer on the polymeric film was removed to reduce the resistance for mass transfer.

In order to investigate the consistency and reusability of IPN between PDMS and poly(RM257) and compare with the poly(RM257) film, a three-step sequential experiment was performed. We first measured the response of the polymeric films against our first model molecule, toluene for concentrations up to 5000 ppm. After equilibrating the samples under vacuum, we performed the second measurement up to the saturation concentration of toluene, ~30000 ppm which is known to plasticize RM257.[103] Lastly, we repeated the measurement up to 5000 ppm after evacuation to compare with the first run. Then, we compared the change in sensitivity signals of 3 different samples and the reflection coloring of the polymeric films at the end of each run (Figure 4.19). We observed the poly(RM257) polymeric films to exhibit a red shift upon exposure to low concentrations and then a blue shift that recovered to their initial coloring after evacuation of the system from toluene Figure 4.19.a, run 1). However, when the system was exposed to high concentrations of toluene and evacuated (run 2), the films did not recover to their original color (blue-shifted inhomogeneous appearance, as shown in bottom, middle image in Figure 4.19.a). This result is an indicative of the release of the elastic energy stored within the polymer network due to plasticization at high concentrations of toluene which resulted in a permanent set in the network, consistent with the literature.[49] Additionally, after destruction of poly(RM257) structure due to plasticization, we did not observe a meaningful response upon toluene exposure in run 3 as also illustrated in the response curves. This indicates that exposure of the non-IPN, CLC-templated sensors to high concentrations of toluene renders them unusable. For IPN films, exposure to low toluene concentrations resulted in a red shift of coloring which recovered to their initial appearance after evacuation of toluene (Figure 4.19.b, run 1). When the films were exposed to high toluene concentration in run 2, a red shift

was observed which reached to invisible wavelengths. After removal of toluene, contrary to non-IPN counterparts (poly(RM257)), the films with IPN structures recovered back to their initial coloring indicative of the totally preserved structure of the film with the elastic swelling of PDMS. Additionally, as also shown in the response curves, when the system was exposed to toluene vapor in run 3, no significant loss of sensitivity was observed that the desired reusability was achieved. Overall, the development of IPN structure enhanced the durability and reusability of the poly(RM257) polymeric sensors.

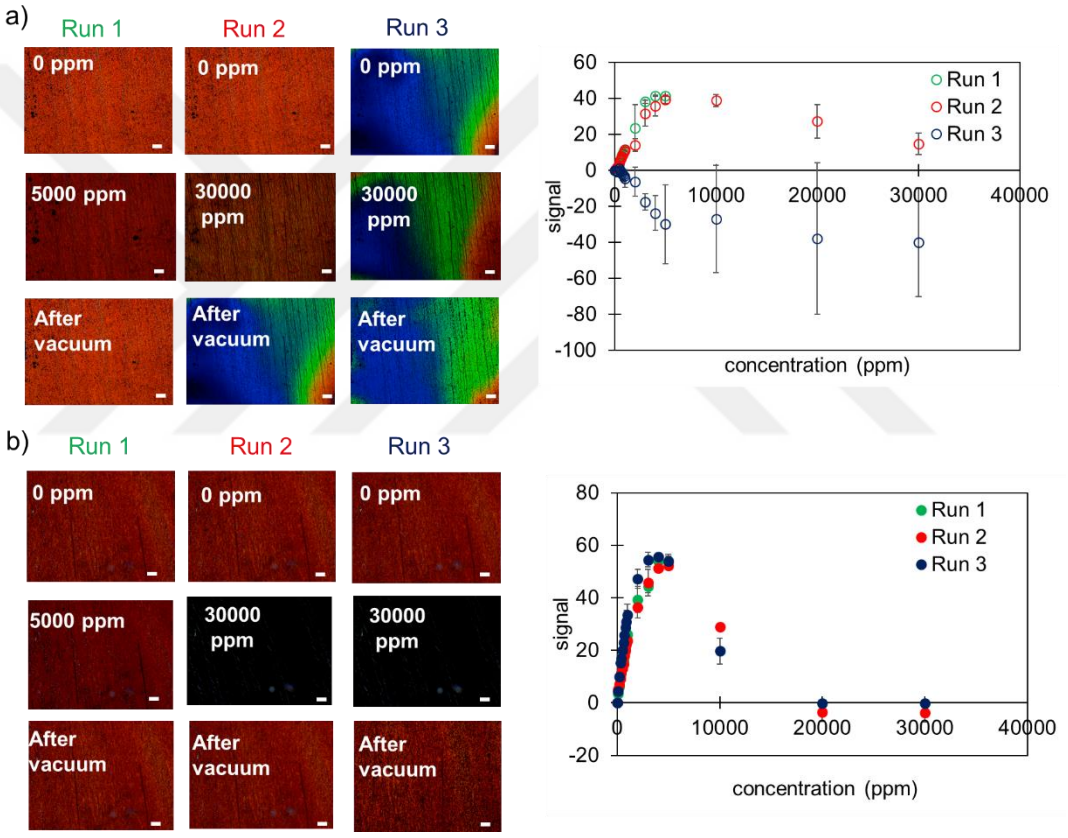


Figure 4.19 Response characteristics of the (a) poly(RM257), (b) IPN films upon exposure to different concentrations of toluene. Top nine images show the reflection-mode polarized light micrographs of each sample collected at the indicated conditions within each run indicated at the top of the columns. The plots show the average signals of 3 different samples calculated from images collected in each run. (scale bar: 200µm).

To measure the sensor performances upon exposure to vapors of VOCs, we chose toluene, hexane, acetone, ethanol and also water which is always present in the potential environments as humidity. The sensor tests were carried out against our five model molecules for both poly(RM257) polymeric film and PDMS-poly(RM257) IPN film. The sensitivity signals of 3 different samples upon exposure to non-polar and polar molecules were obtained by Eqn. 1, and the averages were plotted with the standard deviations (Figure 4.20.a and b, respectively). Additionally, to clearly show the effect of IPN structure on sensor sensitivity, slope of sensitivity curves of poly(RM257) and IPN films upon VOCs and water vapor are illustrated as a bar chart in Figure 4.20.c. When we considered the sensor signals against non-polar solvents (Figure 4.20.a,c), we did not observe a significant response of poly(RM257) polymeric films upon exposure to hexane. However, interestingly, IPN films showed considerably enhanced response upon hexane with limit of detection (LOD) of 118 ppm in 0-1000 ppm concentration range. For toluene, poly(RM257) polymeric films showed high sensitivity which was slightly increased in IPN films with LOD of 60 ppm in 0-1000 ppm concentration range. When the sensitivity of polymeric sensors against polar solvents was examined (Fig. 4.b), we observed that both poly(RM257) polymeric films and IPN films showed no significant response against humidity, while poly(RM257) polymeric films showed very weak responses against ethanol which was not significantly affected with the development of IPN. Furthermore, for acetone, the mid-level response of poly(RM257) polymeric structure was slightly higher than the response of IPN structures. As labelled in Figure 4.20.c, we identified four cases of the change in the response of the films upon the development of the IPN, when compared to the non-IPN counterparts. We further discuss below the underlying phenomenon in these four cases that is useful for the specific identification of the vapors.

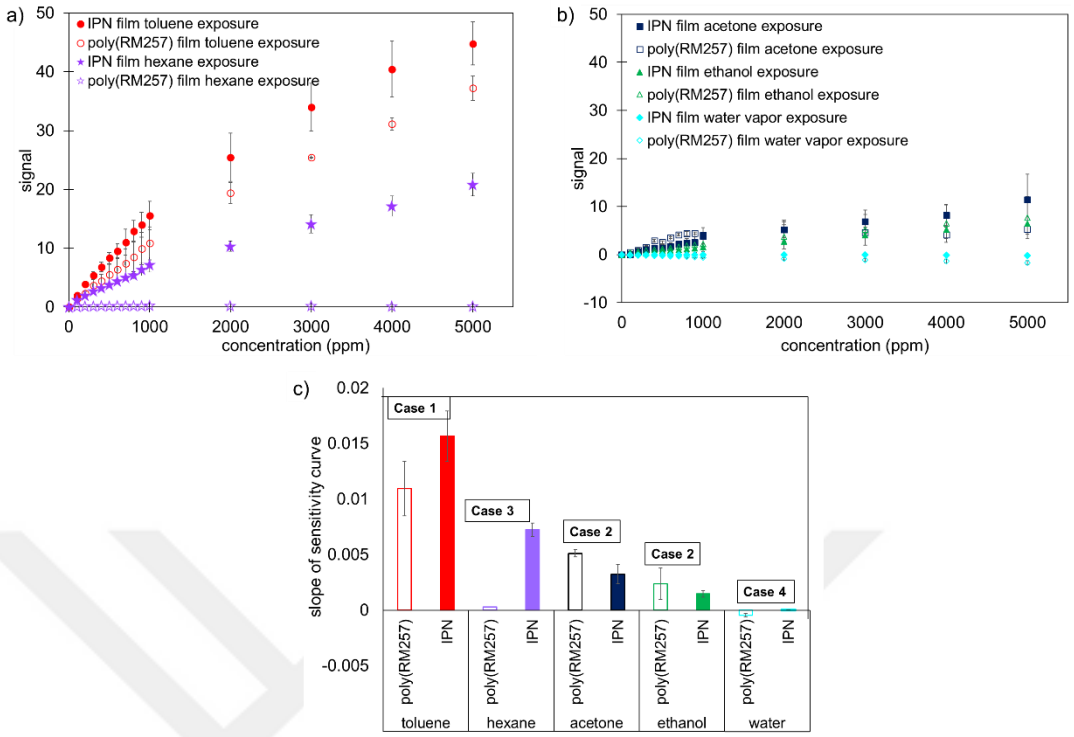


Figure 4.20 Response curves of poly(RM257) and IPN films upon (a)non-polar and (b)polar solvent vapors. (c) Slope of the sensitivity curves of poly(RM257) and IPN films upon non-polar and polar solvent vapors.

When poly(RM257) and IPN films were exposed to solvent vapors, 4 different cases may occur which we identified in Figure 4.20.c and Figure 4.21. The case 1 was the swelling of both PDMS and poly(RM257) polymeric structures against solvent vapor, which resulted in high swelling ratio of the IPN structure. Case 2 and case 3 occurred when one of the polymeric structures, either PDMS or poly(RM257), in the network swelled upon solvent vapor, which resulted in medium swelling of the polymeric structure. Lastly, case 4 took place when none of the polymeric structures in the network is swollen by the solvent vapor. All these four cases can be explained by the solubility parameter based affinity of poly(RM257) and PDMS against the solvent vapors.

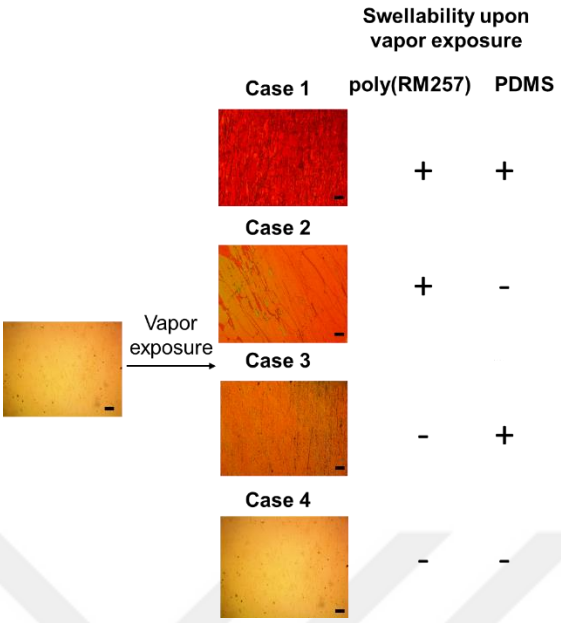


Figure 4.21 Possible response cases of IPN films upon vapor exposure. Micrographs were collected by reflection-mode optical microscope. (scale bar: 200µm).

When we examined our sensor test results illustrated in Figure 4.20.c together with these possible cases, we reached to the following conclusions. Against hexane, upon which poly(RM257) has almost no swellability, we did not observe any response from poly(RM257) polymeric film. With the development of IPN, we observed significantly enhanced response of IPN films with higher sensitivity curve slope due to high swellability of PDMS upon hexane exposure (case 3). In this case, although poly(RM257) film does not swell, PDMS swelled upon exposure to hexane which was reported by the color change of the CLC-templated polymeric structure. Therefore, IPN development in poly(RM257) by impregnation of PDMS earned response to a broader set of analytes. With toluene exposure, upon which both poly(RM257) and PDMS can swell, as indicated by case 1, highly sensitive response with high slope was obtained from poly(RM257) polymeric film which was slightly enhanced by IPN formation with PDMS. Upon acetone exposure, as poly(RM257) has good swellability while PDMS does not have significant swelling ability (case 2), the slope of the sensitivity curve was slightly decreased upon penetration of PDMS. Upon ethanol exposure, where neither poly(RM257) or PDMS did not

possess considerable swellability, we did not observe significant response from any of the two polymeric structures. Lastly, as neither poly(RM257) nor PDMS swells against water vapor, no response was observed with almost zero slope of sensitivity curve which is consistent with the case 4. Overall, we can conclude that, depending on the swelling behavior of the constituents of IPN, development of IPN can be used to enhance the specificity (as in the hexane case) or sensitivity (as in the toluene case) of the CLC-templated polymeric sensors.

Lastly, we conducted sensor tests which may simulate the real time use of our sensor and compare IPN and poly(RM257) polymeric film performances against toluene vapor. In these experiments, we introduced toluene to the system as three exposure-evacuation cycles of step inputs of 2000 ppm with the profile shown with the straight lines in Figure 4.22.a, to observe the response time and reusability of the sensor. Specifically, we first collected reflection mode polarized light micrographs for 5 minutes under vacuum. Then, we introduced 2000 ppm of toluene to the system and collected micrographs for 10 minutes. Finally, we applied vacuum and took micrographs for 5 more minutes. This procedure was repeated for 3 cycles for 3 different samples. According to step response results illustrated in Fig. 5a, upon toluene, 90% of the maximum response was observed at 45.3±13.2 s for poly(RM257) and 28.3±2.4 s for IPN. Therefore, we can conclude that IPN film has lower response time as compared to poly(RM257) polymeric film. Moreover, the results were also reported as the change in the sensitivity signal with time during real time experiments (Figure 4.22.b) which will be useful for the application of these sensors. Inspection of Figure 4.22.b together with Figure 4.22.a led us to show that IPN gave faster initial response and quickly reached equilibrium upon VOC exposure (rapid increase highlighted as “VOC input” in Figure 4.22.b) and immediately turned to initial state with VOC removal (dramatic decrease highlighted as “vacuum” in Figure 4.22.b) compared to poly(RM257). Furthermore, development of IPN decreased scattering of the sensitivity signals which is also crucial to improve the real time usage of the CLC-based polymeric sensors.

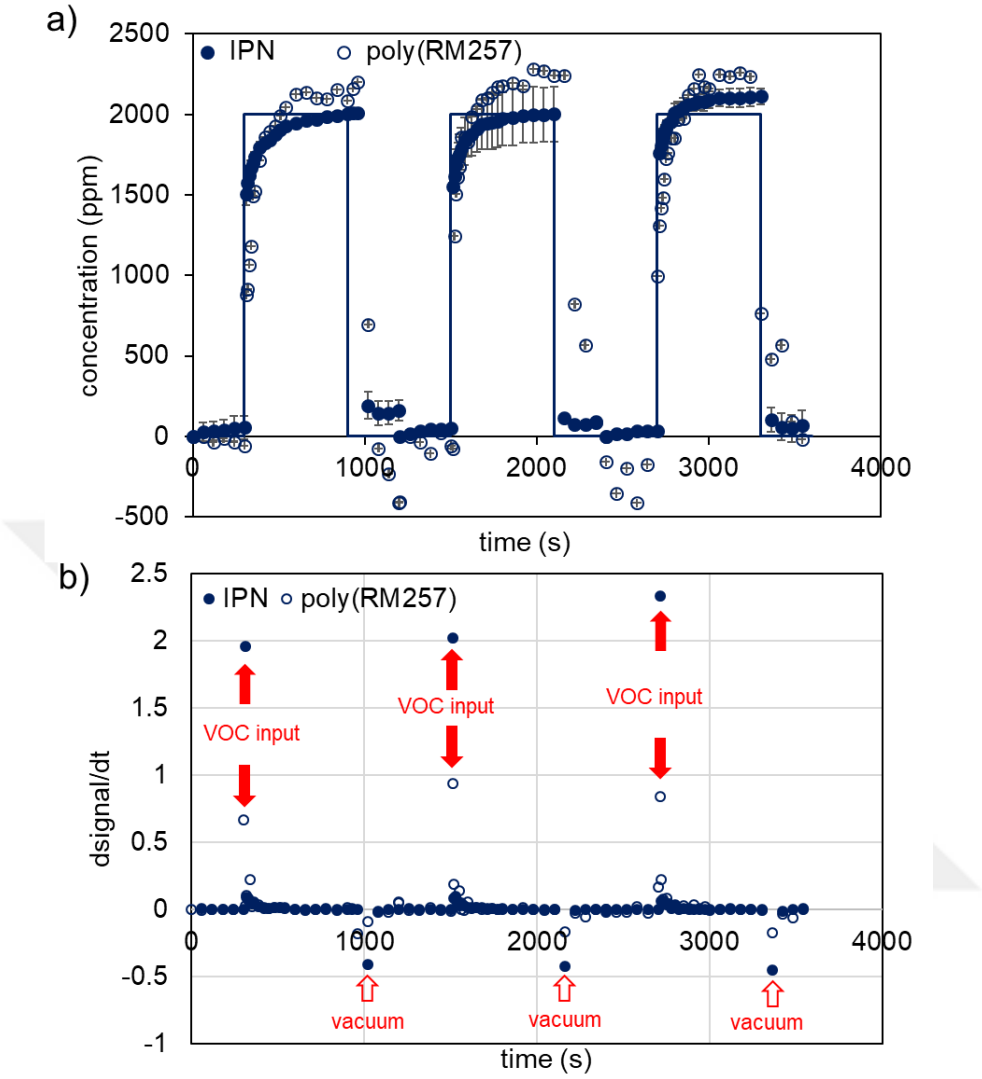


Figure 4.22 (a) Theoretical response (line), practical response (point) of PDMS-filled CLC-templated and CLC-templated polymeric films upon toluene input. (b) Change in the sensitivity signal of IPN and poly(RM257) with time during real time experiments.

Overall, in this work, we synthesized IPN based on poly(RM257) and PDMS by sequential impregnation pathway to be used as optical vapor sensor. The sensor performance was enhanced in terms of durability and reusability with the elastic swelling ability of PDMS upon high vapor concentration exposure. Moreover, sensor tests upon four VOCs and humidity revealed that there are four possible cases which may occur depending on the swelling ability of the constituents of IPN (Figure 4.21).

The most important inference of these cases was observed in the hexane case where poly(RM257) did not show any response while development of IPN significantly enhanced sensor sensitivity due to high swellability of PDMS. The distinct response of the IPN based sensors upon different external stimuli depending on affinity of constituents demonstrated that the specificity feature can be given to the CLC-based optical sensors by development of IPN.

## 4.2 Synthesis and Characterization of Chiral Reactive Metallomesogens

### 4.2.1 Characterization of chiral reactive metallomesogens

The molecule to be synthesized was designed such that the resulting molecule has chiral groups to use the advantage of chiral symmetry in possible applications together with reactive end groups which brings durability and ease of wearable technology integration. We first aimed to verify the molecular handedness of the opposite isomers of Pd-complex (3a-Pd and 3b-Pd) by circular dichroism (CD) and illustrated in Figure 4.23.a. CD spectra of the enantiomeric couples the isomers show the expected mirror-image relationship. 3a-Pd complex (R-isomer) exhibited a positive bisignate Cotton effect that, first with positive and then negative components at longer (450 nm) and shorter (310 nm) wavelengths, respectively. At the same time, 3b-Pd complex (S-isomer) exhibited a completely reversed CD behavior, which was first negative and then positive components at longer (450 nm) and shorter (325 nm) wavelengths.[111] The thermal behavior of metallomesogenic compound, Pd-3b was investigated by means of TGA and DSC analysis. In the DSC thermogram, Pd-3b complex exhibited glass transition temperature ($T_g$) at around 57ºC (Figure 4.23.b) which shows rubbery state above $T_g$ and glassy state below $T_g$. TGA profile under nitrogen atmosphere revealed that after evaporation of volatiles, 3b-Pd degrades from 200 to 440°C (Figure 4.23.c).

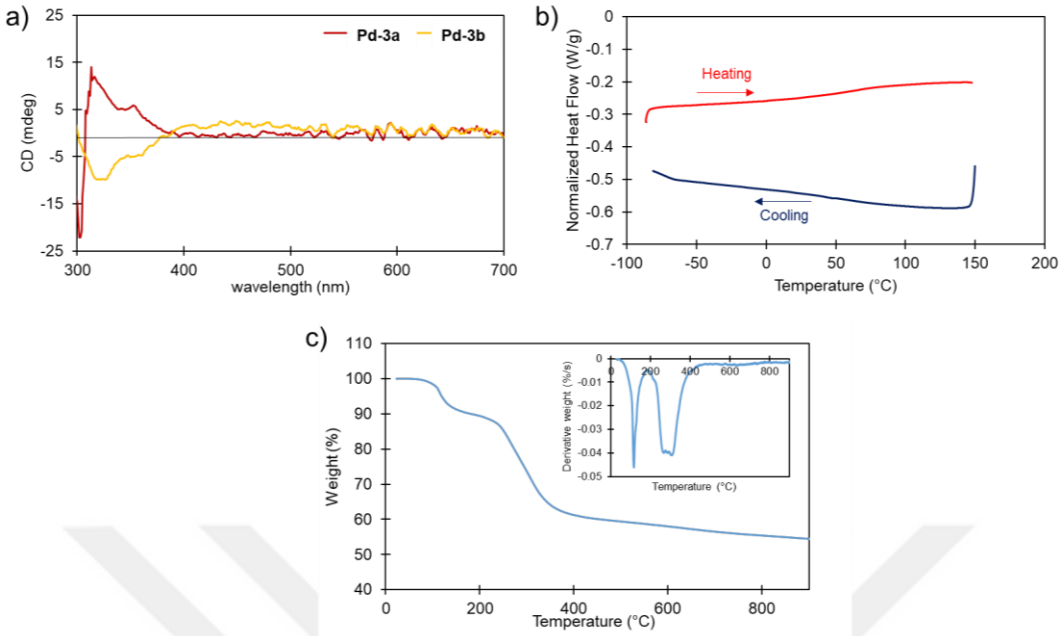


Figure 4.23 (a) Circular dichroism of Pd-3a and Pd-3b complexes. (b) Differential Scanning Calorimetry results of Pd-3a complex (2nd heating and cooling, 10°C/min). (c) Thermogravimetric analysis of Pd-3a complex under $N_2$ atmosphere (Inset shows differential thermal analysis results).

The chiral characteristics of the complexes were investigated by the optical characterizations. In the first part of the study, compound 3 was synthesized by R- and S-2-amino-1-butanol amino alcohols which creates chirality and complexed with Pd, Cu and Zn metals. The chemical structures of resulting molecules are illustrated in Figure 4.24.i,ii columns. With these experiments, we aimed to investigate effect of metal core type on the chiral characteristics of the complexes by determining the pitch size and HTP of the chiral complexes. Pitch size of a cholesteric structure can be measured by four different methods namely; Fingerprint (Lagarde method), Grandjean-Cano, Diffraction method or selective reflection.[112] In this study, we used Fingerprint (Lagarde Method) by confining the complex - 5CB nematic LC mixtures between homeotropically-anchored DMOAP coated glasses and imaging under reflection mode polarized optical microscope. When the cholesteric structures are in the homeotropic alignment, with the torque induced by chirality, the molecular helices are randomly wounded and irregular fingerprint textures are observed. Moreover, the spacing between equally distanced dark lines gives half pitch of the

cholesteric structure.[112] When we imaged different concentrations of Pd-3a, Pd-3b, Cu-3a and Cu-3b complexes - 5CB mixtures, we observed characteristic fingerprint textures in polarized optical microscopy images of resembling CLC phase at homeotropic orientation (Figure 4.24.a-d.iii). However, Zn complexes, Zn-3a and Zn-3b, cannot give periodicity to nematic LC (Figure 4.24.e-f.iii) since the tetrahedral Zn complexes are too labile to ensure the absolute configuration of the metal center[113] as also illustrated in 3D structures.

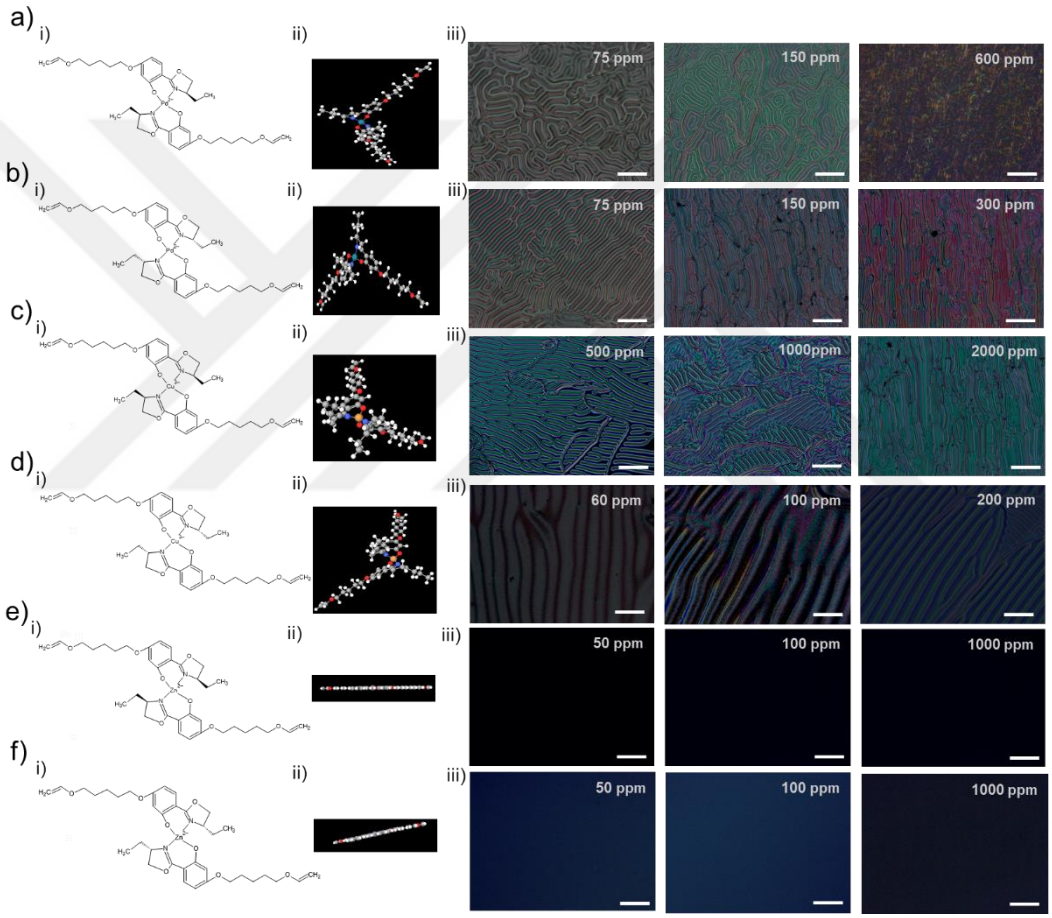


Figure 4.24 (a) Pd-3a, (b) Pd-3b, (c) Cu-3a, (d) Cu-3b, (e) Zn-3a, (f) Zn-3b complex (i) chemical structure, (ii) 3D chemical structure. Reflection mode polarized optical micrographs of complexes – 5CB mixtures sandwiched between DMOAP coated glasses. Scale bars: 200 μm.

The pitch size of the cholesteric structures was measured from optical microscopy images with respect to concentration of the complexes. By using the relationship

between HTP, chiral dopant concentration, and pitch size of the chiral compounds (Equation 1), HTP of Pd-3a, Pd-3b, Cu-3a and Cu-3b complexes were determined as 3.9, 2.8, 1.1 and 1.2 $\mu m^{-1}$, respectively (Figure 4.25, Table 4.1). HTP results revealed that metal center does have a significant impact on the chiral behavior as also reported in literature.[102]

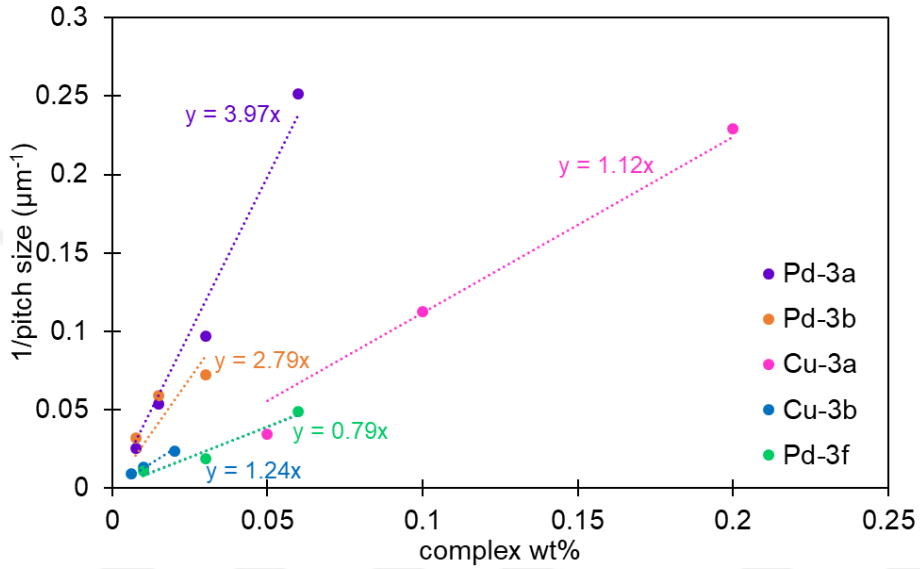


Figure 4.25 Pitch size of Pd-3a, Pd-3b, Cu-3a, Cu-3b and Pd-3f complexes – 5CB mixtures with respect to concentration.

Table 4.1 Helical Twisting Power (HTP) of complexes mixed with 5CB nematic LC.

| **Complex ID** | **HTP ($\mu m^{-1}$)** |
|---|---|
| Pd-3a | 3.9 |
| Pd-3b | 2.8 |
| Cu-3a | 1.1 |
| Cu-3b | 1.2 |
| Zn-3a | - |
| Zn-3b | - |

In the second task of our study, four more different amino alcohols ((S)-(+)-2-phenylglycinol, (R)-(+)-2-phenylglycinol, (S)-(-)-2-amino-3-phenyl-1-propanol and (S)-(+)-2-amino-3-methyl-1-butanol), see Appendix C.1 for the chemical structures) were used to synthesize compound 3 and complexed with Pd. The chemical structure of resulting molecules are illustrated in Figure 4.26.a-d.i,ii. By synthesis of these compounds, we aimed to investigate effect of chiral group type and length on chiral behavior of chiral reactive metallomesogens. As illustrated in Figure 4.26.a-d.iii, when Pd-3c, Pd-3d and Pd-3e complexes are mixed with 5CB, they did not give enough chirality to twist nematic LC as their mixtures did not exhibit cholesteric feature when sandwiched between DMOAP coated glasses (Figure 4.26.a-c). However, characteristic fingerprint textures were observed in polarized optical microscopy images of Pd-f complex (Figure 4.26.d.iii) with HTP of 0.7 $\mu m^{-1}$. The optical characterization results of the Pd complexes synthesized from amino alcohols with different chiral group length are summarized in Table 4.2. In the light of these results, we reached two main conclusions. Firstly, the complexes synthesized from the amino alcohols which has phenyl in their chiral group ((S)-(+)-2-phenylglycinol, (R)-(+)-2-phenylglycinol and (S)-(-)-2-amino-3-phenyl-1-propanol) either does not exhibit strong chiral behavior adequate to give chirality to 5CB nematic LC which is also observed in 3D structures. Secondly, we observed that increase of the chiral group chain length (from Pd complex synthesized from (R)-2-amino-1-butanol to (S)-(+)-2-amino-3-methyl-1-butanol) results in increase of pitch size and decrease of HTP from 3.38 $\mu m^{-1}$ to 0.79 $\mu m^{-1}$ due to greater affinity of shorter chiral group chain length complexes with 5CB nematic LC inducing higher HTP values.[102]

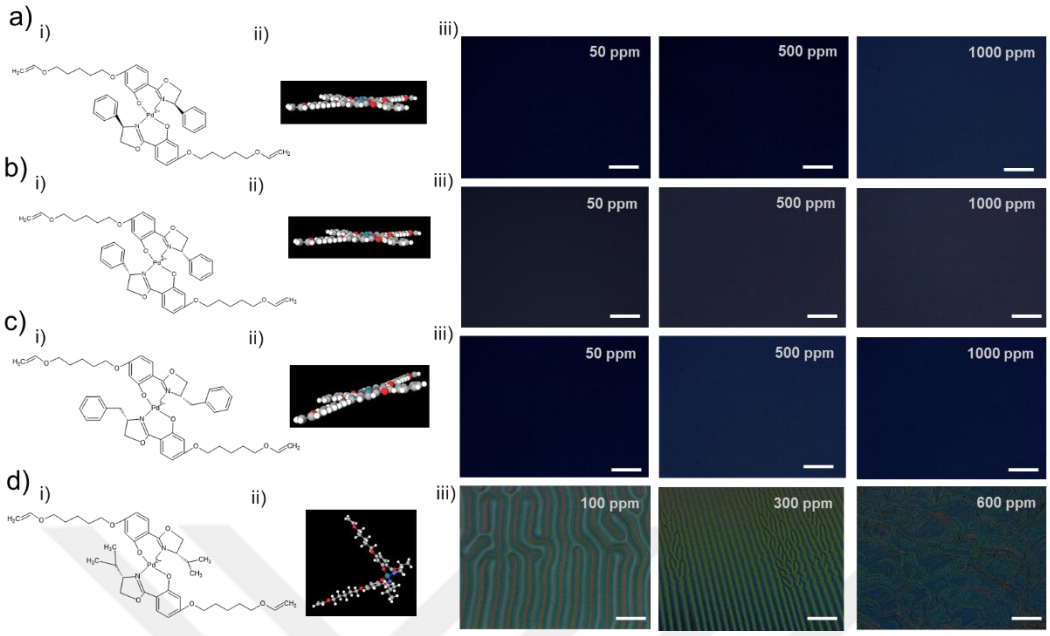


Figure 4.26 Reflection mode polarized optical microscopy images of a) Pd-3c, b) Pd-3d, c) Pd-3e, d) Pd-3f complexes (i) chemical structure, (ii) 3D chemical structure. Reflection mode polarized optical micrographs of complexes – 5CB mixtures sandwiched between DMOAP coated glasses. Scale bars: 200 μm.

Table 4.2 Helical Twisting Power (HTP) of complexes mixed with 5CB nematic LC.

| **Complex ID** | **HTP ($\mu m^{-1}$)** |
|---|---|
| Pd-3c | - |
| Pd-3d | - |
| Pd-3e | - |
| Pd-3f | 0.8 |

### 4.2.2 Polymerization of chiral reactive metallomesogens

The chiral characteristics of the complexes were investigated by optical characterizations and discussed above. At that point, we also hypothesized that the

resulting complexes can be polymerized due to reactive end groups of the structure. In order to photopolymerize the complexes, we mixed Pd-3b complex, 5CB and photoinitiator, filled between the PVA coated glass and kept under UV light. However, reactive structure cannot be polymerized due to the low amount of cross-linkable structure in the mixture and the mixture remained in the liquid phase. In order to overcome this problem, reactive LC monomer RM257 was added to the mixture and cross-linkable structure amount was increased in the mixture. A mixture of 1% photoinitiator, 10% Pd-3b, 20% RM275, 1% photoinitiator and balanced 5CB mixture was confined between PVA coated glasses was polymerized and non-reactive mesogen, 5CB, was washed with ethanol (Scheme 4.1).

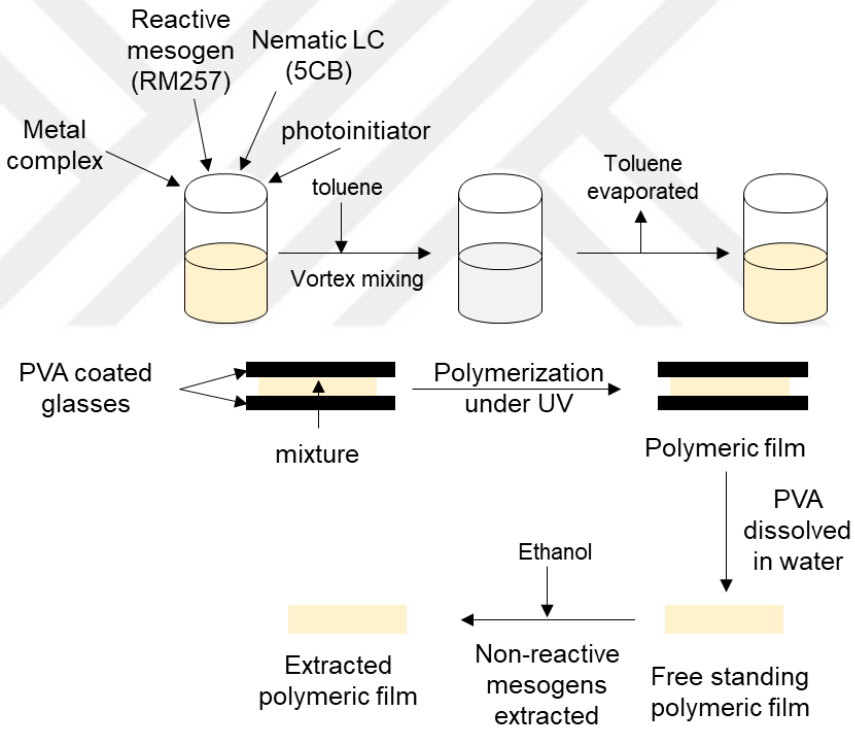


Scheme 4.1 Schematic illustration of the preparation of extracted polymeric films.

Reflection mode polarized optical microscope images of the polymeric film were collected before-after polymerization and after extraction of non-reactive mesogens (Figure 4.27.i,-iii). Moreover, UV visible spectrum of the extracted polymeric film was collected that the mixture exhibits cholesteric feature with the peak wavelength

of ~550 nm (inset of Figure 4.b.iii). With extraction of non-reactive mesogen, the pitch size of the polymeric structure decreased to UV-visible range due to shrinking which is also consistent with the blue-green appearance of the polymeric film shown in Figure 4.b.ii. This result shows that with the increase of cross-linkable compounds in the mixture, Pd-3b and RM257 remained in the structure after polymerization under UV and the extraction of non-reactive mesogen 5CB.

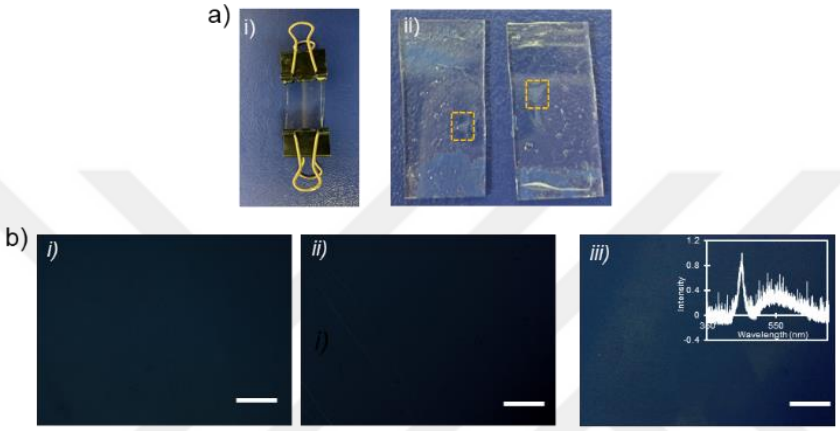


Figure 4.27 a) Photography of Pd-3b, 5CB and photoinitiator mixture confined between PVA coated glasses (i) before, (ii) after polymerization (yellow dashed rectangles show unpolymerized-fluid regions). b) Polarized optical microscopy images of films synthesized from 1 wt% photoinitiator, 10% Pd-3b, 20% RM257 and balanced 5CB filled between PVA-coated glasses a) before, b) after polymerization, c) after extraction of non-reactive mesogens (Inset shows UV-visible spectrum of extracted RM257-Pd complex polymeric film). Scale bars: 200μm.

# CHAPTER 5

# CONCLUSIONS

In the first part of the study, we reported a method which achieves significantly enhanced sensitivity of CLC-templated polymeric VOC sensors with the contribution of the strain resulted from elastic energy storage in polymeric film. We developed response curves and observed higher sensitivity of strained films as compared to flat film upon toluene exposure. In strain map of the strained films, we observed higher sensitivity in high-compressed parts as the highest strain was observed in these parts between two disclination lines. We have also conducted real time experiments and we proved that our sensor can be used several times with almost same sensitivity which gave almost 100% of the cumulative exposure and reaches 90% of equilibrium response within the first minute of exposure. Overall, this study provides a method to develop a sensor using CLC-templated polymeric films which is sensible enough to be used in industry and daily life and has durable structure for integration into wearable technologies. For this purpose, the RGB signals of these sensors can be converted into concentration using colorimetric analysis tools based on a smartphone network which ease their usage in the wearable technologies.[31,114–117] More importantly, the sensors developed in this study employed the ordering symmetries of CLCs to provide structural coloring through Bragg reflections that would not be possible with the use of their isotropic counterparts. In addition, use of CLCs as molecular templates have also provided strain to the polymer network which was critical in terms of enhancement of the sensitivity of the sensors. Herein, we also note that such enhancement is not limited to CLCs or with film geometries. Future studies may also benefit from the introduction of blue phases as molecular templates or synthesis instead of film

geometries (such as particles) that can introduce controlled strain to the polymer network.

In the second part of the study, we aimed to enhance sensor performance of CLC-templated polymeric films by development of IPN. This study differs from the previous CLC-based IPN sensors such that CLC-templated structure's selective response was also employed rather being used as optical reporter of the swelling response of penetrated polymeric structure. Our results showed that the development of IPN enhances the durability and reusability of the polymeric sensors against high VOC vapor exposures. The sensor tests performed using toluene, hexane, acetone, ethanol and water vapor demonstrated that the collaborative swelling behavior of PDMS or poly(RM257) polymeric structures upon VOC vapor critically affected sensor specificity and sensitivity which will further be used to identify the molecular constituents of the mixtures. The presented research conceptually illustrates the development of IPN and its effect on sensor performance of CLC-templated poly(RM257) polymeric structures. This study may be further extended to the development of sensors against specific target species in mixtures with the combination of different, pre-designed polymeric materials. The IPN materials we introduced herein will find use in short- or long-term tracking of the industrial or daily chemical exposures, can be integrated into wearable technologies or internet of the things, and will benefit from the machine learning algorithms for easy and more accurate quantification.

In the last part of our research, we aimed to synthesize and characterize optically active chiral metallomesogens. In the light of the studies presented in literature, the intermediate products including reactive end group were synthesized and purified by silica column chromatography which was confirmed by NMR analysis. At that point of the synthesis, the study was divided into two main task. Firstly, in order to investigate effect of metal core type on chiral behaviour of chiral reactive metallomesogens, compound 3 was synthesized by (R)- and (S)-2-amino-1-butanol and complexed with Pd, Cu and Zn acetate. Cholesteric future of Pd-3a, Pd-3b, Cu-3a and Cu-3b were confirmed by optical characterization. Moreover, HTP of these

complexes were determined as 3.9, 2.8, 1.1 and 1.2 $\mu m^{-1}$, respectively, and no significant effect of metal core type was observed on the chiral behavior of chiral reactive metallomesogens. However, Zn-3a and Zn-3b complexes did not act as chiral dopant when they are mixed with nematic LC due to unstable tetrahedral structure of Zn. As a second task, we aimed to examine effect of type of amino alcohol on chiral behavior of the chiral reactive metallomesogens and used (S)-(+)-2-phenylglycinol, (R)-(+)-2-phenylglycinol, (S)-(-)-2-amino-3-phenyl-1-propanol and (S)-(+)-2-amino-3-methyl-1-butanol amino alcohols and complexed them with palladium (II) acetate. The complexes synthesized from the amino alcohols which has phenyl in their chiral group does not exhibit chiral as no fingerprint texture was observed in the optical microscopy images of compound 5 – 5CB mixtures. Secondly, when we compared chiral feature of the Pd-3a, Pd-3b and Pd-3f complexes, we observed that increase of the chiral group chain length results in increase of pitch size and decrease of HTP due to decrease of the affinity of the molecules with nematic phase. Lastly, mixture of Pd-3a, RM257 (reactive LC monomer) and photoinitiator mixture confined between PVA coated glasses was polymerized under UV and polymerization was confirmed by optical characterization and UV-visible spectroscopy. In a study of a molecule of this structure focused on this aim, the main motivation is to determine the easily observable properties (optical, electronic, magnetic, etc.) caused by the chiral symmetry of the molecule and the possible interaction of the metal atom in this chiral symmetry with a substrate. It is an expectation that it will provide advantages in applications. In addition, the durability provided by the polymerization of these structures will provide ease of use and integration into devices. Since a molecule with the targeted structure is not available in the literature, a basis for more comprehensive and direct application studies will be established by carrying out synthesis and characterization studies in which basic information will be obtained for the applications mentioned above.

## REFERENCES


1. Dumanli, A. G. & Savin, T. Recent advances in the biomimicry of structural colours. *Chem. Soc. Rev.* **45**, 6698–6724 (2016).
2. Kinoshita, S., Yoshioka, S. & Kawagoe, K. Mechanisms of structural colour in the Morpho butterfly: Cooperation of regularity and irregularity in an iridescent scale. *Proc. R. Soc. B Biol. Sci.* **269**, 1417–1421 (2002).
3. Parnell, A. J. *et al.* Spatially modulated structural colour in bird feathers. *Sci. Rep.* **5**, 1–10 (2015).
4. Sharma, V., Crne, M., Park, J. O. & Srinivasarao, M. Structural origin of circularly polarized iridescence in jeweled beetles. *Science (80-. ).* **325**, 449–451 (2009).
5. Dong, Y. *et al.* Chameleon-inspired strain-accommodating smart skin. *ACS Nano* **13**, 9918–9926 (2019).
6. Teyssier, J., Saenko, S. V., Van Der Marel, D. & Milinkovitch, M. C. Photonic crystals cause active colour change in chameleons. *Nat. Commun.* **6**, 1–7 (2015).
7. Binet, C., Mitov, M. & Boudet, A. Bragg reflections in cholesteric liquid crystals: from selectivity to broadening and reciprocally. *Mol. Cryst. Liq. Cryst. Sci. Technol. Sect. A Mol. Cryst. Liq. Cryst.* **339**, 111–123 (2000).
8. Sun, J., Bhushan, B. & Tong, J. Structural coloration in nature. *RSC Adv.* **3**, 14862–14889 (2013).
9. Mirzaei, A., Leonardi, S. G. & Neri, G. Detection of hazardous volatile organic compounds (VOCs) by metal oxide nanostructures-based gas sensors: A review. *Ceram. Int.* **42**, 15119–15141 (2016).
10. Occupational Safety and Health Administration. Occupational Exposure Limits-Toluene. *United States Department of Labor* (2017). Available at: https://www.osha.gov/SLTC/toluene/exposure_limits.html. (Accessed: 20th March 2018)

11. Nayani, K. *et al.* Liquid crystals with interfacial ordering that enhances responsiveness to chemical targets. *Adv. Mater.* **30**, 1–7 (2018).

12. Bedolla Pantoja, M. A. & Abbott, N. L. Surface-Controlled Orientational Transitions in Elastically Strained Films of Liquid Crystal That Are Triggered by Vapors of Toluene. *ACS Appl. Mater. Interfaces* **8**, 13114–13122 (2016).

13. Bukusoglu, E., Bedolla Pantoja, M., Mushenheim, P. C., Wang, X. & Abbott, N. L. Design of Responsive and Active (Soft) Materials Using Liquid Crystals. *Annu. Rev. Chem. Biomol. Eng.* **7**, 163–196 (2016).

14. Mulder, D. J., Schenning, A. P. H. J. & Bastiaansen, C. W. M. Chiral-nematic liquid crystals as one dimensional photonic materials in optical sensors. *J. Mater. Chem. C* **2**, 6695–6705 (2014).

15. Raynes, E. P. & Jia, X. The measurement of weak chirality using nematic liquid crystals. *Liq. Cryst.* **44**, 1960–1967 (2017).

16. Popov, P., Honaker, L. W., Mirheydari, M., Mann, E. K. & Jákli, A. Chiral nematic liquid crystal microlenses. *Sci. Rep.* **7**, 1–9 (2017).

17. Belmonte, A., Bus, T., Broer, D. J. & Schenning, A. P. H. J. Patterned full-color reflective coatings based on photonic cholesteric liquid-crystalline particles. *ACS Appl. Mater. Interfaces* **11**, 14376–14382 (2019).

18. Debije, M. G. & Schenning, A. P. H. J. Stimuli-Responsive Liquid Crystalline Materials. in *Stimuli-Responsive Liquid Crystalline Materials* 1–9 (Elsevier Ltd., 2016). doi:10.1016/b978-0-12-803581-8.04039-x

19. Herzer, N. *et al.* Printable optical sensors based on H-bonded supramolecular cholesteric liquid crystal networks. *J. Am. Chem. Soc.* **134**, 7608–7611 (2012).

20. Winterbottom, D. A., Narayanaswamy, R. & Jr, I. M. R. Cholesteric liquid crystals for detection of organic vapours. *Sens. Actuators, B* **90**, 52–57 (2003).

21. Stumpel, J. E. *et al.* An optical sensor for volatile amines based on an inkjet-printed, hydrogen-bonded, cholesteric liquid crystalline film. *Adv. Opt. Mater.* **2**, 459–464 (2014).

22. Mujahid, A., Stathopulos, H., Lieberzeit, P. A. & Dickert, F. L. Solvent vapour detection with cholesteric liquid crystals—optical and mass-sensitive evaluation of the sensor mechanism. *Sensors* **10**, 4887–4897 (2010).

23. Han, Y., Pacheco, K., Bastiaansen, C. W. M., Broer, D. J. & Sijbesma, R. P. Optical monitoring of gases with cholesteric liquid crystals. *J. Am. Chem. Soc.* **132**, 2961–2967 (2010).

24. Chang, C. K., Bastiaansen, C. W. M., Broer, D. J. & Kuo, H. L. Discrimination of alcohol molecules using hydrogen-bridged cholesteric polymer networks. *Macromolecules* **45**, 4550–4555 (2012).

25. Chang, C. K., Kuo, H. L., Tang, K. T. & Chiu, S. W. Optical detection of organic vapors using cholesteric liquid crystals. *Appl. Phys. Lett.* **99**, 10–13 (2011).

26. Sutarlie, L., Lim, J. Y. & Yang, K. L. Cholesteric liquid crystals doped with dodecylamine for detecting aldehyde vapors. *Anal. Chem.* **83**, 5253–5258 (2011).

27. Sutarlie, L., Qin, H. & Yang, K. L. Polymer stabilized cholesteric liquid crystal arrays for detecting vaporous amines. *Analyst* **135**, 1691–1696 (2010).

28. Kek, K. J., Lee, J. J. Z., Otono, Y. & Ishihara, S. Chemical gas sensors using chiral nematic liquid crystals and its applications. *J. Soc. Inf. Disp.* **25**, 366–373 (2017).

29. Wang, T., Liu, M. & Hwang, S. Optical sensing of organic vapour based on polymer cholesteric liquid crystal film. *Liq. Cryst.* 1–8 (2020).

30. Bukusoglu, E., Pantoja, M. B., Mushenheim, P. C., Wang, X. & Abbott, N. L. Design of Responsive and Active (Soft) Materials Using Liquid Crystals. *Annu. Rev. Chem. Biomol. Eng.* **7**, 163–196 (2016).

31. Kou, D., Zhang, Y., Zhang, S., Wu, S. & Ma, W. High-sensitive and stable photonic crystal sensors for visual detection and discrimination of volatile aromatic hydrocarbon vapors. *Chem. Eng. J.* **375**, 121987 (2019).

32. Yang, K., Cadwell, K. & Abbott, N. L. Mechanistic Study of the Anchoring Behavior of Liquid Crystals Supported on Metal Salts and Their Orientational Responses to Dimethyl Methylphosphonate. *J. Phys. Chem. B* **108**, 20180–20186 (2004).

33. He, F. J., Liu, H. L., Chen, L. C. & Xiong, X. L. A portable liquid crystal-based polarized light system for the detection of organophosphorus nerve gas. *Rev. Sci. Instrum.* **89**, 035001 (2018).

34. Ahmadnia-Feyzabad, S., Khodadadi, A. A., Vesali-Naseh, M. & Mortazavi, Y. Highly sensitive and selective sensors to volatile organic compounds using MWCNTs/SnO 2. *Sens. Actuators, B* **166**–**167**, 150–155 (2012).

35. Suematsu, K. *et al.* Nanoparticle cluster gas sensor: Controlled clustering of SnO2 nanoparticles for highly sensitive toluene detection. *ACS Appl. Mater. Interfaces* **6**, 5319–5326 (2014).

36. Vijaya, J. J., Kennedy, L. J., Sekaran, G. & Nagaraja, K. S. Sol-gel derived (Sr,Ni)Al2O4 composites for benzene and toluene sensors. *Mater. Lett.* **61**, 5213–5216 (2007).

37. Tang, W. & Wang, J. Mechanism for toluene detection of flower-like ZnO sensors prepared by hydrothermal approach: Charge transfer. *Sens. Actuators, B* **207**, 66–73 (2015).

38. Matsuguchi, M., Uno, T., Aoki, T. & Yoshida, M. Chemically modified copolymer coatings for mass-sensitive toluene vapor sensors. *Sens. Actuators, B* **131**, 652–659 (2008).

39. Khan, S., Newport, D. & Le Calvé, S. Development of a Toluene detector based on deep UV absorption spectrophotometry using glass and aluminum capillary Tube Gas Cells with a LED source. *Micromachines* **10**, 193 (2019).

40. Xiao, Y. *et al.* Reduced graphene oxide for fiber-optic toluene gas sensing. *Opt. Express* **24**, 28290 (2016).

41. Fujii, Y., Honma, S., Morisawa, M. & Muto, S. Development of new optical

fiber toluene sensor. *Adv. Mater. Devices Sens. Imaging III* **6829**, 68291Z (2007).

42. Chang, H., Chang, G. T., Thokchom, A. K., Kim, T. & Park, J. Ultra-fast responsive colloidal – polymer composite-based volatile organic compounds ( VOC ) sensor using nanoscale easy tear process. *Sci. Rep.* **8**, 1–11 (2018).

43. Jiang, X. *et al.* Highly-sensitive optical organic vapor sensor through polymeric swelling induced variation of fluorescent intensity. *Nat. Commun.* **9**, 1–9 (2018).

44. Athanasekos, L., Pispas, S. & Riziotis, C. Novel block copolymers for multi-agent detection using polymer optical fibers. *Microstruct. Spec. Opt. Fibres* **8426**, 842615 (2012).

45. Acikbas, Y. *et al.* An optical vapor sensor based on amphiphilic block copolymer langmuir-blodgett films. *IEEE Sens. J.* **18**, 5313–5320 (2018).

46. Hromadka, J. *et al.* Volatile Organic Compounds Sensing Using Optical Fibre Long Period Grating with Mesoporous Nano-Scale Coating. *Sensors* **17**, 205 (2017).

47. He, C., Korposh, S., Correia, R. & Morgan, S. P. Volatile Organic Compound Vapour Measurements Using a Localised Surface Plasmon Resonance Optical Fibre Sensor Decorated with a Metal-Organic Framework. *Sensors* **21**, 1420 (2021).

48. Dolai, S. *et al.* Colorimetric Polydiacetylene − Aerogel Detector for Volatile Organic Compounds (VOCs). *Appl. Mater. Interfaces* **9**, 2891–2898 (2017).

49. Avşar, D. I. & Bukusoglu, E. Chameleon skin-inspired polymeric particles for the detection of toluene vapor. *Soft Matter* **16**, 8683–8691 (2020).

50. Mykytyuk, Z. M., Kremer, I. P., Ivakh, M., Diskovskyi, I. S. & Khomyak, S. V. Optical sensor with liquid crystal sensitive element for monitoring acetone vapor during exhalation. *Mol. Cryst. Liq. Cryst.* **721**, 24–29 (2021).

51. Batir, O., Bat, E. & Bukusoglu, E. Strain-enhanced Sensitivity of Polymeric

Sensors Templated from Cholesteric Liquid Crystals. *Soft Matter* **16**, 6794–6802 (2020).

52. Akdeniz, B. Liquid Crystal - Templated Synthesis of Polymeric Microparticles with Complex Nanostructres. (Middle East Technical University, 2019).

53. Lecommandoux, S. *et al.* Backbone conformation study on 'side-on fixed' liquid crystal polymers. *Phys. B Condens. Matter* **234**–**236**, 250–251 (1997).

54. Avşar, D. I. & Bukusoglu, E. Chameleon skin-inspired polymeric particles for the detection of toluene vapor. *Soft Matter* **16**, 8683–8691 (2020).

55. Yeh, T. Y., Liu, M. F., Lin, R. De & Hwang, S. J. Alcohol Selective Optical Sensor Based on Porous Cholesteric Liquid Crystal Polymer Networks. *Molecules* **27**, (2022).

56. Lohani, A., Singh, G., Bhattacharya, S. S. & Verma, A. Interpenetrating Polymer Networks as Innovative Drug Delivery Systems. *J. Drug Deliv.* **2014**, 1–11 (2014).

57. Chikh, L., Delhorbe, V. & Fichet, O. (Semi-)Interpenetrating polymer networks as fuel cell membranes. *J. Memb. Sci.* **368**, 1–17 (2011).

58. Matricardi, P., Di Meo, C., Coviello, T., Hennink, W. E. & Alhaique, F. Interpenetrating polymer networks polysaccharide hydrogels for drug delivery and tissue engineering. *Adv. Drug Deliv. Rev.* **65**, 1172–1187 (2013).

59. Gan, Y. *et al.* An interpenetrating network-strengthened and toughened hydrogel that supports cell-based nucleus pulposus regeneration. *Biomaterials* **136**, 12–28 (2017).

60. Chen, Z. *et al.* Nitrogen-doped interpenetrating porous carbon/graphene networks for supercapacitor applications. *Chem. Eng. J.* **409**, 127891 (2021).

61. Bao, Z. *et al.* Three-Dimensional Interpenetrating Network Phase-Change Composites with High Photothermal Conversion and Rapid Heat Storage and Release. *ACS Appl. Energy Mater.* **4**, 7710–7720 (2021).

62. Li, H. Q. *et al.* Proton exchange membranes with cross-linked interpenetrating network of sulfonated polyvinyl alcohol and poly(2-acrylamido-2-methyl-1-propanesulfonic acid): Excellent relative selectivity. *J. Memb. Sci.* **595**, 117511 (2020).

63. Liu, H. *et al.* High-effective preparation of 3D hierarchical nanoporous interpenetrating network structure carbon membranes as flexible free-standing anodes for stable lithium and sodium storage. *Colloids Surfaces A Physicochem. Eng. Asp.* **608**, 125593 (2021).

64. Sun, T. *et al.* Nanofibers interpenetrating network mimicking "reinforced-concrete" to construct mechanically robust composite membrane for enhanced CO2 separation. *J. Memb. Sci.* **639**, 119749 (2021).

65. Bai, L., Liu, J., Jin, C., Zhang, J. & Wang, F. Heteroatom-doped carbon interpenetrating networks: a signpost to achieve the best performance of non-PGM catalysts for fuel cells. *J. Mater. Chem. A* **8**, 18767–18777 (2020).

66. Hoekstra, D. C. *et al.* Wavelength-Selective Photopolymerization of Hybrid Acrylate-Oxetane Liquid Crystals. *Angew. Chemie* **133**, 2–9 (2021).

67. Hussain, S. & Park, S. Y. Optical glucose biosensor based on photonic interpenetrating polymer network with solid-state cholesteric liquid crystal and cationic polyelectrolyte. *Sensors Actuators, B Chem.* **316**, 128099 (2020).

68. Hussain, S. & Park, S. Y. Sweat-Based Noninvasive Skin-Patchable Urea Biosensors with Photonic Interpenetrating Polymer Network Films Integrated into PDMS Chips. *ACS Sensors* **5**, 3988–3998 (2020).

69. Noh, K. G. & Park, S. Y. Biosensor Array of Interpenetrating Polymer Network with Photonic Film Templated from Reactive Cholesteric Liquid Crystal and Enzyme-Immobilized Hydrogel Polymer. *Adv. Funct. Mater.* **28**, 1–9 (2018).

70. Shin, S. R. *et al.* Synthesis and characteristics of semi-interpenetrating polymer network hydrogels of chitosan and polyaniline. *Smart Struct. Mater.*

*2004 Electroact. Polym. Actuators Devices* **5385**, 490 (2004).

71. Zhao, Y., Kang, J. & Tan, T. Salt-, pH- and temperature-responsive semi-interpenetrating polymer network hydrogel based on poly(aspartic acid) and poly(acrylic acid). *Polymer (Guildf).* **47**, 7702–7710 (2006).

72. Pramanik, S., Dutta, J. & Chakraborty, P. Development of pH-responsive interpenetrating polymer networks of polyacrylamide-g-gum arabica and sodium alginate for gastroprotective delivery of gabapentin. *Indian J. Pharm. Sci.* **83**, 473–482 (2021).

73. Liu, X., Guo, H. & Zha, L. Study of pH/temperature dual stimuli-responsive nanogels with interpenetrating polymer network structure. *Polym. Int.* **61**, 1144–1150 (2012).

74. Moirangthem, M., Engels, T. A. P., Murphy, J., Bastiaansen, C. W. M. & Schenning, A. P. H. J. Photonic Shape Memory Polymer with Stable Multiple Colors. *ACS Appl. Mater. Interfaces* **9**, 32161–32167 (2017).

75. Li, Y., Chen, Y., Zhang, C., Xue, T. & Yang, M. A humidity sensor based on interpenetrating polymer network prepared from poly(dimethylaminoethyl methacrylate) and poly(glycidyl methacrylate). *Sensors Actuators B Chem.* **125**, 131–137 (2007).

76. Zhang, L. *et al.* Preparation and properties of water-responsive films with color controllable based on liquid crystal and poly(ethylene glycol) interpenetrating polymer network. *Liq. Cryst.* 1–9 (2022). doi:10.1080/02678292.2022.2037769

77. Shi, X. *et al.* Wearable Optical Sensing of Strain and Humidity : A Patterned Dual-Responsive Semi-Interpenetrating Network of a Cholesteric Main-Chain Polymer and a Poly ( ampholyte ). *Adv. Funct. Mater.* **31**, 2104641 (2021).

78. Myung, D., Hussain, S. & Park, S.-Y. Photonic calcium and humidity array sensor prepared with reactive cholesteric liquid crystal mesogens. *Sensors*

*Actuators, B Chem.* **298**, 126894 (2019).

79. Kragt, A. J. J., Zuurbier, N. C. M., Broer, D. J. & Schenning, A. P. H. J. Temperature-Responsive, Multicolor-Changing Photonic Polymers. *ACS Appl. Mater. Interfaces* **11**, 28172–28179 (2019).

80. Lim, J. S., Kim, Y. J. & Park, S. Y. Functional solid-state photonic droplets with interpenetrating polymer network and their applications to biosensors. *Sensors Actuators, B Chem.* **329**, 129165 (2021).

81. Stumpel, J. E. *et al.* Stimuli-responsive materials based on interpenetrating polymer liquid crystal hydrogels. *Adv. Funct. Mater.* **25**, 3314–3320 (2015).

82. Kang, S.-W., Sprunt, S. & Chien, L.-C. Ordered Polymer Microstructures Obtained Using Pattern Forming States of a Cholesteric Liquid Crystal as Templates. *Adv. Mater.* **13**, 1179–1182 (2001).

83. Kim, M., Huang, Y., Choi, K. & Hidrovo, C. H. The improved resistance of PDMS to pressure-induced deformation and chemical solvent swelling for microfluidic devices. *Microelectron. Eng.* **124**, 66–75 (2014).

84. Lee, J. N., Park, C. & Whitesides, G. M. Solvent Compatibility of Poly(dimethylsiloxane)-Based Microfluidic Devices. *Anal. Chem.* **75**, 6544–6554 (2003).

85. Venkatesan, K., Kouwer, P. H. J., Yagi, S., Müller, P. & Swager, T. M. Columnar mesophases from half-discoid platinum cyclometalated metallomesogens. *J. Mater. Chem.* **18**, 400–407 (2008).

86. Wu, X., Zhu, M., Bruce, D. W., Zhu, W. & Wang, Y. An overview of phosphorescent metallomesogens based on platinum and iridium. *J. Mater. Chem. C* **6**, 9848–9860 (2018).

87. Cuerva, C., Campo, J. A., Cano, M. & Schmidt, R. Nanostructured discotic Pd(ii) metallomesogens as one-dimensional proton conductors. *Dalt. Trans.* **46**, 96–105 (2017).

88. Liu, C. Y., Hu, C. C., Chen, J. L. & Liu, K. T. Metallomesogens as stationary

phases for the separation of phenols by gas chromatography. *Anal. Chim. Acta* **384**, 51–62 (1999).

89. Chen, J. L. & Liu, C. Y. Separation of dialkyl sulfides by metallomesogenic stationary phases for complexation gas chromatography. *J. Chromatogr. A* **1161**, 269–274 (2007).

90. Huang, K. P., Misra, T. K., Wang, G. R., Huang, B. Y. & Liu, C. Y. Novel stationary phase for complexation gas chromatography originating from ionic liquid and metallomesogen. *J. Chromatogr. A* **1215**, 177–184 (2008).

91. Bryks, W., Smith, S. C. & Tao, A. R. Metallomesogen Templates for Shape Control of Metal Selenide Nanocrystals. *Chem. Mater.* **29**, 3653–3662 (2017).

92. Crispini, A., Ghedini, M. & Pucci, D. Functional properties of metallomesogens modulated by molecular and supramolecular exotic arrangements. *Beilstein J. Org. Chem.* **5**, 23–25 (2009).

93. Pucci, D. *et al.* Liquid crystalline cholesterol-based ortho-palladated curcumin complexes as multifunctional biomaterials. *Mol. Cryst. Liq. Cryst.* **481**, 14–25 (2008).

94. Chico, R., Domínguez, C., Donnio, B., Coco, S. & Espinet, P. Liquid crystalline salen manganese(III) complexes. Mesomorphic and catalytic behaviour. *Dalt. Trans.* **40**, 5977–5983 (2011).

95. Akabane, T., Ohta, K., Takizawa, T., Matsuse, T. & Kimura, M. Discotic liquid crystals of transition metal complexes, 54: Rapid microwave-assisted synthesis and homeotropic alignment of phthalocyanine-based liquid crystals. *J. Porphyr. Phthalocyanines* **21**, 476–492 (2017).

96. Qian, G. *et al.* Chiral Platinum-Based Metallomesogens with Highly Efficient Circularly Polarized Electroluminescence in Solution-Processed Organic Light-Emitting Diodes. *Adv. Opt. Mater.* **2000775**, 1–8 (2020).

97. Wang, Y. *et al.* Influence of integrated alkyl-chain length on the mesogenic and photophysical properties of platinum-based metallomesogens and their

application for polarized white OLEDs. *Dye. Pigment.* **133**, 238–247 (2016).

98. Yang, X. *et al.* Platinum-based metallomesogens bearing a Pt(4,6-dfppy)(acac) skeleton: Synthesis, photophysical properties and polarised phosphorescence application. *Dalt. Trans.* **47**, 13368–13377 (2018).

99. Oriol, L. & Serrano, J. L. Metal-containing nanostructured materials through in situ polymerization of reactive metallomesogens. *Angew. Chemie - Int. Ed.* **44**, 6618–6621 (2005).

100. Cano, M., Oriol, L., Pin, M. & Serrano, J. L. Photopolymerization of Reactive Mesogenic Schiff Bases and Related Metallomesogens. *Chem. Mater.* **11**, 94–100 (1999).

101. Martin, A. G., Harms, S., Weigand, W. & Gin, D. L. Polymerizable transition-metal-containing liquid crystals with thermally reactive 1,3-diene tails. *Adv. Mater.* **17**, 602–606 (2005).

102. Lehmann, M., Sierra, T., Barbera, J., Serrano, L. & Parker, R. Chiral hexacatenar metallomesogens : supramolecular organization versus steric demand of chiral cores. *J. Mater. Chem.* **12**, 1342–1350 (2002).

103. Karausta, A. & Bukusoglu, E. Liquid crystal-templated synthesis of mesoporous membranes with predetermined pore alignment. *ACS Appl. Mater. Interfaces* **10**, 33484–33492 (2018).

104. Watanabe, W. H. & Conlon, L. E. Homogeneous Metal Salt Catalysis in Organic Reactions. I. The Preparation of Vinyl Ethers by Vinyl Transetherification. *J. Am. Chem. Soc.* **79**, 2828–2833 (1957).

105. Serrano, J. L. *et al.* Improving FLC Properties. Simplicity, Planarity, and Rigidity in New Chiral Oxazoline Derivatives. *J. Am. Chem. Soc.* **117**, 8312–8321 (1995).

106. Feldman, A. I., Crooker, P. P., Goh, L. M. Chiral strain and reentrancy in blue-phase transitions A. *Phys. Rev. A* **35**, 842–846 (1987).

107. Bukusoglu, E. *et al.* Strain-induced alignment and phase behavior of blue

phase liquid crystals confined to thin films. *Soft Matter* **13**, 8999–9006 (2017).

108. Smalyukh, I. I. & Lavrentovich, O. D. Three-dimensional director structures of defects in Grandjean-Cano wedges of cholesteric liquid crystals studied by fluorescence confocal polarizing microscopy. *Phys. Rev. E - Stat. Physics, Plasmas, Fluids, Relat. Interdiscip. Top.* **66**, 16 (2002).

109. Madsen, M. H., Agentoft, N., Hansen, P. & Garnaes, J. Accounting for PDMS Shrinkage when Replicating Structures. *J. Micromechanics Microengineering* **24**, 127002 (2014).

110. Johnson, L. M. *et al.* Elastomeric microparticles for acoustic mediated bioseparations. 1–8 (2013).

111. Watanabe, K. & Akagi, K. Helically assembled π-conjugated polymers with circularly polarized luminescence. *Sci. Technol. Adv. Mater.* **15**, (2014).

112. Golicha, H. S. A., Omarn, M. H. & Mbithi, N. M. Optical Techniques in the Determination of Pitch Lengths in the Cholesteric and Chiral Smectic C Phases. *J. Mater. Sci. Eng.* **10**, 1–5 (2021).

113. Endo, K., Liu, Y., Ube, H., Nagata, K. & Shionoya, M. Asymmetric construction of tetrahedral chiral zinc with high configurational stability and catalytic activity. *Nat. Commun.* **11**, 1–7 (2020).

114. Mccracken, K. E. & Yoon, J. Analytical Methods Recent approaches for optical smartphone sensing in resource-limited settings : a brief review. *Anal. Methods* **8**, 6591–6601 (2016).

115. Shen, L., Hagen, A. & Papautsky, I. Point-of-care colorimetric detection with a smartphone. *Lab Chip* **12**, 4240–4243 (2012).

116. Meier, R. J. *et al.* Simultaneous Photographing of Oxygen and pH In Vivo Using Sensor Films **. *Angew. Chemie Int. Ed.* **50**, 10893–10896 (2011).

117. Xu, W. *et al.* Sensors and Actuators B : Chemical Simultaneous color sensing of O 2 and pH using a smartphone. *Sensors Actuators B. Chem.* **220**, 326–330 (2015).

# APPENDICES

## A. Calculation of strain introduced by wedge cell

We first calculated the change of the film thickness (Δh) starting from equating the thickness of the film at disclination line and found as;

$$\Delta h_i = \frac{p}{2} \times \left[\frac{m_i}{m_{i+1}+m_i}\right] \quad \text{Equation A. 1}$$

where an integral number m of half pitches of length p/2 be fitted into sample thickness h[106].

Then, we calculated radius of disclination line ($r_d$) using a model based on elastic energy proposed by Feldman et al[106]. In this model, only twist part of elastic energy was used and the location of disclination lines were calculated as;

$$r_d = \sqrt{2R \times \left(m \times \frac{p}{2} + \Delta h\right)} \quad \text{Equation A. 2}$$

where R is the radius of curvature of PCX lens.

We also calculated amount of strain introduced to the CLC film in a wedge cell before polymerization for compressed and stretched parts in the two sides of disclination line, as;

$$strain = -\frac{\Delta h}{m \times \frac{p}{2}} \quad for\ compressed\ part \quad \text{Equation A. 3}$$

$$strain = \frac{\Delta h}{m \times \frac{p}{2}} \quad for\ stretched\ part \quad \text{Equation A. 4}$$

***Calculation of strain by extraction***

Strain values we calculated using Eqn. S3 and S4 was for CLC film in wedge cell before polymerization. However, as we used extracted films in our sensor tests, we needed to calculate the amount of strain introduced via extraction.

We recorded UV-visible spectra of the films with 5-25% chiral dopant and showed peak wavelengths at the reflected light in Figure 4.2.a. We observed that the peak wavelength and chiral dopant ratio have a linear relationship. Moreover, at low chiral concentrations, no wavelength peak was observed in the visible region before polymerization. Therefore, in order to calculate the shrinkage via extraction, we extrapolated the before polymerization data and estimated the wavelength peak of CLCs at low chiral concentrations before polymerization. At 7.5% chiral dopant concentration, we observed 45% of wavelength shift which can be considered as the strain in compression mode introduced via extraction; therefore, all the regions became compressed. By considering the strain introduced via both extraction and wedge cell, we re-calculated the strain values and mentioned the parts of the film as high-compressed, medium-compressed and low-compressed in the main text.

## B. Sensor test of strained films

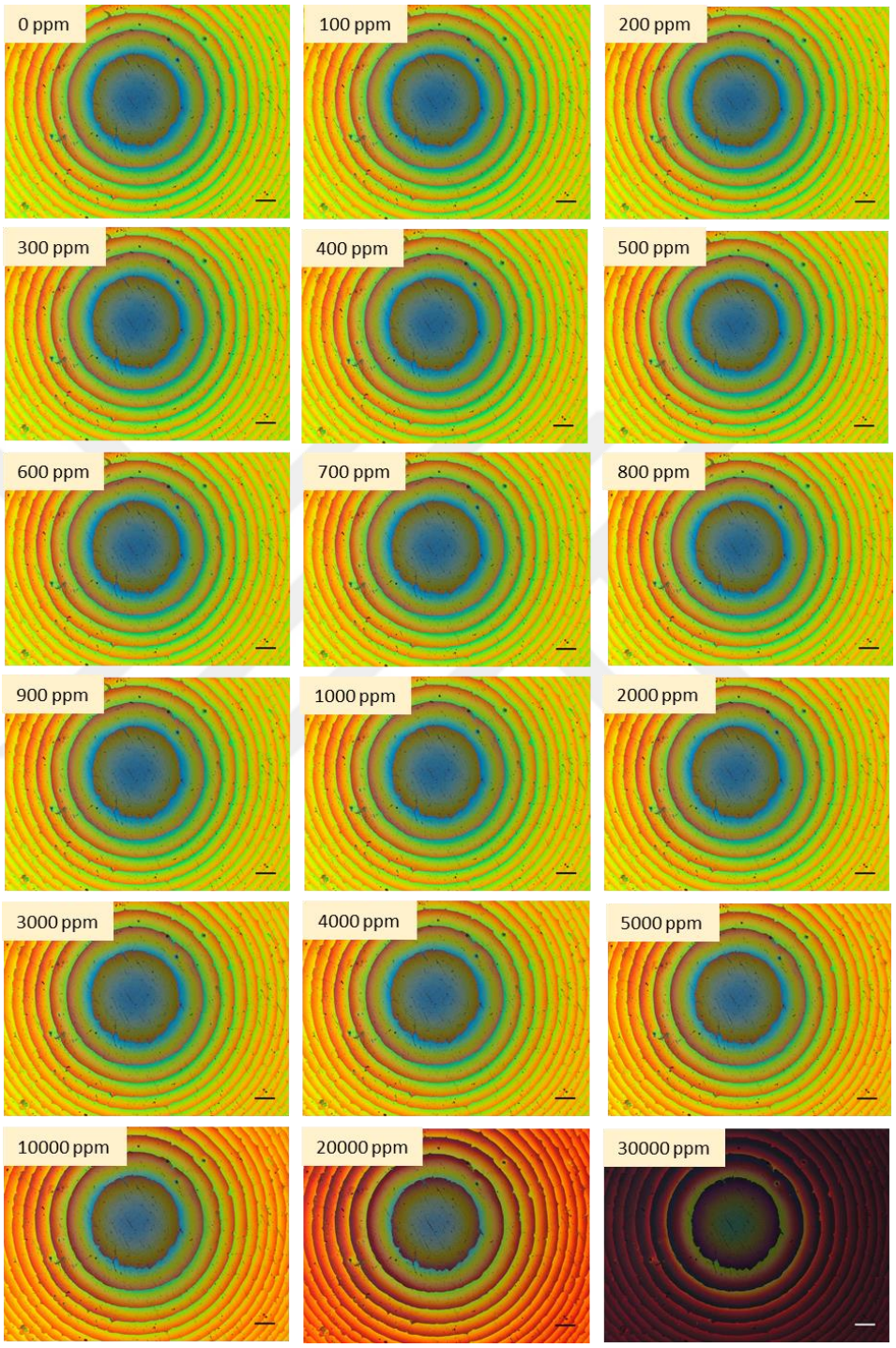


Appendix B. 1 Reflection mode polarized optical micrographs of CLC-templated polymeric strained films synthesized from 20% RM257, 7.5% chiral dopant and balance E7 collected upon toluene exposure. (scale bar: 200μm)

## C. Chemical structures of aminoalcohols

**aa1 :** R -2-amino-1-butanol

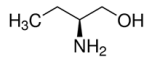


**aa2 :** S -2-amino-1-butanol

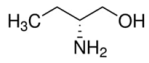


**aa3 :** (R)-(+)-2-phenylglycinol

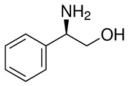


**aa4 :** (S)-(+)-2-phenylglycinol

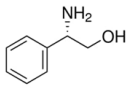


**aa5:** (S)-2-amino-3-phenyl-1-propanol

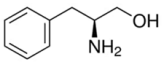


**aa6 :** (S)-(+)-2-amino-3-methyl-1-butanol

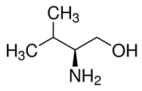


Appendix C. 1 Chemical structures of aminoalcohols

## D. $^{1}$H NMR spectrum of synthesized compounds

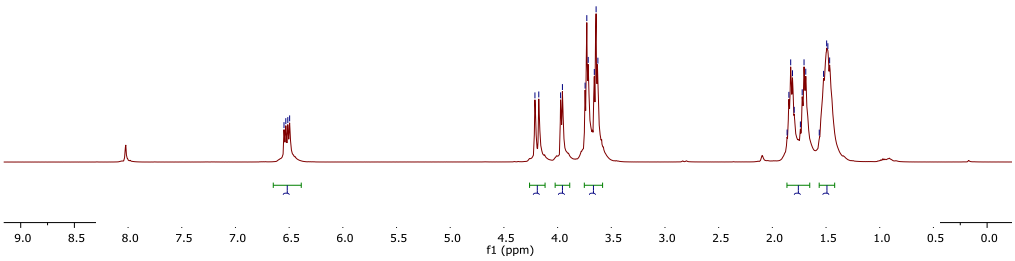


Appendix D.1 The H-NMR spectrum of (6-Chlorohexyloxy)ethane.

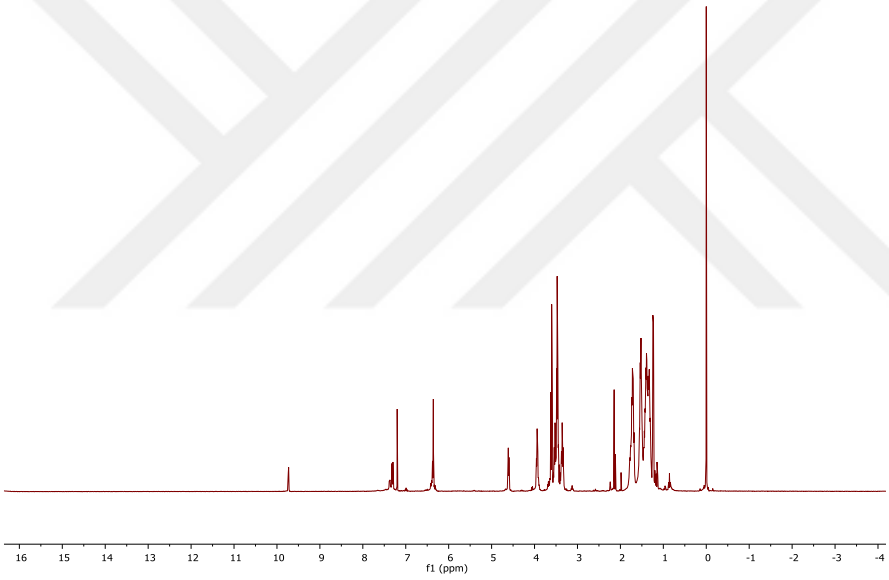


Appendix D.2 The H-NMR spectrum of 4-(6-hydroxyhexyloxy)-2-hydroxybenzonitrile.

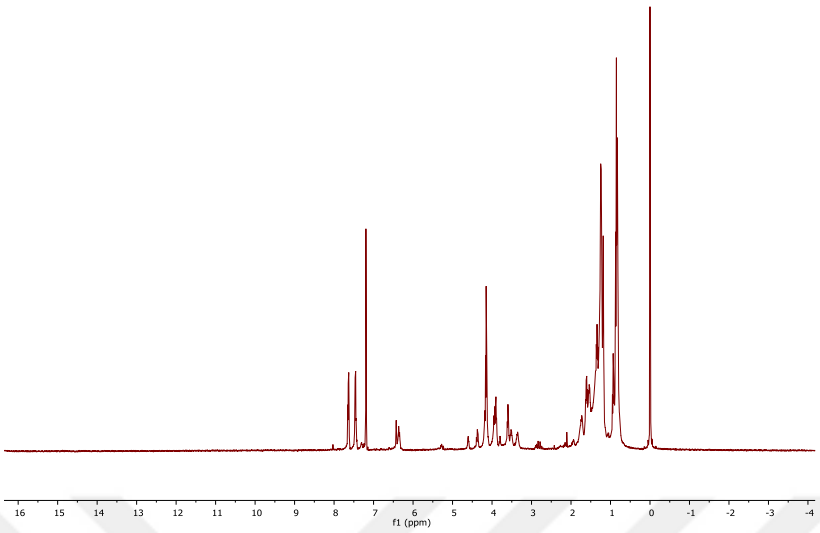


Appendix D.3 The H-NMR spectrum of synthesis of (4S)-4,5-dihydro-2-(2'-hydroxy,4-(6-hydroxyhexyloxy)-phenyl)-4-[(R)-2-amino-1-butanol]oxazole.

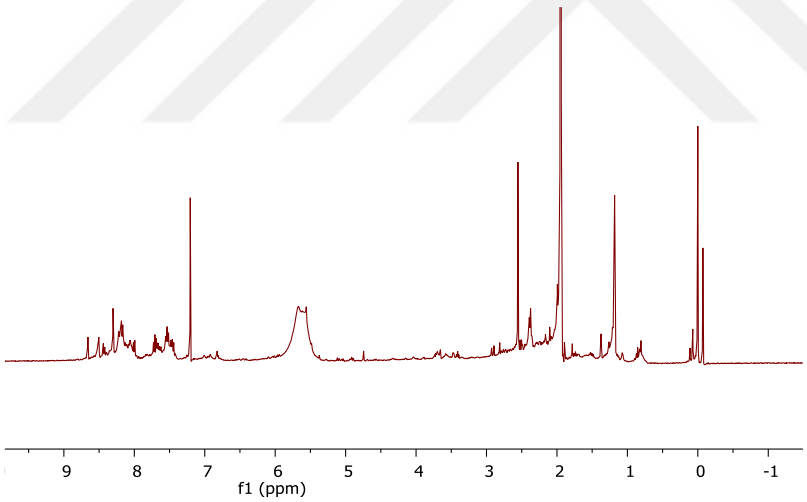


Appendix D.4 The $^{1}$H-NMR spectrum of 3a-*Pd* complex

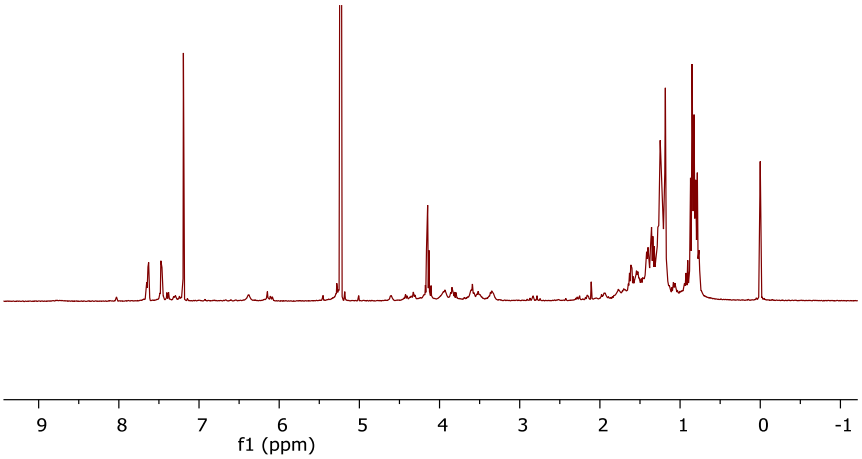


Appendix D. 5 The H-NMR spectrum of Pd-3b complex

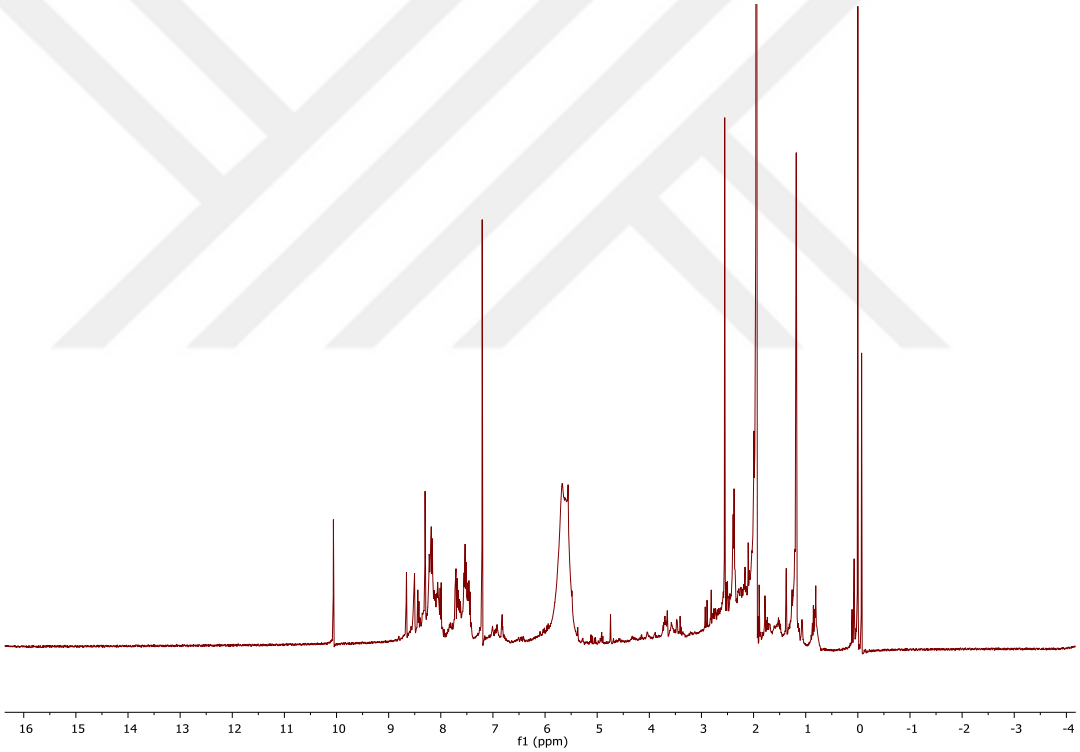


Appendix D. 6 The H-NMR spectrum of Zn-3a complex.

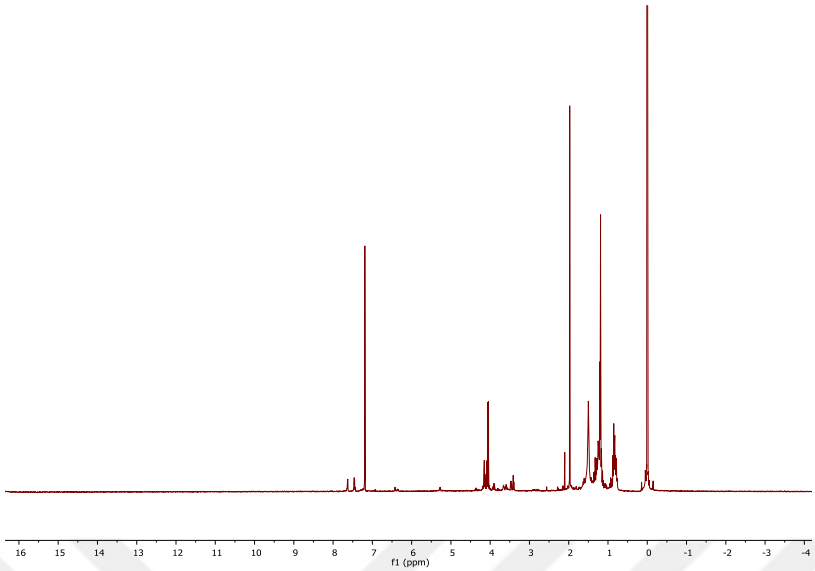


Appendix D. 7 The H-NMR spectrum of Zn-3b complex.

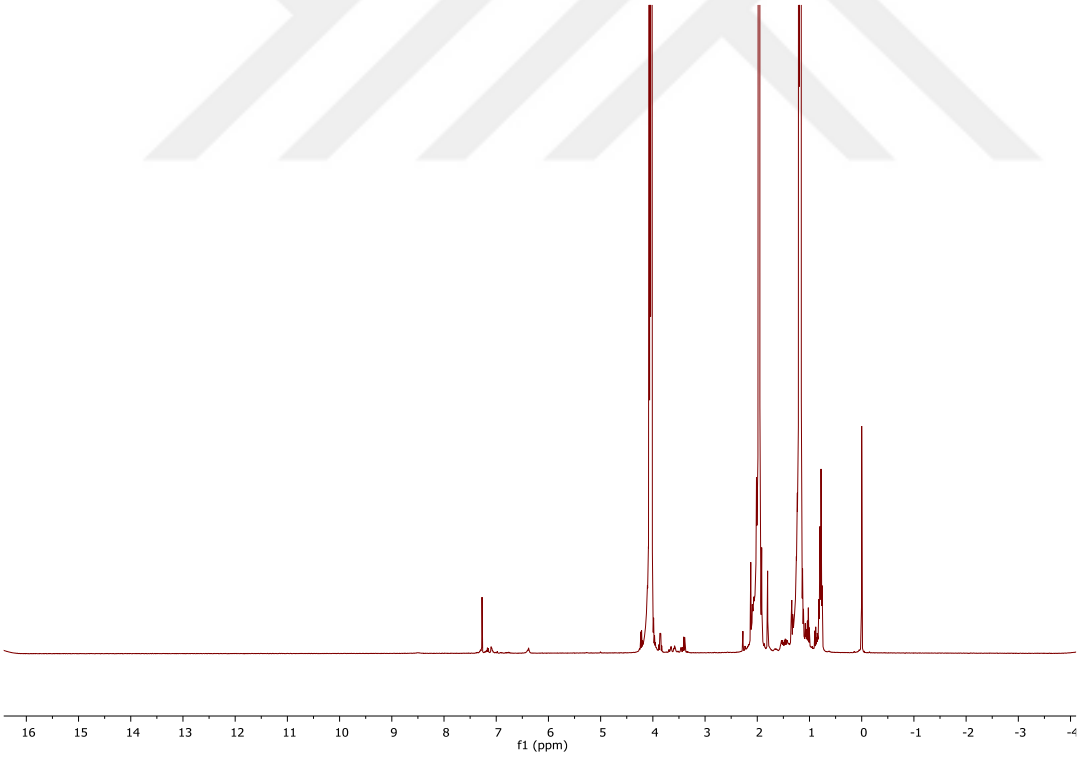


Appendix D. 8 The $^{1}$H-NMR spectrum of 3c compound.

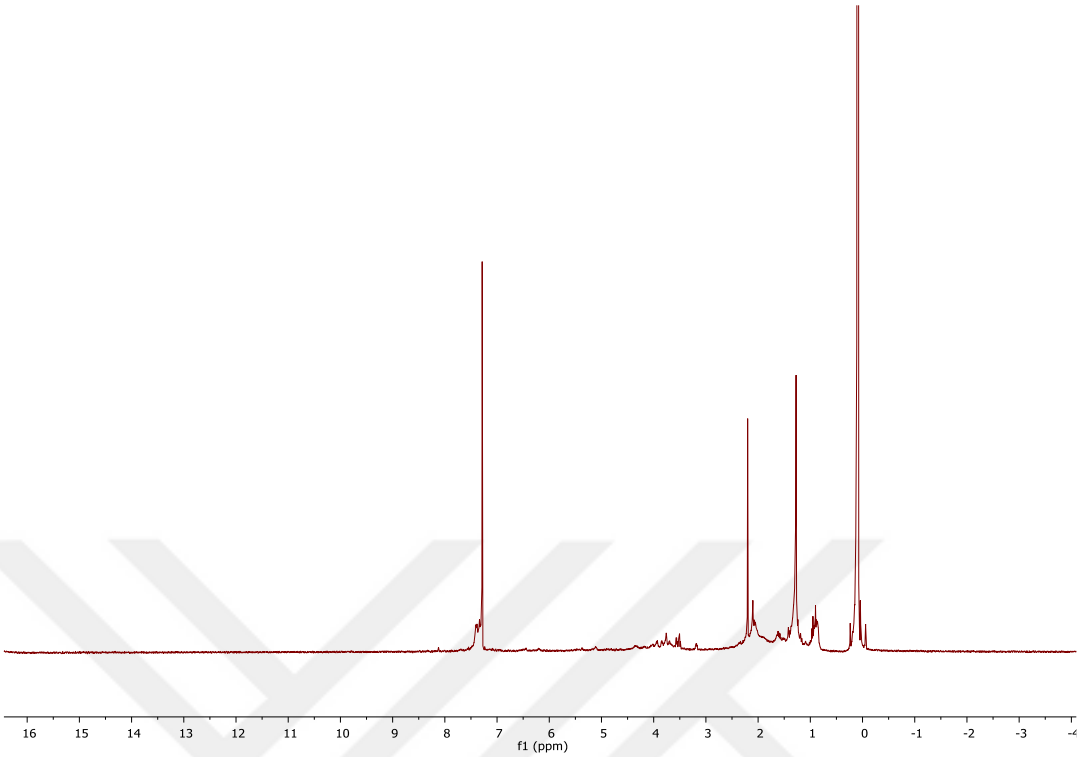


Appendix D. 9 The $^{1}$H-NMR spectrum of 3d compound.

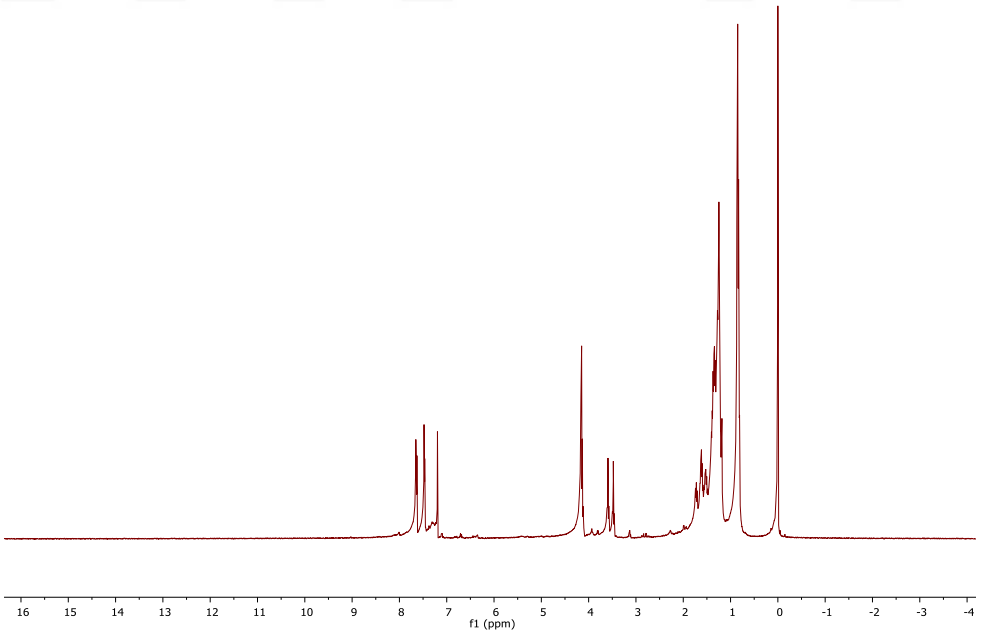


Appendix D. 10 The $^{1}$H-NMR spectrum of 3f compound.

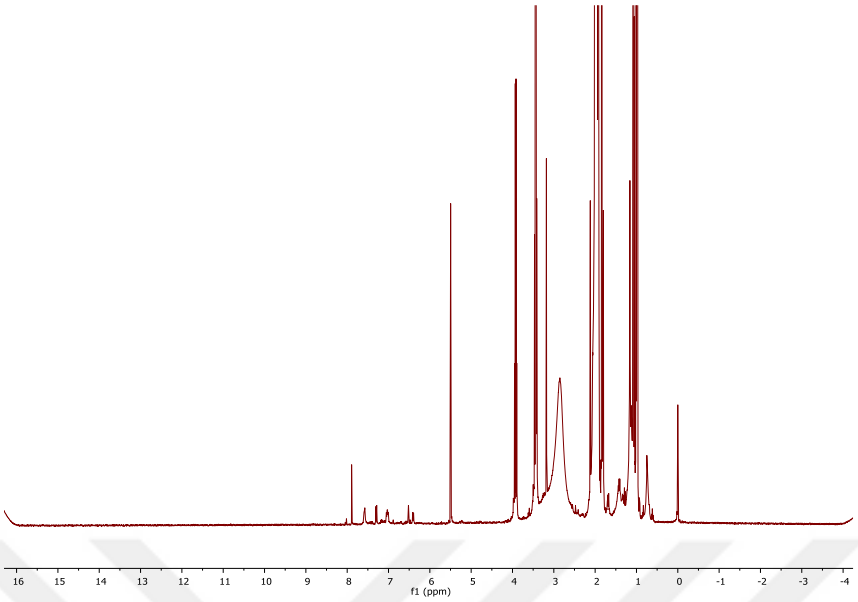


Appendix D. 11 The H-NMR spectrum of 3e- *Pd* complex.

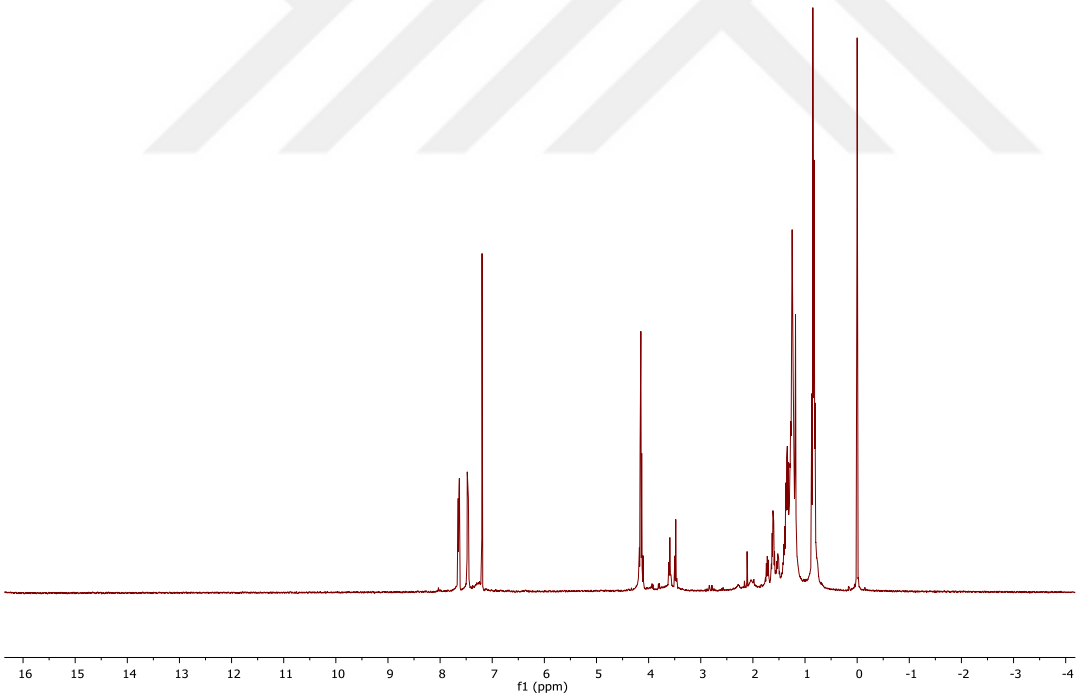


Appendix D. 12 The H-NMR spectrum of 3f- *Pd* complex.

## CURRICULUM VITAE

Surname, Name: Batır, Özge

### EDUCATION

| Degree | Institution | Year of Graduation |
|---|---|---|
| MS | METU Chemical Engineering | 2017 |
| BS | METU Chemical Engineering | 2015 |
| High School | Sıhhıye Atatürk Anadolu High School | 2010 |

### FOREIGN LANGUAGES

Advanced English, Basic German

### JOB EXPERIENCE

- Research and Teaching Assistant, Department of Chemical Engineering Middle East Technical University (11/2015 – Present)
- MKE Kayaş Detonator Factory, Engineer Intern (09/2013)
- Nuh Cement Factory, Engineer Intern (09/2014)

### PUBLICATIONS

#### Journal Articles

1- **Batir, O.**, Selçuk, N., & Kulah, G. (2019). Effect of kaolin addition on alkali capture capability during combustion of olive residue. Combustion Science and Technology, 191(1), 43-53.

2- Akdeniz, B., **Batir, O.**, & Bukusoglu, E. (2020). Identification and sorting of particle chirality using liquid crystallinity. Journal of colloid and interface science, 574, 11-19.

3- **Batir, O.**, Bat, E., & Bukusoglu, E. (2020). Strain-enhanced sensitivity of polymeric sensors templated from cholesteric liquid crystals. Soft Matter, 16(29), 6794-6802.

4- **Batir, O.**, Bat, E., & Bukusoglu, E. (2022) Interpenetrating network based polymeric sensors with enhanced specificity, sensitivity, and reusability. Sensors and Actuators B, 367, 132172.

**Oral Presentations**

1- **Batir, O.**, Selçuk, N., & Kulah, G. Effect of kaolin addition on alkali capture capability during combustion of olive residue. 10th Mediterranean Combustion Symposium, Naples, Italy, 17 – 21 September 2017.

2- **Batir, O.**, Bat, E., & Bukusoglu, E. Enhanced Sensitivity of Polymeric Sensors Templated from Cholesteric Liquid Crystals. ACS Fall 2021, Atlanta, US, 22-26 August. (online oral presentation)

3- **Batir, O.**, Bat, E., & Bukusoglu, E. Kolesterik Sıvı Kristal Şablonlu Polimerik Sensörlerin Hassasiyetinin Geliştirilmesi. UKMK 2021, Konya Technical University, Turkey, 10-12 June 2021. (online oral presentation)

**Poster Presentations**

1- **Batir, O.**, Bat, E., & Bukusoglu, E. Cholesteric Liquid Crystal Based Polymeric Sensors for Detection of Volatile Organic Compounds. 9th Eastern Mediterranean Chemical Engineering Conference, Ankara, Turkey, 31 August- 2 September 2018.

**PROJECTS**

- **Synthesis and Characterization of Chiral Reactive Metallomesogens (2020-2021)**
  *Scientific and Technological Research Council of Turkey (TUBITAK) Funded Project No: 120Z987*

- **Development of Polymeric Gas Sensors (2020)**
  *Middle East Technical University, Scientific Research Projects Coordination Unit (BAP) Funded Project No: TEZ-D-304-2020-10175*

- **Chemical Engineering Design Project: Design of Ethylene Oxide Plant (2014-2015)**
  *Middle East Technical University, Department of Chemical Engineering*

- **Topics in Chemical Engineering Course Project: Modeling of Hot Cyclone (2014-2015)**
  *Middle East Technical University, Department of Chemical Engineering*